Transport properties of electrolyte gated graphene devices

Von der Fakultät Mathematik und Physik
der Universität Stuttgart zur Erlangung der Würde eines
Doktors der Naturwissenschaften (Dr. rer. nat.)
genehmigte Abhandlung

vorgelegt von
Federico Paolucci
aus Italien

Hauptberichter:: Prof. Dr. Klaus von Klitzing
Mitberichter: Prof. Dr. J. Wrachtrup
Vorsitzender: Prof. Dr. A. Muramatsu
Tag der mündlichen Prüfung: 15. Mai 2015

Max-Planck-Institut für Festkörperforschung
Stuttgart, 2015

Contents

Introduction

Graphene is a single layer of carbon atoms arranged in a honeycomb lattice. It is the building block of graphite. The latter is made out of weakly coupled (van der Waals force) graphene layers stacked one on the other. Graphene was isolated in 2004 through micro-mechanical cleavage of graphite [1]. The interaction between lattice and charge carriers produces a linear electronic dispersion relation. Therefore, the charge carriers in graphene mimic chiral particles with zero mass. Many interesting physical properties were shown in graphene including room temperature integer quantum Hall effect, fractional quantum Hall effect, high temperature ballistic transport, and Hofstadter's butterfly [2, 3]. Superconductivity is predicted in graphene at extremely high carrier concentrations [4, 5], but it has never been experimentally proven. Electrolyte gating allows inducing high charge carrier concentration in a wide range of materials [6, 7]. These achievable densities are one order of magnitude lower than chemical doping, but two orders of magnitude higher than classic solid gating. Contrary to chemical doping, electric field induced charges do not affect the crystal structure of the studied material. In multilayer graphene also intercalation of ions in between the graphene planes is conceivable in electrolyte gated devices. It causes changes in the physical properties of graphene [8].

Chapter 1 The first chapter covers the fundamental properties of graphene. The focus lies on the lattice structure and the resulting electronic properties of graphene based materials. We start discussing the properties of graphite. Then, we introduce graphene stacks with a number of layers ranging from 2 to 10 layers. The next section is dedicated to monolayer graphene. Finally, we discuss the properties of intercalated graphitic compounds.

Chapter 2 This chapter is dedicated to electrolyte gating. We start with an historical account of filed effect transistors with particular focus on the so-called electric double layer transistor (EDL). We introduce the methods to determine the charge carrier concentration in the channel of such devices. Then, we address electrochemical doping by using electrolytes. Finally, we describe the different types of electrolyte and their most common applications.

Chapter 3 Here, we describe the fabrication process of electrolyte gated graphene devices. The micromechanical cleavage method and other procedures to obtain graphene mono-, bi- and multilayers are introduced. The evaluation of the thickness of graphene is discussed next. In the following sections, we discuss in detail the whole fabrication process including the transfer of graphene on a target substrate and the electrolyte production.

Chapter 4 This chapter is devoted to studies of the charge concentration in

electrolyte gated graphene. We introduce the measurement techniques. Then, we focus on the detailed description of the gate voltage dependence of the charge carrier concentration. We divide the behavior in three different regions: zero, low ($\leq$ 1.5 V) and high (>1.5 V) values of gate voltage. Finally we discuss the hysteresis in the charge concentration sweeping up and down the gate voltage.

Chapter 5 We present in this chapter the large magneto-resistance measured in our devices. This feature is interpreted as the consequence of strong charge disorder in the samples. Two different theoretical models help us to determine the strength of the charge inhomogeneity. Finally, we compare the values obtained with the different methods.

Chapter 6 Electrolyte gating can at high gate voltages also be used to intercalate multilayers of graphene. In this chapter we show evidence for intercalation in bilayer graphene. For high values of the gate voltage, the charge concentration shows a steep increase only in the case of multilayer graphene. We study the temperature and magnetic field dependence of the transport of a bilayer graphene sample at high gate voltage. It shows weak localization up to high temperature. This feature is attributed to intercalation of the graphitic host.

Chapter 1

Carbon in flatland

Carbon is a chemical element of group 14 in the periodic table of elements and has atomic number 6. Carbon has three natural isotopes: C^{12} and C^{13}, that are stable, while C^{14} is radioactive. The electronic configuration of isolated carbon is $1s^2 2s^2 2p^2$: the $1s^2$ electrons belong to the ion core of the atom, while the 2s, $2p_x$, $2p_y$ and $2p_z$ orbitals hold the four valence electrons.

Carbon has two main allotropes: diamond and graphite. Their crystal structures are represented in Figure 1.1. The two crystals are generated by different chemical bondings between the carbon atoms. In diamond, the bondings are tetrahedral and involve a sp^3 hybridization of the carbon atoms. As a consequence, diamond has the three-dimensional cubic face centered crystal (FCC) structure shown in Figure 1.1-a. All the valence electrons are involved in the covalent bond, therefore diamond is a transparent electrical and heat insulator. In graphite, the bondings are trigonal and involve sp^2 hybridization of carbon. As a result, graphite consists of two dimensional carbon layers arranged in a honeycomb lattice, with covalent bondings within the layer. The building block of graphite, i.e. a single layer of carbon atoms arranged in hexagonal lattice, is called graphene. The delocalized π-orbitals produce weak van der Waals interactions that link the different layers. As a result, graphite is an anisotropic material: it is a good thermal and electrical conductor in the plane and a poor one in the direction perpendicular to the layers.

In this chapter, we discuss some fundamental properties of different compounds based on carbon arranged in two-dimensional layers. We start with a description of graphite: a 3D stack of graphene layers (1.1). Subsequently, we consider thinned down graphite and analyze the electronic properties of multilayer graphene (1.2). In section 1.3 we discuss the properties of the thinnest stack of 2D carbon layers: bilayer graphene. We continue describing the properties of single layer graphene (1.4) paying particular attention to its crystal structure and its electronic properties. Finally, we discuss the structure and physical properties of graphitic intercalated compounds (1.5). These are materials where graphite hosts other chemical species (single atoms or molecules) between the carbon planes.

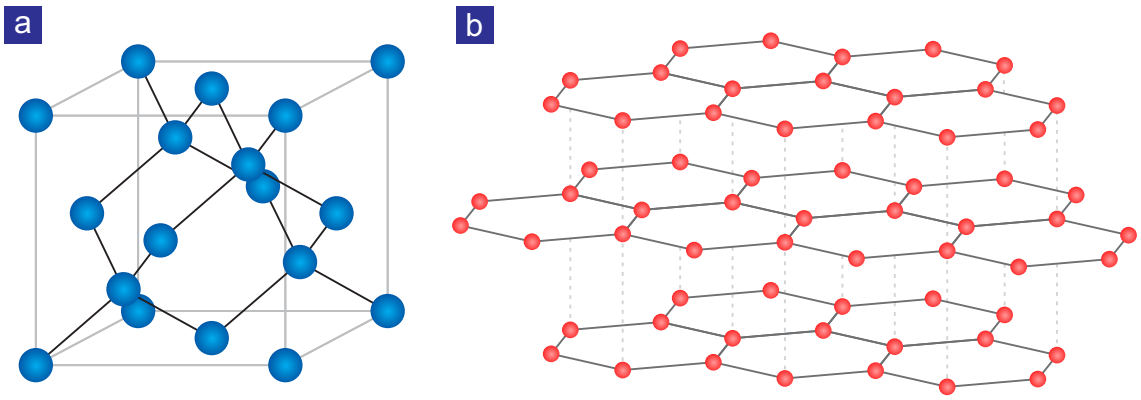

Figure 1.1: Crystal structure of diamond and graphite. (a) Diamond lattice: blue dots represent the carbon atoms and the black lines depict the covalent bonds. (b) Graphite lattice: red dots represent the carbon atoms, solid gray lines indicate the covalent bonds in the plane, while the dashed lines depict the van der Waals interaction between the planes.

1.1 Graphite

Graphite has a layered structure. The carbon atoms are arranged in a honeycomb lattice within each layer. All the carbon atoms in one layer are equivalent, but from a crystallographic point of view, it is possible to define two inequivalent sublattices called A and B. In every sublattice, the atoms have a different orientation of the bonds and are translationally invariant. The distance between adjacent carbon atoms is $d = 1.42$ Å, while the distance between adjacent atoms belonging to the same sublattice (A or B) is $a = d \cdot \sqrt{3} = 2.46$ Å [9]. a is called the lattice parameter.

The graphene layers can stack in different configurations, but the most common arrangement is the so-called Bernal stacking (or AB stacking). The crystal structure of AB stacked graphite is represented in Figure 1.2.

In AB stacked graphite the two layers are separated by a distance $c = 3.35$ Å and a carbon atom of the upper layer is either located on top of a carbon atom from the layer below or above the center of the hexagon described by the carbon atoms of the layer below (see Figure 1.2). In other words, an atom of sublattice A of the lower layer can be vertically aligned only with a carbon atom of the sublattice B of the upper layer. As a consequence, this stacking yields a 6-fold degeneracy of the crystal structure.

The translation (unit cell) vectors of the graphite crystal structure $\mathbf{a_1}$, $\mathbf{a_2}$ and $\mathbf{a_3}$ are shown in Figure 1.2 and are given by:

$$\begin{aligned} \mathbf{a_1} &= a\big(\sqrt{3}/2, -1/2, 0\big) \\ \mathbf{a_2} &= a\big(\sqrt{3}/2, 1/2, 0\big) \\ \mathbf{a_3} &= 2c\big(0, 0, 1\big). \end{aligned} \tag{1.1}$$

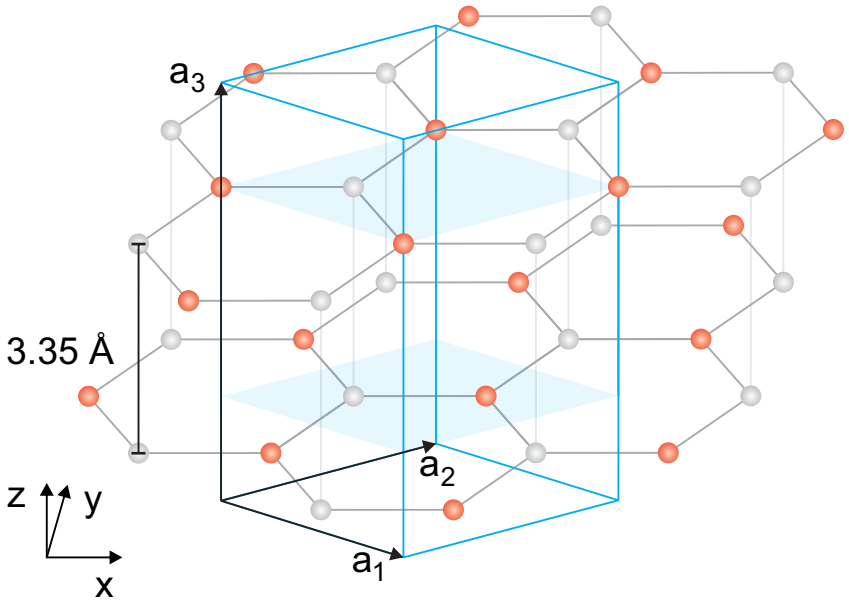

Figure 1.2: Crystal structure and unit cell of Bernal stacked graphite. The gray dots in the upper layer represent sublattice A, while in the lower layer they depict sublattice B. The red dots highlight sublattice A in the lower layer, while they represent sublattice B in the upper one. The turquoise prism represents the unit cell and the turquoise solid parallelograms are sections of the unit cell passing through the graphite layers.

The translation vectors define the unit cell of graphite (shown in Figure 1.2), where the in-plane and out of plane lattice parameters are respectively $a = |\mathbf{a_1}| = |\mathbf{a_2}| = 2.46$ Å and $c_L = 2c = 6.71$ Å.

The basis vectors of the reciprocal lattice for graphite are:

$$\begin{aligned} \mathbf{b_1} &= \frac{2\pi}{a}\left(1/\sqrt{3}, -1, 0\right) \\ \mathbf{b_2} &= \frac{2\pi}{a}\left(1/\sqrt{3}, 1, 0\right) \\ \mathbf{b_3} &= \frac{4\pi}{c}\left(0, 0, 1\right). \end{aligned} \tag{1.2}$$

The reciprocal lattice is a prism with a hexagonal base. The first Brillouin zone (BZ) is the solid defined by the perpendicular bisectors of the sides connecting adjacent reciprocal lattice points [10]. The first BZ is shown in Figure 1.3-a: as a result of the real and reciprocal lattice symmetry, the first Brillouin zone is an hexagonal prism of height $|\mathbf{b_3}| = 4\pi/c$.

The band structure of graphite is calculated within a tight-binding theory [11,12]. This approach takes in account the in-plane and out-of-plane interactions between the electronic orbitals of the carbon atoms in sublattices A and B. The complete

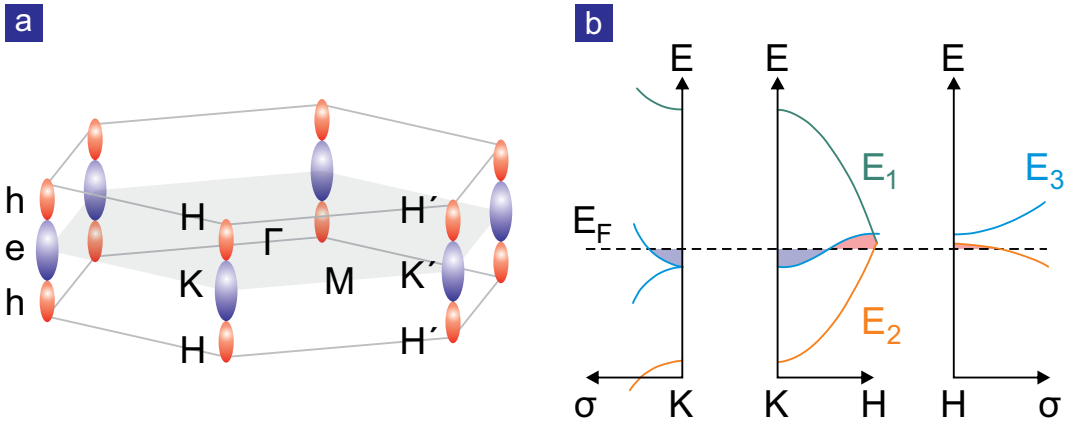

Figure 1.3: First Brillouin zone and Band structure of Bernal stacked graphite. (a) First Brillouin zone. The important symmetry points are marked. The blue ellipsoids depict the electron Fermi surfaces and the red ellipsoids the hole Fermi surfaces. Modified from [9]. (b) 3D energy bands of graphite: blue areas are the electron pockets near the Fermi level and the red areas are the hole pockets. Modified from [9].

electronic energy spectrum of graphite consists of 16 bands: 12 σ-bands and 4 π-bands. The π-bands (2 bonding and two antibonding) are strongly coupled and lie between two groups of σ-bands (separated by $\sim$ 5 eV). Only 8 energy bands are filled, because graphite has 16 electrons in the unit cell (4 valence electrons for each carbon atom in the cell). The 6 low lying σ-bands are completely full and the Fermi level crosses the middle of the 4 π-bands. Therefore, only π-bands influence the electronic properties of graphite.

Figure 1.3-b shows the energy band spectrum of graphite near the Fermi level (E_F). E_1, E_2 and the doubly degenerate E_3 bands are the four π-bands that overlap for about 41 meV. The E_3 band is doubly degenerate near the zone edges. The overlap is due to the interaction between the carbon atoms of sublattice B of next-nearest-neighbor planes. E_1 is completely above the Fermi level (see Figure 1.3-b) and is therefore completely empty. E_2 is almost full leaving a hole pocket (schematically shown as red ellipsoids in Figure 1.3-a and the red area in the direction $H-\sigma$ in Figure 1.3-b) near the zone corner H (and H'). The majority electron (two regions) and hole (one region) pockets are created by the doubly degenerate band E_3. The overlap between the valence and conduction bands makes graphite into a semimetal.

The Fermi level crosses the energy band E_3. The three carrier pockets, two hole-like and one electron-like, form along the HKH (and $H'K'H'$) axis (see Figure 1.3-b). The Fermi level is chosen to ensure that electron and hole pockets have the same volume. Since the degeneracy of E_3 is lifted away from the BZ edges, the Fermi surfaces (thus the free charges) are located in the areas around the direction HKH ($H'K'H'$) as shown in Figure 1.3-a. For rising (decreasing) E_F, i.e. free carrier concentration, the Fermi surfaces expand to the center of the Brillouin zone Γ allowing only electrons (holes) as free charges.

1.2 Multilayer graphene

Graphite is a 3D material build up of a stack of two-dimensional carbon graphene layers. The question that immediately arises is the following: how may graphene layers are needed in order to be able to speak of graphite? To answer this question it is necessary to calculate the band structure of a thin stack of graphene layers within a tight-binding description and compare the results with the electronic energy levels of graphite [13]. The main parameter to compare is the band overlap between the 4 π-bands at the K (K') points of the first BZ, because it determines the transport properties of the graphene stack. A decrease of the number of layers implies a lower overlap of the 4 π-bands near the K (K') points, because the interaction between atoms of the A and B sublattices in different layers (γ_1) is gradually suppressed. For 11 layers the difference in the band overlap compared with bulk graphite is less than 10% [13]. A further decrease of the number of graphene sheets causes an increase of this difference. Therefore, for graphene stacks thinner than 11 layers one should not speak of graphite anymore [14].

We define "multilayer graphene" as a stack of a number of carbon layers ranging between 2 and 10. The crystal structure is identical to that of graphite (see Figure 1.2). In multilayer graphene the symmetry of the crystal changes with the number of layers. For an even number of layers the crystal has a 3-fold symmetry, while for an odd number of layers the symmetry is 6-fold (as in the graphite) [15].

The energy spectrum of multilayer graphene can be calculated starting from the AB-stacked graphite model [16]. The coupling energy between carbon sites within one plane, γ_0, and the difference between the on-site energy of equivalent sites, Δ', are taken from experimental data of bulk graphite. The number of layers (N) affects the doubly degenerate E_3 band. E_3 consists of N energy levels if N is even, and $N+1$ if N is odd [13]. The other two π-bands E_1 and E_2 are nearly unaffected by the number of layers. This implies that the number of graphene layers influences mainly the band structure near the Fermi level around the symmetry points K (K') of the first Brillouin zone.

Figure 1.4 shows the band structure of multilayer graphene near the K (K') for low energies (energy close to E_F) when varying the thickness from 3 to 6 layers. A striking property is a dramatic change of the shape of the bands in k-space away from their minima (maxima. For an odd number of layers, there are two linear bands (one π bonding and one π antibonding), because there is no interlayer-coupling between the first and the last layers of sublattice A and B [13]. For an even number of layers these bands exhibit a parabolic dispersion instead. The other bands follow a parabolic dispersion for all the different thicknesses. The coupling between the different bands is strong near the K (K') points. Therefore, deviations from the parabolic shape are expected at low energies near the minima and maxima (see Figure 1.4). The overlap between the highest valence and lowest conduction band decreases for thin multilayers. For example, trilayer graphene has an overlap of only 13.8 meV [13]. All systems with $N \geq 3$ show an overlap between conduction and valence bands, therefore they are defined as semimetals.

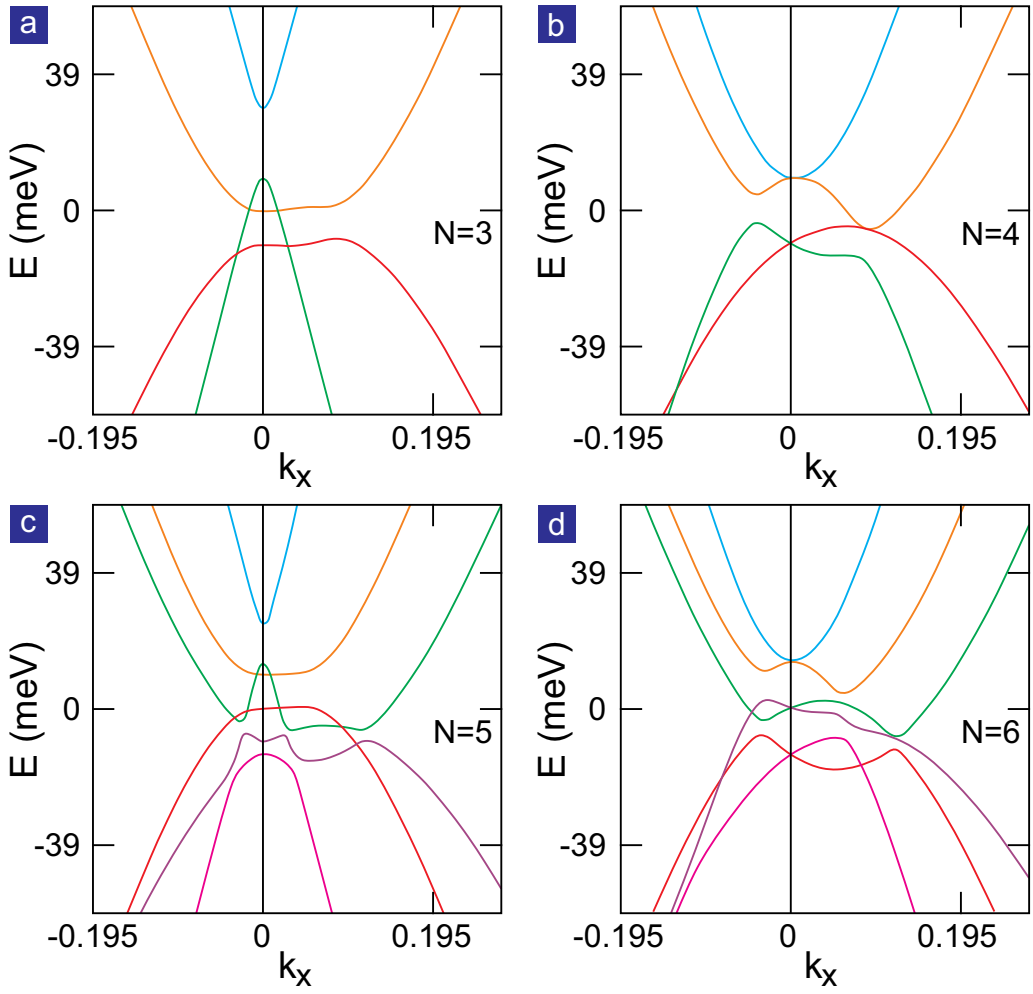

Figure 1.4: Band structure of different multilayer samples. Band structure of 3- (a), 4- (b), 5- (c) and 6- (d) layers of graphene near the K (K') points. The π-bands are highlighted with different colors. The zero point in k-space is equivalent to point K (K') in the first BZ. All the curves are adapted from [16].

1.3 Bilayer graphene

Bilayer graphene is the thinnest stack of 2D layers of carbon atoms. It consists of two coupled graphene monolayers. The crystal structure and unit cell (containing 4 atoms) of bilayer graphene are the same as of AB stacked graphite (see Figure 1.2). We call the two atoms of the lower layer A_1 and B_1 (A and B refer to the sublattice), and we label the atoms of the upper layer as A_2 and B_2. Atoms B_1 are below atoms A_2, while A_1 and B_2 are not aligned with any atom in the other layer. A_2 and B_1 are assumed to be dimer sites, because their orbitals are strongly coupled. A_1 and B_2 are non-dimer sites, because they are fully uncoupled with any other orbital of the other layer [17]. Bilayer gaphene is a multilayer with an even number of layers. Hence, bilayer graphene has a 3-fold symmetry and its point group is D_{3d} [15].

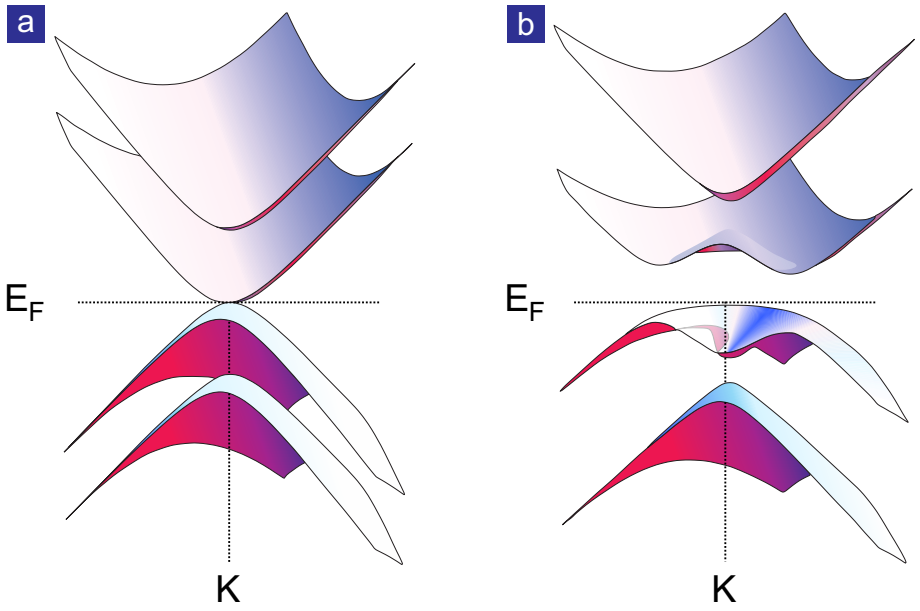

Figure 1.5: Band structure of bilayer graphene. (a) Band structure of bilayer graphene around the symmetry point K (K'). (b) Band structure of bilayer graphene with an electric-field applied perpendicular to the layers: an energy gap opens between the two low energy bands. The symmetry point K (K') and the Fermi energy are marked. Adapted from [18].

The reciprocal lattice vectors $\mathbf{b_1}$, $\mathbf{b_2}$ and $\mathbf{b_3}$ are the same as of graphite (see Equation 1.5). Therefore the reciprocal lattice and the first Brillouin zone are prisms with a hexagonal base (see Figure 1.3-a). The symmetry of the reciprocal lattice supports a Brillouin zone with two degeneracy points at the two inequivalent corners K and K' of the first BZ [19].

The band structure of bilayer graphene can be calculated within the same tight-binding description as of graphite. The important parameters for bilayer graphene are: the nearest-neighbour hopping within a layer γ_0, the coupling between the pairs of orbitals on the dimer sites γ_1, the interlayer coupling between the pairs of orbitals on non-dimer sites γ_3, the coupling between the orbitals of dimer and non-dimer sites γ_4, the asymmetry between the two layers U (that can cause the opening of a mini-gap), the energy difference between dimer and non-dimer states Δ' and the difference between the energy states of sublattices A and B on the same layer δ_{AB} [17, 19].

U and δ_{AB} are related to extrinsic factors and are not included in the band structure calculation of the bare bilayer ($U = \delta_{AB} = 0$). The other 5 parameters are usually taken from infrared spectroscopy experiments. The resulting band structure of bilayer graphene is shown in Figure 1.5-a. There are 4 parabolic bands centered at the edges of the first BZ (K and K'): two bands touching at zero energy arising from hopping between the non-dimer orbitals and another two that start at $\pm\gamma_1$ and originate from the coupling between the dimer sites. The coupling between the

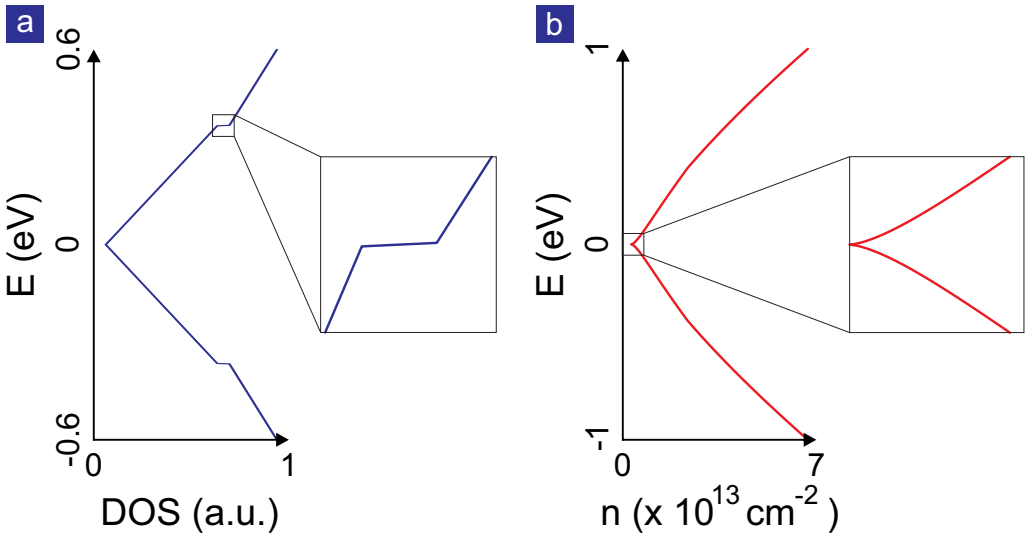

Figure 1.6: Density of states and carrier density of bilayer graphene. (a) DOS of bilayer graphene. The square shows a magnification around the bottom of the second electron band. (b) Dependence of carrier density on energy. The square shows the magnification near zero energy.

orbitals of the dimer sites (A_2 and B_1) is about $\gamma_1 = 0.39$ eV [20].

A precise calculation of the energy band close to the Fermi level is possible by neglecting the influence of the environment (U and δ_{AB}) and the small interaction between dimer and non-dimer orbitals γ_4. With these approximations, the two low energy bands show a small overlap of 1.6 meV [13]. This overlap implies semimetallic behavior for bilayer graphene.

Figure 1.5-b shows the band structure of biased bilayer graphene in the vicinity of the first BZ edges (K or K'). In the presence of an electric field between the two layers the asymmetry parameter U no longer vanishes [18, 21]. A small unbalance between the electron and hole charge distribution in the two layers is more realistic. The gap is preserved, but within this model the strength and the shape of the gap both depend on the carrier density in each layer and on the charge unbalance between the layers [21].

The density of states (DOS) is derived from the tight-binding Hamiltonian. In the case of balanced bilayer graphene, there exists an analytical expression for the DOS per unit cell for positive energy values [22] and it has the form:

$$DOS(E) = \frac{g_v g_s}{2\pi\gamma^2}\left[\frac{\gamma_1}{2} + E + \theta(E-\gamma_1)\left(E - \frac{\gamma_1}{2}\right)\right], \tag{1.3}$$

where $g_s = 2$ is the spin degeneracy, $g_v = 2$ is the valley degeneracy, $\gamma = (\sqrt{3}/2)a\gamma_0$ is the band parameter related to the lattice constant and the nearest-neighbour hopping, and $\theta(r)$ is the step function (with value 1 when $r > 0$, 0 otherwise) which defines the appearance of the second band in the DOS. The density of states is symmetric around $E = 0$ as shown in Figure 1.6-a. Different from semiconductor

based two dimensional electronic systems whuch usually posses a simple parabolic dispersion and therefore constant DOS, bilayer graphene shows a DOS strongly dependent on energy. $E = \pm\gamma_1 = \pm 0.39$ eV coincides with the minimum (maximum) of the second electron (hole) band. This second band shows up as a step in the DOS at 0.39 eV (see Figure 1.6-a).

The integration of the DOS over energy gives the dependence of the charge carrier density n on E (shown in Figure 1.6-b). The increase of the density is symmetric around zero energy, i.e. electron and hole sides are equivalent. The second band starting at an energy of 0.39 eV gets filled for charge carrier densities exceeding $\sim 2.2 \times 10^{13}$ cm^{-2}.

1.4 Monolayer graphene

Monolayer graphene is the building block of every graphitic material. The hybridization of the carbon atoms and the crystal structure of the single layer are the same as of graphite. Graphene is perfectly two dimensional, therefore its unit cell and Brillouin zone are defined within the plane.

The crystal structure of graphene is shown in Figure 1.7-a. The sublattices A and B are indicated with green and red dots. The unit cell (turquoise parallelogram) contains two carbon atoms and is defined by the following lattice vectors:

$$\begin{aligned} \mathbf{a_1} &= a\big(\sqrt{3}/2, 1/2\big) \\ \mathbf{a_2} &= a\big(\sqrt{3}/2, -1/2\big) \end{aligned} \tag{1.4}$$

where $a = 2.46$ Å is the same in-plane lattice constant as of graphite (i.e. the distance between adjacent atoms belonging to the same sublattice) [2].

The reciprocal lattice vectors are obtained from the equation $\mathbf{a_i} \cdot \mathbf{b_j} = 2\pi\delta_{ij}$ (where $i, j = 1, 2$ [10]) and have the following form:

$$\begin{aligned} \mathbf{b_1} &= \frac{2\pi}{a}\big(1/\sqrt{3}, 1\big) \\ \mathbf{b_2} &= \frac{2\pi}{a}\big(1/\sqrt{3}, -1\big). \end{aligned} \tag{1.5}$$

The reciprocal lattice (see Figure 1.7-b) has the same symmetry properties as the real space lattice, so the reciprocal space belongs to the hexagonal point group. The first BZ is the smallest polyhedron centered at the origin of the reciprocal lattice and enclosed by the perpendicular bisectors of the reciprocal lattice vectors [10]. For graphene, the symmetry of the first BZ is the same as that of the lattice (hexagonal). The important symmetry points of the first Brillouin zone are: the centre Γ, the inequivalent zone corners K and K', and the edge mid point M.

The band structure of graphene is calculated within the tight-binding approximation used for graphite [11, 12]. In monolayer graphene the interlayer interactions are obviously absent, thus γ_1, γ_3, γ_4, U and Δ' are not present in the model. The sublattices A and B are assumed to be isoenergetic, so $\delta_{AB} = 0$. The nearest-neighbour

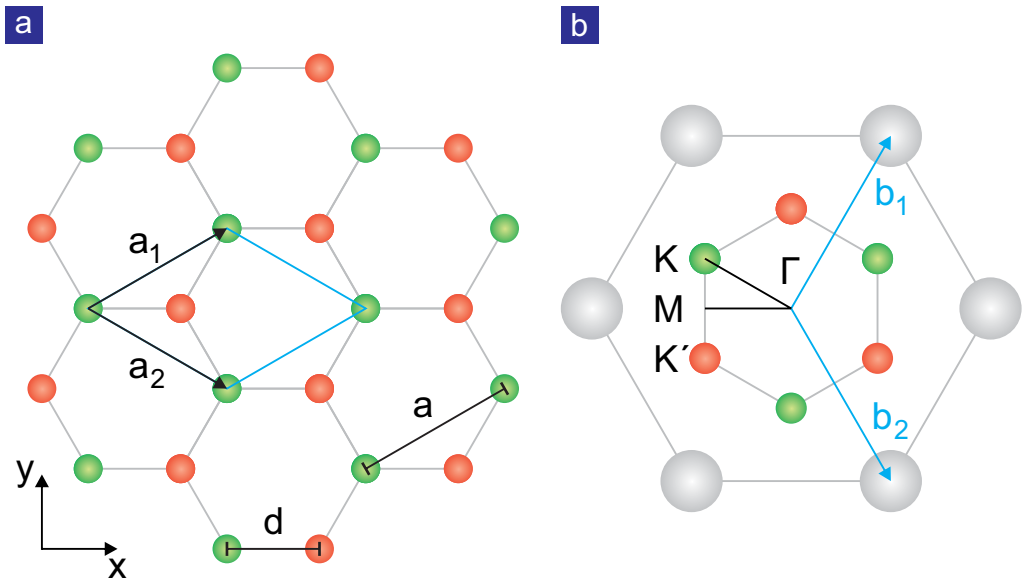

Figure 1.7: Crystal structure and first Brillouin zone of monolayer graphene. (a) The green and red dots represent the two sublattices of the graphene structure. Lattice constant a and the distance between adjacent atoms d are shown. The unit cell vectors $\mathbf{a_1}$ and $\mathbf{a_2}$ are included as black arrows and the unit cell is depicted with the turquoise parallelogram. (b) The reciprocal lattice, defined by the basis vectors $\mathbf{b_1}$ and $\mathbf{b_2}$, is displayed in gray. The first BZ corresponds to the internal hexagon. The inequivalent points K and K' are colored as green and red dots, respectively.

hopping γ_0 is the only parameter used in the tight-binding energy dispersion calculations for graphene [11].

The π bands of monolayer graphene are described by the following equation:

$$E(\mathbf{k}) = \pm\gamma_0 \left[1 + 4 \cdot \cos\left(\frac{\sqrt{3}k_x a}{2}\right) \cdot \cos\left(\frac{k_y a}{2}\right) + 4 \cdot \cos^2\left(\frac{k_y a}{2}\right) \right]^{1/2} \tag{1.6}$$

where the plus sign describes the antibonding π^*-band ($E > 0$), the minus sign applies to the bonding π-band ($E < 0$), $\gamma_0 \simeq 3$ eV and $a = 2.46$ Å is the lattice parameter.

The band structure of graphene is shown in Figure 1.8. The π-(bonding) and π^*-(antibonding) bands are symmetric and the two free electrons of the two carbon atoms in a unit cell completely fill the π bands. Thus, the Fermi level lies at the K and K' points where the two bands touch. The K and K' points are located at the edges of the first Brillouin zone and their exact position in k-space is:

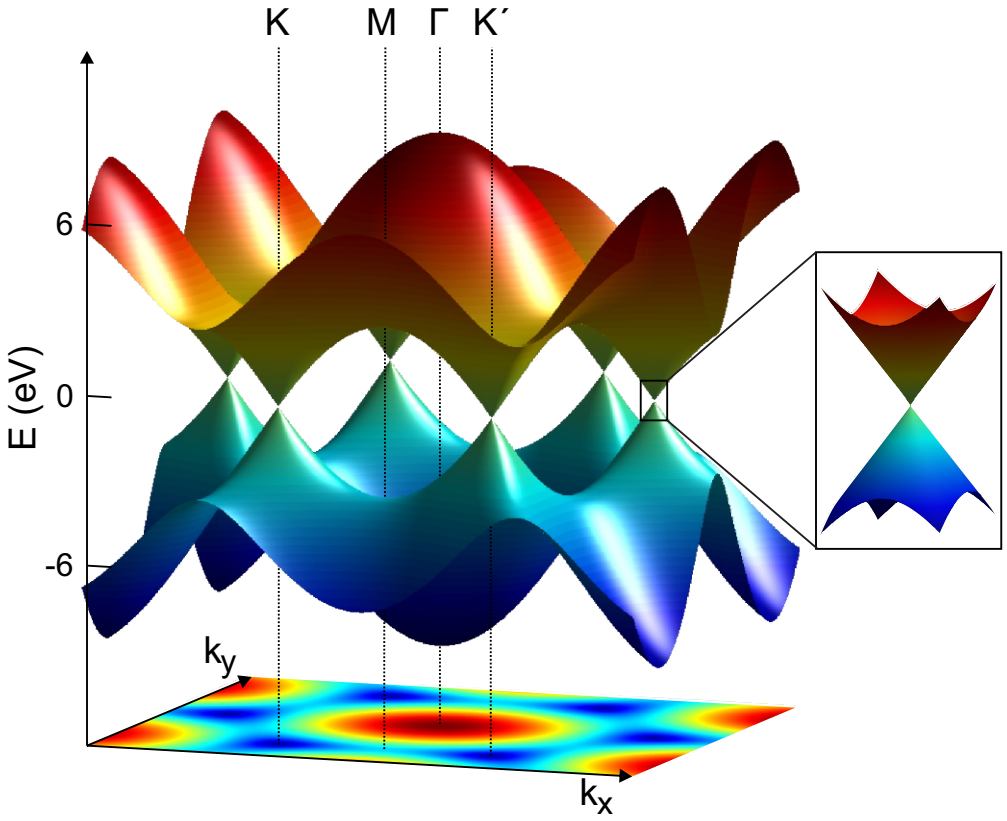

Figure 1.8: Band structure of monolayer graphene. 3D visualization of the band structure of graphene. Important symmetry points are labeled. A magnification of the bands near the K (K') point is shown in the square box. The base plane is a 2D color map of the energy dispersion of the bands in k-space.

$$\begin{aligned} \mathbf{K} &= \left(-\frac{2\pi}{3\sqrt{3}a}, -\frac{2\pi}{3a} \right) \\ \mathbf{K}' &= \left(\frac{2\pi}{3\sqrt{3}a}, -\frac{2\pi}{3a} \right). \end{aligned} \tag{1.7}$$

The energy dispersion near the two edge points K and K' is linear and has the following expression [11]:

$$\Big|E(\mathbf{k})\Big| \simeq \sqrt{3}\pi\gamma_0 a \Big|\mathbf{k} - \mathbf{K}\Big| = \hbar v_F \Big|\mathbf{k} - \mathbf{K}\Big| \tag{1.8}$$

where $\hbar$ is the reduced Planck constant and $v_F = \sqrt{3}\gamma_0 a/2\hbar \simeq 10^6 m/s$ is the Fermi velocity. The Fermi velocity is independent of energy and momentum. This is valid only in the vicinity of K (K'), i.e. $\mathbf{k} \ll \mathbf{K}$ [12].

The effective mass of free electrons in a solid ($m*$) is inversely proportional to the second derivative of the energy with the wave-vector, i.e. $m*$ is inversely

proportional to the curvature of the bands in k-space [10]. Since graphene has a linear energy dispersion near K and K' points, the effective mass of monolayer would diverge near zero energy. For this reason the motion of electrons in graphene at low energy can not be described within the Schrödinger formalism.

The linear energy dispersion requires the use of a Dirac-like formalism for massless particles. For this reason, K and K' points are called Dirac points and the charge carriers in the vicinity of these points are called Dirac fermions. The Dirac formalism leads to a square root dependence of the cyclotron mass on the carrier density [23]. This feature distinguishes graphene from other two dimensional systems described by parabolic bands, for which the cyclotron mass is density independent.

Since graphene has a linear and symmetric gapless band structure near K and K', the electron and hole states are interconnected and show a charge-conjugation-like symmetry. This symmetry is a consequence of the presence of two inequivalent sublattices (A and B) that are responsible for the different branches of the electronic dispersion. A new quantum number, called pseudospin, is introduced to characterize the relative contribution of each sublattice. It is important to emphasize that the pseudospin is completely independent from the real spin of the quasiparticles in the graphene bands.

The density of states of graphene can be derived from the tight-binding Hamiltonian [11]. Within the assumption of energetically equivalent sublattices A and B, i.e. $\delta_{AB} = 0$, the only important parameter enter the calculation is the nearest-neighbour hopping γ_0. The DOS of graphene can be derived analytically and has a form equivalent to the distribution function calculated for a hexagonal net [24]. The density of states for unit cell can be expressed as [2]:

$$
\begin{aligned}
DOS(E) &= \frac{4|E|}{\pi^2\gamma_0^2\sqrt{Z_0}}\mathbf{F}\left(\frac{\pi}{2},\sqrt{\frac{Z_1}{Z_0}}\right) \\
Z_0 &= \begin{cases} \left(1+\left|\frac{E}{\gamma_0}\right|\right)^2 - \frac{[(E/\gamma_0)^2-1]^2}{4} & -\gamma_0 \le E \le \gamma_0 \\ 4\left|\frac{E}{\gamma_0}\right| & -3\gamma_0 \le E \le -\gamma_0 \vee \gamma_0 \le E \le 3\gamma_0 \end{cases} \\
Z_1 &= \begin{cases} \left(1+\left|\frac{E}{\gamma 0}\right|\right)^2 - \frac{[(E/\gamma_0)^2-1]^2}{4} & -3\gamma_0 \le E \le -\gamma_0 \vee \gamma_0 \le E \le 3\gamma_0 \\ 4\left|\frac{E}{\gamma_0}\right| & -\gamma_0 \le E \le \gamma_0 \end{cases}
\end{aligned}
\tag{1.9}
$$

where $\mathbf{F}\left(\pi/2,\sqrt{Z1/Z_0}\right) = \int_{\pi/2}^{0} d\theta/[1-(Z_1/Z)\sin^2\theta]$ is the complete elliptic integral of the first type [24].

Two dimensional electronic systems (2DES) with a parabolic dispersion posses energy independent DOS. Frequently, the DOS is higher for holes than electrons, because the holes tend to have higher effective mass than electrons. In graphene, the DOS is strongly energy dependent (see Figure 1.9-a). For low energies ($\mathbf{k} \ll \mathbf{K}$), the density of states is linear with energy. DOS further increases with E until it reaches a maximum when $E = \gamma_0$. In this region, there is a steep increase of the charge carrier density n resulting in a slope change or a kink in the dependence of

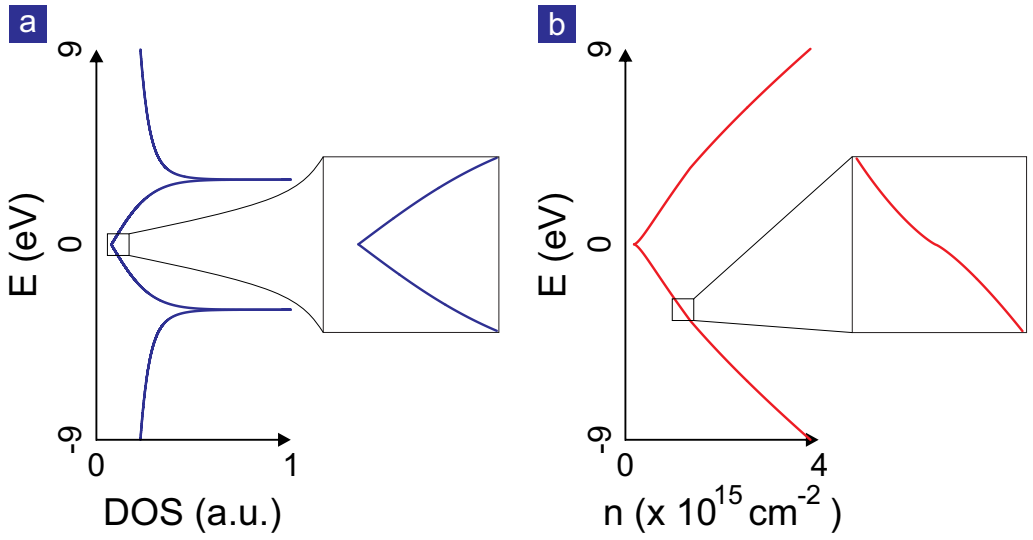

Figure 1.9: Density of states and carrier density of monolayer graphene. (a) DOS of monolayer graphene. The insert shows a magnification at zero energy. (b) Dependence of the carrier density on the Fermi energy. The insert shows the magnification at the singularity at the M point.

n on energy (see Figure 1.9-b). In graphene the density of states is symmetric with respect to zero energy, therefore electrons and holes have identical effective mass.

The singular point in the DOS corresponds to a van Hove singularity in the band structure of graphene (see Figure 1.8). It is located at the $\mathbf{M} = (0, -2\pi/3a)$ symmetry point in momentum space. M is the mid point of the straight line connecting K and K' (see Figure 1.7-b), thus the van Hove singularity is generated at the connection between two Dirac cones (one in K and one in K').

Van Hove singularities are usually associated with anomalies in the low temperature behavior of electronic systems [25]. The van Hove singularity at the M point attracts a lot of interest from theorists [4, 5, 26] and experimentalists, because it is situated at a charge carrier density $n \simeq 9.5 \times 10^{14}$ cm^{-2}. This may be experimentally achievable by chemical doping. Theoretically, filling of the bands to the van Hove singularity could bring about electron-electron coupling mediated superconductivity in monolayer graphene [4]. Other theoretical works predict magnetic and superconducting instabilities for Ca decorated monolayers when the Fermi level is higher than 2 eV [26]. Within this model superconductivity is created by electron-phonon coupling and appears at higher temperatures than the magnetic instability. More recent works on decorated graphene showed that Li decoration could cause electron-phonon mediated superconductivity in graphene with higher critical temperature than Ca decoration [5].

1.5 Graphitic intercalation compounds

Graphitic intercalation compounds (GICs) are formed by the insertion of chemical species (atoms or molecules) between the carbon layers in a graphene stack [8]. The chemical species in between the graphene layers are called the intercalants (see Figure 1.10-a).

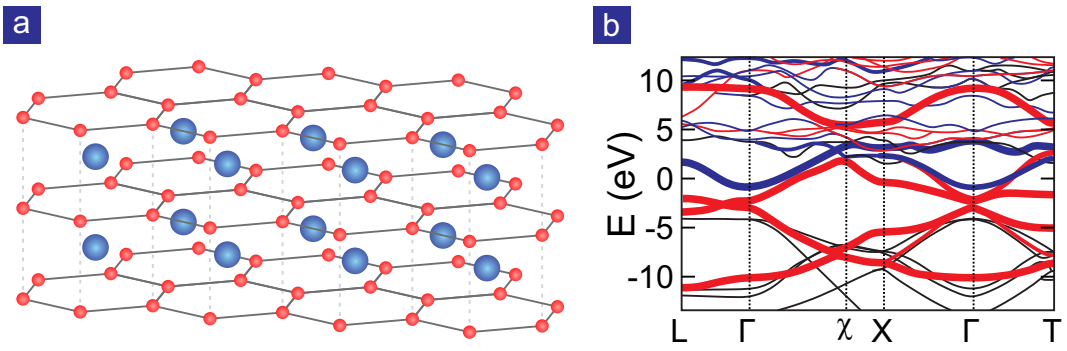

Figure 1.10: Crystal structure and band structure of graphitic intercalated compounds (a) Crystal structure of a GIC. The red dots represent the carbon atoms while the blue circles depict the intercalant between the layers. (b) Electronic band structure of CaC_6. The intercalant bands are shown in blue, the carbon π-bands in red and the carbon σ-bands in black. Adapted from [27].

The stoichiometry of GICs depends on the dimensions of the intercalant atoms: big atoms (M= Cs , K and Rb) create a MC_8 composition, while smaller ones (M= Ba, Ca, Eu, Yb and Sr) allow a MC_6 stoichiometry [28]. Lithium is a very small atom, thus the Li intercalated graphitic compounds can have different stoichiometry (LiC_6, LiC_3 and LiC_2) depending on the preparation technique. The first effect of intercalation is the increase of the distance between the graphene layers, which depends on the size of the intercalant species [29].

The carbon layers in graphite are usually arranged in AB stacking, but after the intercalation process they rearrange in AA stacking [28]. The configuration of minimum energy is when the intercalant is in the centre of the carbon hexagon of the graphene structure. This is only possible if the graphene layers are stacked with atoms of different layers perfectly aligned.

Another important structural phenomenon in GICs is the so-called staging. When chemical species are inserted between the graphite layers, periodic arrangements of graphene and intercalant layers can be formed. The period is given by an intercalant layer and the number of graphene layers n sandwiched between two intercalant layers [30, 31]. n is called stage of the GIC. The creation of staging is attributed to Coulomb repulsion between the intercalant layers [32] and can be experimentally visualized in x-ray diffraction and Raman spectroscopy [8, 31].

The electronic energy dispersion in GICs can be determined starting from the properties of graphite and the intercalant [8]. The band structure has been calculated only for stage 1 compounds, because the problem becomes extraordinarily

complex for higher stage compounds. Differently from graphite, the electronic energy dispersion of GICs is not calculated in a tight-binding approximation, but rather using first-principle calculations taking into account the positions of each of the atoms and the interactions between their orbitals. Figure 1.10-b shows the electronic band structure of CaC_6. The π- and σ-bands of CaC_6 display strong similarities with the graphite ones (see Figure 1.3-b), but they are more filled due to the charge transfer from the intercalant. The main difference is the presence of a new set of bands at the Fermi level due to the intercalant species. These bands are usually called intercalant or interlayer bands [27]. The analysis of the band structure for CaC_6 can be generalized for other graphitic intercalation compounds.

GICs attracted much interest, because these compounds show a wide range of physical and chemical properties. For example, the optical reflectivity of intercalated graphite has a transmission window associated with free carriers not present in graphite [8]. This increase of transmission is due to the increase of free charge carriers caused by the intercalant (confirmed by Hall measurements).

Intercalation improves the thermoelectric properties of graphite. A good thermoelectric material converts the thermal energy in electricity. The Seebeck coefficient for GICs is higher than for pristine graphite, therefore GICs show higher thermoelectric conversion factors [33]. This feature simply arises from the increase of charge carriers caused by the intercalation process.

Transport measurements on GICs show a logarithmic increase of the resistivity for decreasing temperature and a negative magneto-resistance for low magnetic fields (weak localization). These features are characteristic of two dimensional electronic behavior, and hence graphitic intercalation compounds show 2D behavior [34]. The increase of the interlayer distance (due to the presence of the intercalant species) decreases the coupling between the graphene layers and, thus, intercalated graphite behaves as a 2D material [8].

Finally, some GICs exhibit superconductivity. Depending on the intercalant the stoichiometry can vary from IC_6 to IC_2 (where I stands for intercalant) [29]. Superconductivity reveals only in stage 1 compounds. CaC_6 is the GIC with highest critical temperature ($T_C = 11.5K$) [35]. The nature of superconductivity in these materials is still under debate. Possible explanations are enhanced electron-phonon coupling due to high doping of the graphite-like σ-bands, charge density wave induced pairing or Cooper pair formation in the intercalant band [27, 29].

Chapter 2

Electrochemical doping

Free charge carriers have a strong impact on the physical properties of solid state systems. They determine the conductivity [6, 10, 25, 36], affect the optical absorption properties [10], allow for collective plasma oscillations [10], play a role in magnetism [37] and influence the transition temperatures in superconductors [38]. Therefore, tuning the carrier density in solid state systems over a wide range represents a powerful means for modifying their physical properties. Typically, the carrier concentration in solid state systems is tuned either by chemical doping or by using the electric field effect (FE).

Chemical doping is the intentional insertion of impurities in the crystal structure of a material [10] to generate additional free charge carriers. It should be distinguished from unintentional doping during the growth. For semiconductor single crystals this unintentional doping is usually on the order of 10^{16} cm^{-3} or less. This dopant concentration induces unwanted room temperature conductivity and may represent an important source of scattering. Intentional chemical doping is achievable with different methods: addition of dopants during the material growth, diffusion and implantation. The concentration of intentional dopants can be varied across a wide range of densities. Semiconductors doped with donor impurities (the dopant donates one or more electrons to the semiconductor) are defined as n-type, while those doped with acceptor impurities (the dopant takes on electron for the host material) are called p-type. The n and p type classifications specify which charge carrier acts as the material's majority carrier. The opposite carrier is called the minority carrier and may exist due to thermal excitation. It typically has a much lower concentration compared to the majority carrier. To the best of our knowledge, maximum chemical doping has been induced in silicon using boron and phosphorus (10^{19} cm^{-3}) [39, 40]. The incorporated atoms can occupy the interstitial sites in the crystallographic structure of the host material or they substitute atoms (see Figure 2.1-a). In both cases the crystallographic structure is distorted. Changes in the physical properties of the material should therefore not only be attributed to the change of charge carrier density, but possibly also to changes in the crystal structure of the material.

The carrier density in solid state systems can be modulated also by the field effect. A potential difference (called gate voltage V_G) applied between two (poor)

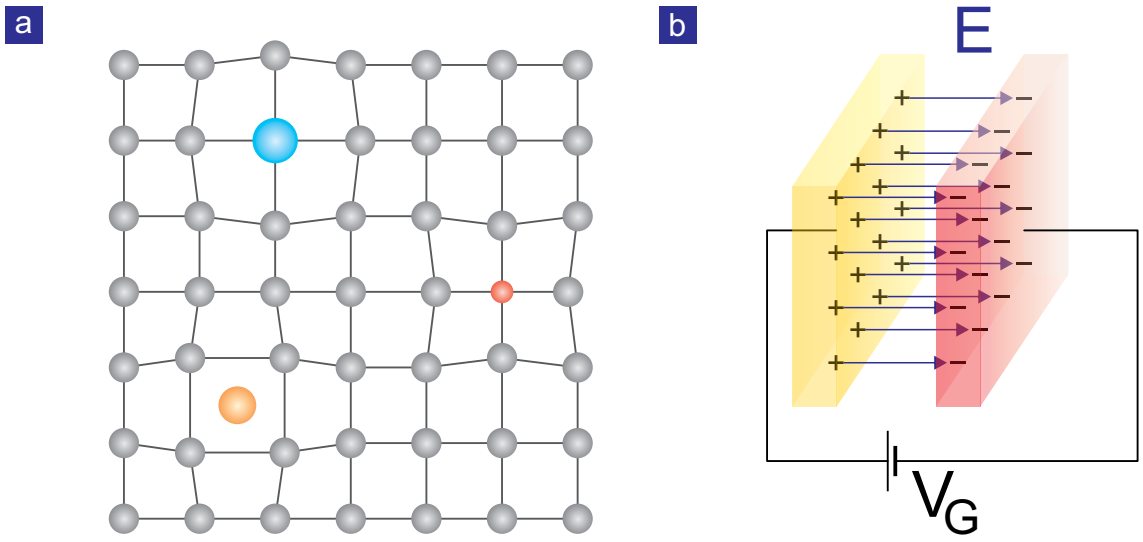

Figure 2.1: Defects due to chemical doping and working principle of a field effect transistor. (a) Defects on the crystal structure due to chemical doping: the blue circle represents a substitution atom bigger than the host atoms, while the red circle depicts a substitution atom smaller than the original one. Interstitial doping is shown with the orange circle. (b) Parallel plate capacitor: the two plates are represented by yellow (positive charged) and red (negative charged) parallelograms. The electric field between the plates E is represented by the blue arrows.

conductors (yellow and red parallelepipeds in Figure 2.1-b) separated by an electrical insulator causes charge accumulation at the conductor/insulator interfaces as in a parallel plate capacitor. The induced charge carriers are given by $q = \epsilon A V_G/d$, where ϵ is the permittivity of the insulator, A is the area and d is the distance separating the conductors. The charge modulation occurs only at the surface of the conductors, because the external electric field can penetrate only a short distance into a conducting material. In principle, the lateral induced charge distribution is homogeneous across the sample and the crystal structure of the material is unaffected. The maximum carrier density that can be induced by the field effect is limited by the permittivity of the insulator and the distance between the capacitor plates and is typically on the order of 10^{13} cm^{-2}. In contrast to chemical doping, field effect doping is not applicable to insulators. The main advantage of field effect doping is the in-situ tunability of the charge carrier density.

In this chapter, we discuss two possible physical realizations of field effect devices. We describe their operation. We start with a brief historical account of field effect devices in Section 2.1. A more recent implementation of a field effect device is the so-called electric double layer transistor EDLT). It relies on the use of an electrolyte as a dielectric medium. The physics of the electric double layer (EDL) transistor is presented in Section 2.2. The evaluation of induced charge carrier density in the channel can either proceed via the Hall effect (2.3.1) or by monitoring the ionic current in the electrolyte (2.3). Electrolytes can also be used to chemically dope the

channel. Section 2.4 describes the mechanism of electrochemical doping in 3D and layered materials. Finally, we give an overview of the different families of electrolytes used in electrolyte gating (2.5).

2.1 Historical account of field effect doping

The first field effect device was proposed by J. E. Lilienfeld in 1925 [41] and is the forefather of the metal-semiconductor field effect transistor (MESFET). The apparatus is shown in Figure 2.2-a. A thin film of a semiconductor (or poor conductor) is evaporated on the surface of an insulating substrate (gray box) and two electrically conducting electrodes (yellow parallelepipeds on the sides). Another electrode is placed in contact with the poor conductor within a fracture of the insulating substrate. By applying a voltage V_1 between the two electrodes on top of the substrate, an electric current I flows across the poor conductor. The application of a voltage V_2 between the electrode in the fracture and the negative pole of V_1 induces a modulation of the current due to the field effect.

In 1935 O. Heil proposed the junction field effect transistor (JFET) [42] where a thin film of a semiconductor is placed between two metal electrodes. On top of this heterojunction an insulator with high dielectric constant and a metal control contact are deposited. The voltage applied between the control electrode and the semiconductor tunes the charge accumulation in the latter and, therefore, its conductivity (similar to parallel plate capacitor in Figure 2.1-b). The first working JFET devices were produced by W. Schockley at Bell Labs in 1947.

A major breakthrough in field effect technology was the invention of the metal-oxide field effect transistor (MOSFET) by D. Kahng in 1959 [43]. The geometry of the MOSFET is sketched in Figure 2.2-b. The substrate is a monocrystalline semiconductor wafer (usually silicon) with a slightly n-doped bulk (azure area in Figure 2.2-b) and two p-doped portions near the surface (green sections is Figure 2.2-b). An electric insulator is evaporated on the surface of the wafer covering entirely the n-doped region and partially the p-doped areas (gray parallelogram of Figure 2.2-b). Three metal electrodes (typically gold) are evaporated: two on the p-doped regions and one on the oxide. A DC voltage V_{SD} is applied between the two contacts on the p-doped silicon. The electrode connected to the positive pole of the voltage source is called source (S), while the contact connected to the negative pole is referred to as the drain (D). A second DC voltage V_G is applied between the electrode on the insulating layer, called gate (G), and the drain. This voltage is referred to as the gate voltage. V_G is equivalent to the voltage applied between the plates of a capacitor: the metal and the slightly n-doped semiconductor are the two parallel plates separated by the insulator (see Figure 2.1-b). The change of V_G induces a variation of the charge accumulated at the plates. Since the pristine carrier concentration in the semiconductor is low, the field effect charge has a strong influence on the conductivity of the silicon at the surface. Therefore, the current flowing from S to D (due to the constant V_{SD}) changes drastically with the gate voltage.

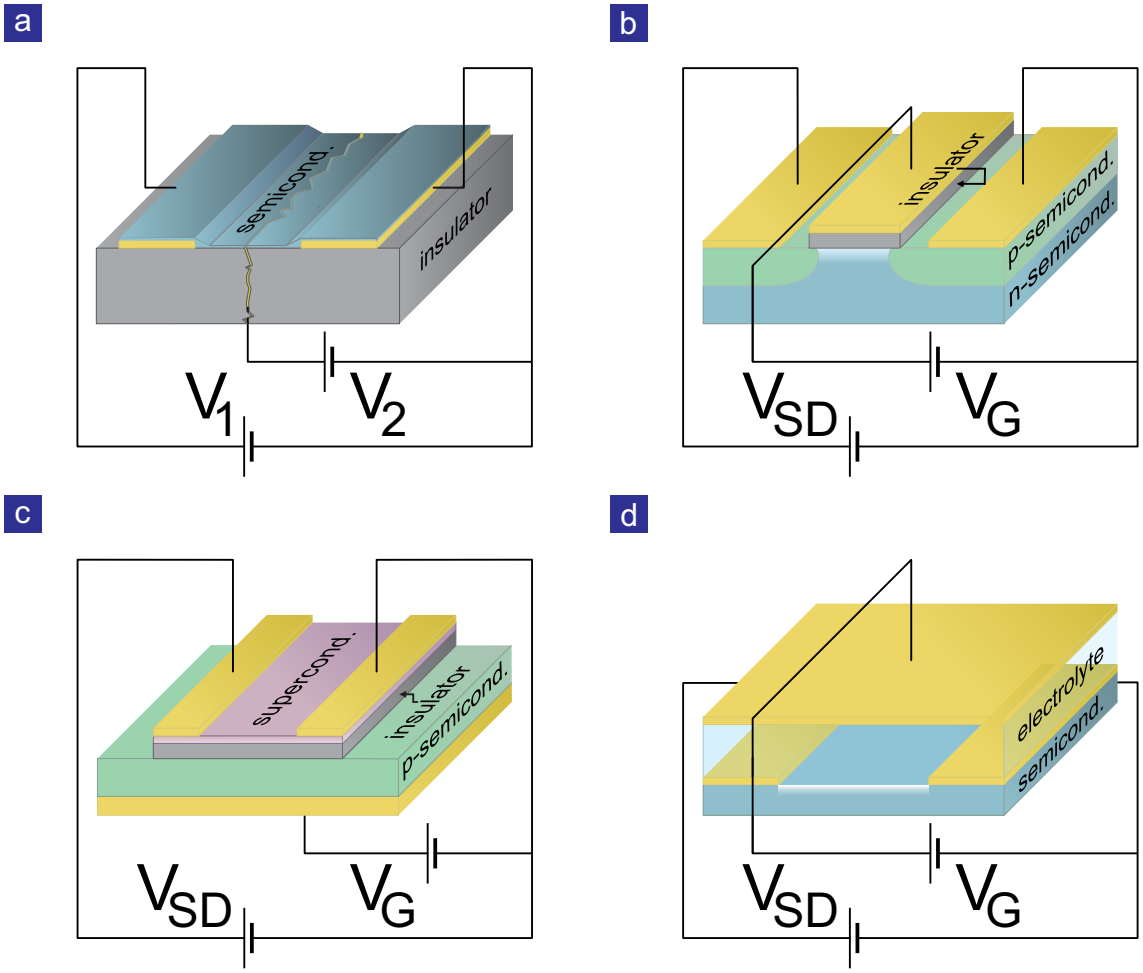

Figure 2.2: Different types of *FET*.(a) First field effect device proposed by Lilienfeld in 1925. (b) MOSFET geometry. (c) *FET* with superconducting channel. (d) Electrolyte based transistor. In every picture the yellow parallelograms depict the electrodes and the external electrical connections are shown.

Apart from their industrial relevance, field effect transistors have ever since attracted the attention of basic research. Field effect devices have been used to tune the carrier density in a wide range of materials including polymers [44], organic semiconductors [45], semiconductor nanowires [46] and superconductors [47]. Figure 2.2-c displays a FET with a superconducting channel. The change of carrier density in the superconductor due to the variation of V_G can induce a change of the superconductor critical temperature [47].

A second breakthrough in field effect based technology has been the electrolyte based transistor [48]. The basic principle of an electrolyte based transistor was already put forward at Bell Labs in 1955 [49]. In the 1980s reversible electrochemical oxidation was used to tune the conductivity of semiconducting polymers [50]. The first fully electrolyte gating based devices date back to the early years of this century

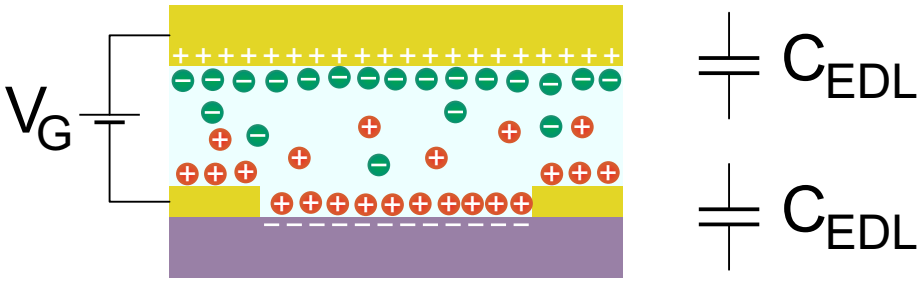

Figure 2.3: EDL transistor. Schematic drawing of an EDLT. Voltage source, cations (red circles) and anions (green dots) are presented. On the right side the two capacitors C_{EDL} depict the capacitance due to the EDLs.

[48, 51].

Electrolytes are materials that allow ionic conduction but do not permit electronic transport. Applying a DC voltage to an electrolyte by means of two metal electrodes induces a charge polarization at the electrode-electrolyte interface. This charge can vary the carrier concentration in the electrode and this effect can be used for the production of electrolyte based transistors (see Figure2.2-d). The basics of electrolyte gating are presented in more detail in sections 2.2 and 2.4.

2.2 Electric Double Layer gating

In electrolyte based transistors the dielectric material separating the gate electrode from the conductive channel is an electrolyte (see Figure 2.2-d). Electrolytes support ionic conduction rather than electron conduction. Hence, the gate electrode is electrically insulated from the channel of the transistor.

The application of the gate voltage V_G drives the anions to the positive pole of the voltage source and the cations to the negative pole. Assuming the ions can not enter into the two electrodes, they will accumulate at the interface of the electrolyte and the gate electrode as well as at the interface between the electrolyte and the sample. In Figure 2.3 a positive voltage is applied to the gate electrode: anions are attracted by the gate and cations are driven towards the surface of the studied material. The anions at the gate electrode-electrolyte interface simply screen the charges into the metal, while the cations at the sample-electrolyte interface attract electrons at the surface of the studied material. These two pairs of charged planes are called electric double layers (EDLs) and electrolyte based transistors are therefore also referred to as electric double layer transistors (EDLTs).

EDLs have been studied intensively, both theoretically [52–56] as well as experimentally [57]. EDLs occur at every interface between a solid and a fluid. An electrolyte can be viewed as an ionic fluid, therefore the surface charges of a solid can attract the counter ions immersed into the electrolyte (also) in the absence of

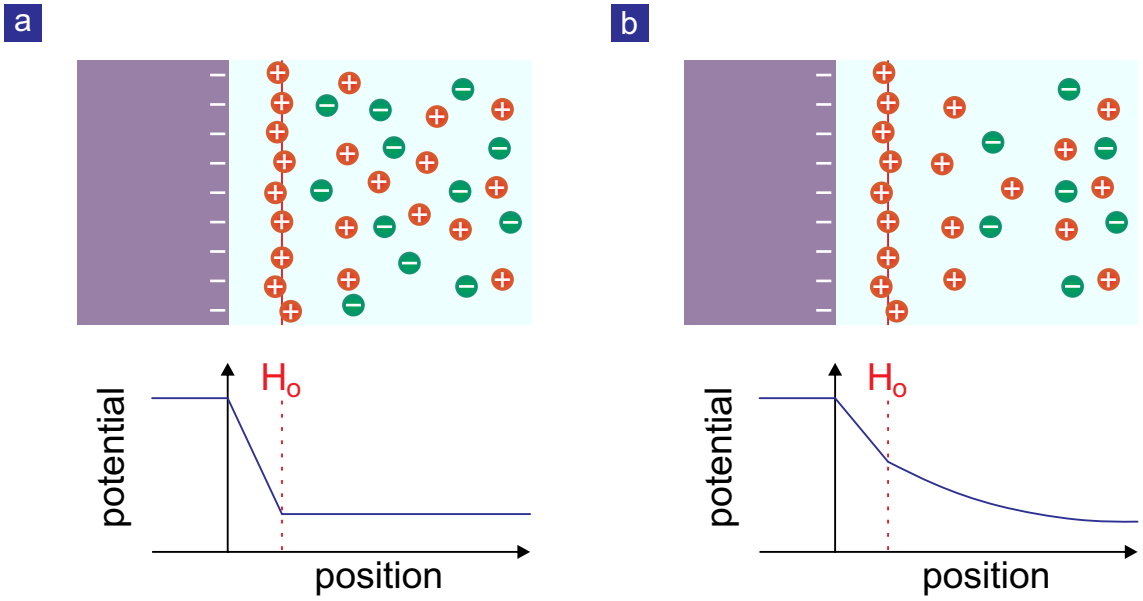

Figure 2.4: Formation and modeling of the electric double layer. Schematic representation and potential dependence of EDL within the Helmholtz [52] (a) and Stern [55] (b) theories. The position of the Helmholtz plane H_0 is represented.

an external applied potential [56] and an EDL forms. This kind of electric double layer is very weak and an external voltage is usually needed to accumulate a large number of charges at the electrolyte-solid interface.

The first model for EDLs was developed in 1853 by H. von Helmholtz [52, 56] and involves a rigid arrangement of ions which neutralizes the surface charges of a solid (see Figure 2.4-a). The ionic layer is called Helmholtz plane and is assumed to be located at a distance H_0 from the surface of the solid. The bulk of the electrolyte is charge neutral. Therefore, there is only a linear potential drop at the solid-electrolyte interface. The resulting capacitance of the electric double layer is given by:

$$C \simeq \frac{\epsilon_0 \kappa}{H_0} \tag{2.1}$$

where ϵ_0 is the permittivity of vacuum and κ is the effective dielectric constant of the EDL. The thickness of the double layer H_0 corresponds to the Debye screening length and depends on the ionic concentration in the electrolyte and the temperature [58].

The Helmholtz model implies a differential capacitance of the EDL independent of the electrode and the applied potential, which has however been experimentally confuted [57]. To circumvent this discrepancy between model and experiment a diffusive double layer has been introduced in 1924 by Stern [53–56]. The Helmholtz plane is no longer rigid, but the ions can diffuse into the electrolyte (see Figure 2.4-b). Therefore, there is a continuous charge gradient from the surface into the bulk of the electrolyte. The potential drops linearly between the solid surface and

the Helmholtz plane, like in a parallel plate capacitor, but there is an additional exponential decay of the potential from the Helmholtz plane into the bulk of the electrolyte that depends on ion diffusion. The diffusion of the counter ions depends on temperature, ionic concentration, ionic charge and applied voltage [53–56] . High temperature and low ionic concentration decrease the screening energy in the electrolyte bulk, therefore these conditions produce a wide diffusive double layer. In other words, electrolytes at low temperatures and with a large ion concentration form narrow Helmholtz layers and can generate a higher carrier concentration in the gated material.

2.3 Evaluation of the injected charge carrier density

The charge carrier density induced by EDLTs (n_{2D}) in the channel is the most important parameter for gating purposes. In electrolyte based devices n_{2D} can be obtained directly by measuring the Hall effect or by determining the charges participating in the EDL formation (double step chronocoulometry).

2.3.1 Hall effect

The Hall effect is the standard method to determine the carrier concentration in solid state systems [59]. The Hall voltage V_H is the potential difference that builds up transversely to the injected current I_S in an electrical conductor subjected to a magnetic field B perpendicular to the current (see Figure 2.5-a). V_H exclusively depends on physical properties of the material under investigation and is given by [10]:

$$V_H = -\frac{IB}{n_{3D}de}. \tag{2.2}$$

Here d is the thickness of the sample and n_{3D} is the three dimensional charge carrier concentration. The Hall voltage is inversely proportional to the charge concentration. So, high magnetic fields and currents are needed to experimentally determine n_{2D} in materials with very high carrier concentration(see Figure 2.5-a). For example, a 20 nm thick gold stripe exposed to a magnetic field $B = 10$ T shows a Hall voltage $V_H \simeq 10$ μV for an injected current $I_S = 1$ mA. Sometimes injecting high currents or applying high magnetic fields is not possible, so the Hall signal becomes extremely small and difficult to detect.

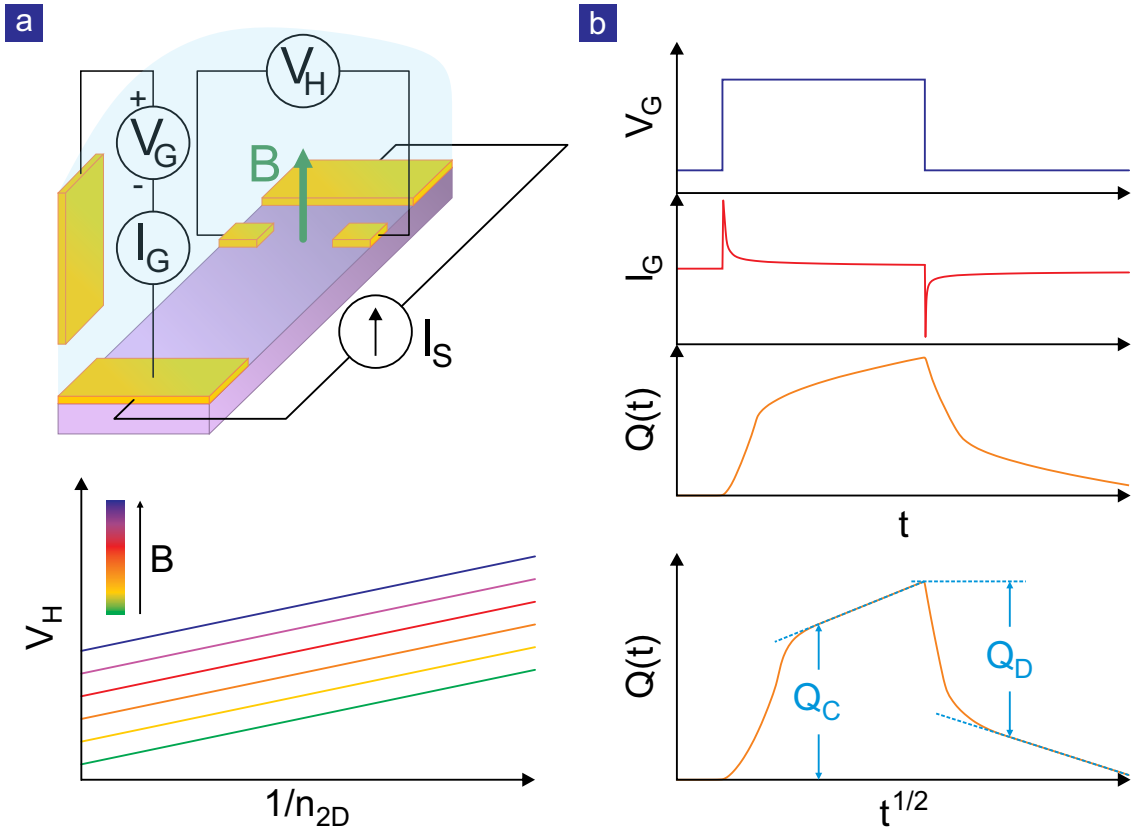

Figure 2.5: Hall effect and Double Step Chronocoulometry. (a) Experimental configuration for Hall effect measurements (top) and the dependence of V_G on carrier density for different strengths of magnetic field. (b) Procedure for Double Step Chronocoulometry.

2.3.2 Double step chronocoulometry

In an EDL the charges accumulated at the electrolyte surface q_{EL} are screened by the surface charges in the sample q_S [56]. Since the electric double layer is totally neutral, the charge in the Helmholtz layer and in the sample surface are equal ($q_S = q_{EL}$). Therefore, the charge carriers induced into the sample can be estimated from the number of ions forming the Helmholtz plane. The standard method to determine the charge participating to the Helmholtz plane is called Double Step Chronocoulometry (DSC) [60].

DSC relies on measuring the time dependence of the ionic current that flows when applying the gate voltage V_G to create the EDL (called gate current I_G). When V_G is applied the gate current immediately shows a peak (see Figure 2.5-b). Afterwards I_G decays with time. Integrating the ionic current with respect to time gives the total ionic charge (Q) displaced during the integrated time interval. The behavior of $Q(t)$ allows distinguishing between ions that form the EDL and the ion current that flows in the electrolyte bulk [60]. The electric double layer forms on a

short time scale and results in an exponential time dependence of Q. In contrast, electrochemical effects, such as the diffusion of electroreactants, happen on a longer time scale and produce a square root time dependence of the charge accumulation. Plotting Q vs.$\sqrt{t}$ allows identifying the end of the creation of the EDL. Subsequently, the involved charge Q_C (see Figure 2.5-b) can be evaluated.

The second step of DSC is removing the applied voltage and analyze the discharge of the EDL. The behaviors of I_G and Q with time are analogous to charging (see Figure 2.5-b). Q_D is the charge removed during the destruction of the electric double layer. If $Q_D = Q_C$ adsorption of reactants and chemical interaction between electrolyte and sample were absent [60].

The injected charge is $Q_{EDL} = Q_C = Q_D$ and the surface charge carrier density accumulated in the gated material is given by:

$$n_{2D} = \frac{Q_{EDL}}{eS}. \tag{2.3}$$

Here, S is the sample surface and e the electronic charge.

The penetration depth of the charges in the material can be classically estimated using the Thomas-Fermi approximation. Within this model, the screening length r_{TF} [10] is given by:

$$r_{TF} = \frac{\sqrt{a_0}}{2\sqrt[3]{n}}. \tag{2.4}$$

Here, a_0 is the Bohr radius and n the carrier concentration in the material. Typical values of the Thomas-Fermi screening length are 0.51 Å in gold, 0.55 Å in copper [10] and 2.5 Å in graphite [14]. Usually the penetration depth is assumed to be double the Thomas-Fermi length ($l_{scr} = 2r_{TF}$). Since chronocoulometry provides the total charge participating to the EDL (q_{EL}) and since the screening changes with the charge density of the material, evaluating n_{2D} is not trivial. A self consistent calculation of the screening length depending on the injected charge is needed to get a reliable estimate of the surface charge carrier density. Therefore, DSC is experimentally more easily accessible compared to the Hall effect, but requires a more complicated data analysis.

2.4 From electrostatic to electrochemical doping

In the previous sections we discussed the creation of ideal electric double layers in electrolyte based transistors with a channel impermeable to the ions in the electrolyte. In reality, most materials are permeable to these ions, therefore chemical modifications of the channel can occur [61].

Figure 2.6-a describes the dependence of the induced carrier density in the channel on the gate voltage. At $V_G = 0V$ the electrolyte is assumed to be unpolarized (yellow area of Figure 2.6-a). The EDLs do not form (see Figure 2.6-b). This is true only if the channel and the gate electrode are made of the same material, because only then the surface charge densities and the work functions are identical (as described in Section 2.2).

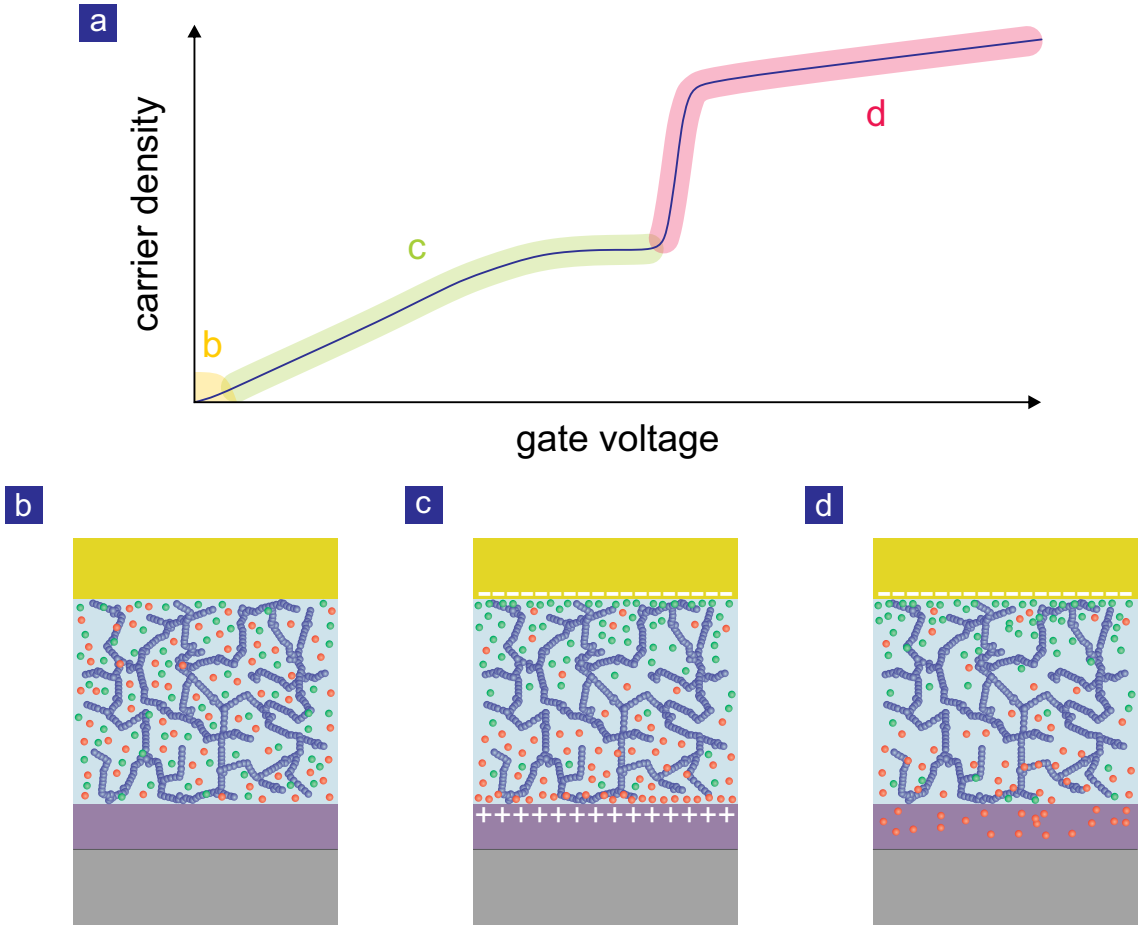

Figure 2.6: EDLT behavior from gating to electrochemistry. (a) Dependence of sample carrier density on the applied gate voltage. Three regimes are highlighted with different colors. The letters refer to other sections of the picture. Cartoons of: (b) unpolarized electrolyte, (c) electrostatic charge injection and (d) electrochemical reaction.

For low values of the gate voltage two EDLs form (see Figure 2.6-c) and charge carriers are induced in the channel (green line of Figure 2.6-a). To first approximation, the number of induced charges depends linearly on the gate voltage. The maximum carrier density depends on the maximum possible packing of the ions on the sample surface. The latter depends on the network that hosts the ions. When optimal packing is reached, a further increase of the gate voltage does not create any change in the induced carrier density (see Figure 2.6-b). To maximize the electrostatically induced charge, the electrolyte host material needs to be optimized. On one hand the host structure needs to be small and light to maximize the free space on the sample surface, on the other hand it has to be strong enough to stand the applied voltage and the resulting electric field. The compromise between free space and endurance gives the best electrolyte for gating purposes.

In perfect electrolyte-sample interfaces the migration of ions from the electrolyte to the channel is forbidden [56]. In reality, ions having high enough energy can penetrate into the specimen (see Figure 2.6-d). Therefore, a further increase of V_G causes the so-called electrochemical doping. This is detected by a strong and steep additional increase of the charge carrier density in the channel (red area of Figure 2.6-a).

The energy necessary for electrochemical doping depends on the gated material. In 3D materials the ions have to break the original chemical bonds and high energies are needed. In layered materials the ions can enter the crystal structure from the sides and diffuse into the host material without breaking any bond. Therefore the required energy for intercalation is smaller (see Paragraph 1.5). In both cases the doping process is reversible, even if the removing of dopants is not complete and occurs at a different energy than doping [61]. Therefore, electrochemical doping induces a structural change of the sample accompanied with an increase of the disorder (see the introduction of this Chapter).

2.5 Electrolytes

Every material in which exclusively ions conduct can be classified as an electrolyte. The most common electrolytes are fast ion conductors, polymer electrolytes and ionic liquids.

Fast ionic conductors (FICs) are materials where ions can freely move into a crystalline matrix of other ionic species [62]. A continuous ionic conduction paths is formed if there is always at least an empty ionic site for the ions to move in. Examples of fast ionic conductors are lanthanum fluoride (LaF_3), calcium titanate ($CaTiO_3$) and yttria-stabilized zirconia (YSZ).

Polymer electrolytes (PEs) are materials where ions can move through a polymeric host matrix [63]. PEs are produced dissolving inorganic salts in polymers [61]. Usually polymer electrolytes are soft and rubbery solids. The most used host polymer is poly(ethyleneoxide) (PEO). A large number of transporting ions can be used in this matrix, namely H^+, Li^+, Na^+, K^+, Ag^+ and Mg^{2+} [63]. Probably, the most common polymer electrolyte is (PEO) doped with lithium perchlorate ($LiClO_4$) [51,61].

Ionic liquids (ILs) are liquid salts. ILs are widely used in electrochemical devices, because they are non-volatile, non-flammable, thermally stable and show large ionic conduction [61]. Examples of ionic liquids are N,N-diethyl-N-(2-methoxyethyl)-N-methylammonium bis(trifluoromethylsulphonyl-imide) (DEME-TFSI) and 1-ethyl-3-methylimidazolium bis(trifluoromethylsulfonyl)amide (EMI-TFSA) [64,65].

Figure 2.7 shows the conductivity ranges for the different classes of electrolytes. Fast ionic conductors are crystalline materials, while polymer electrolytes and ionic liquids are amorphous. Therefore, FICs show the highest conductivity. Among the amorphous electrolytes ILs have higher conductivity than PEs, because the motion of ions into a liquid is easier than in a rubbery amorphous solid. At first sight, fast ionic conductors seem to be the best electrolytes for gating purposes: higher

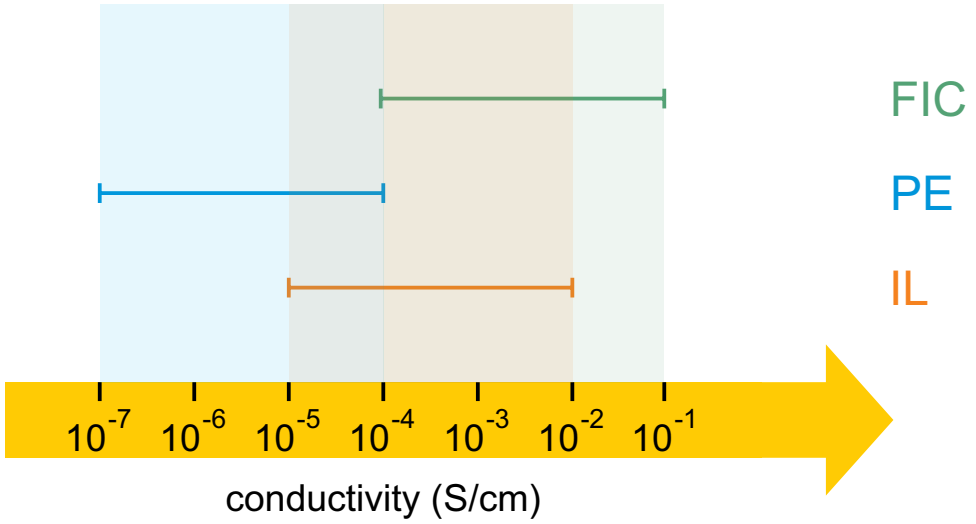

Figure 2.7: Ionic conductivity of different families of electrolytes. The orange, turquoise and green lines represent the conductivity ranges of ionic liquids, polymer electrolytes and fast ionic conductors, respectively.

polarization speed and higher order of the ions on the surface of the sample. Creating a FIC-bases device is however difficult, because the electrolyte and the sample need a very good contact. This is complicated to achieve between two solids with different crystal structures. Therefore, in practice FICs are not used for gating purposes. PEs are deposited on the sample in a liquid form. They then are solidified in situ [51,61], therefore polymer electrolytes are extensively used as gating mediums [6, 51]. Ionic liquids can be bought commercially, are easy to position on the sample and exhibit a large polarization speed. The disadvantages of these materials is however the necessity to confine them on the sample to avoid their motion [7] and the high number of phase transitions when cooled to cryogenic temperatures.

The choice between polymer electrolytes and ionic liquids is based on all the previous considerations. In particular, ionic liquids are predestined for high switching speed transistors working at room temperature, while polymer electrolytes are more appropriate for low temperature studies on small samples where the confinement of liquids is more difficult.

Chapter 3

Sample preparation

The production of electrolyte-gated graphene samples involves several steps. In this Chapter we summarize the fabrication process of our devices. We start by describing the most common approaches to produce single crystalline graphene (Paragraph 3.1). We divide the fabrication methods in bottom-up (Section 3.1.1) and top-down approaches (Section 3.1.2). Subsequently, we address common methods used to evaluate the thickness of graphene layers (Paragraph 3.2): the optical contrast (Section 3.2.1) and Raman spectroscopy (Section 3.2.2). Obtaining large graphene flakes with mechanical exfoliation and being able to position them precisely at a specific target location are important capabilities [3, 66, 67]. In Paragraph 3.3 we provide a detailed description of the precision transfer technique used for the production of our devices. Transferred graphene flakes possess a random shape. For studying the electronic transport properties, a Hall bar with a regular arrangement of the electrical contacts is highly desirable. Paragraph 3.4 describes all necessary fabrication steps. The last step involved in the device manufacturing is the placement of an electrolyte on the electrically contacted sample. Since our polymer electrolyte contains lithium, these operations are performed in the argon atmosphere of a dry glove-box (Paragraph 3.5). Once polymerized, the polymer matrix of the electrolyte protects lithium from interacting with the ambient atmosphere. The sample can then be taken out of the glove-box and the device can be mounted on the sample holder. Finally, all the steps of the sample preparation are summarized in Paragraph 3.6.

3.1 Graphene preparation

Micro- and nanomaterials can be synthesized through two different approaches: bottom-up ant top-down methods. The bottom-up approach consists in the creation of a material or a structure using the self-assembly properties of atoms or molecules. In other words, it relies on the construction of a specific structure starting from its elementary building blocks. The top-down approach counts on the possibility of shaping and structuring high quality bulk materials. Typical methods used in top-down approach are cutting, milling, etching, exfoliating and patterning.

In this Section we describe bottom-up (3.1.1) and top-down (3.1.2) approaches used in graphene fabrication. We give a basic overview of the most popular graphene fabrication methods highlighting the differences in sample quality and reproducibility.

3.1.1 Bottom-up growth of graphene

Graphene can be produced by means of several bottom-up approaches such as molecular beam epitaxy (MBE) [68,69], chemical vapor deposition (CVD) [70,71], thermal decomposition of silicon carbide [72–74] and the reduction of carbon dioxide [75]. Among all of these bottom-up methods, CVD growth and thermal decomposition of silicon carbide are the most common.

Chemical vapor deposition allows growing large graphene crystals (mono- and multilayers) on different metallic substrates. The CVD process relies on the thermal decomposition of hydrocarbon precursors in carbon radicals at the substrate. These radicals nucleate at specific points of the substrate giving rise to graphene (mono- and multilayer) crystals. The metallic substrates have a twofold function. They serve as a catalyst for the hydrocarbon decomposition and as a support for the graphene growth [71]. The carbon precursor can be a gas or a liquid. The most common metal substrates are foils of copper, nickel or platinum. The temperature of the reaction ranges from 800° C to about 1100° C depending on the metal substrate and the carbon precursor [71]. Figure 3.1-a depicts the principle of CVD growth of graphene on a Cu foil. A copper foil is heated up to approximately 1000° C in $H_2 - CH_4$ atmosphere. The substrate acts as catalyst for the dissociation of methane into carbon radicals and atomic hydrogen. The hydrogen atoms form H_2, while the carbon atoms cluster in specific areas of the copper foil and form the typical honeycomb crystal of graphene [76]. CVD growth allows obtaining large monocrystalline graphene patches (up to 1 mm^2), but the conducting substrate forces to transfer graphene onto an insulating substrate to make use of it [71]. This complicates the device fabrication. Another disadvantage of CVD grown graphene is the presence of defects (grain boundaries and vacancies) in the crystals [76].

Graphene synthesis based on the thermal decomposition of silicon carbide [72–74] relies on the higher vapor pressure of silicon compared with carbon. SiC is heated to 1300° C in ultra-high vacuum and a graphene layer is left on the SiC surface [72]. This graphene layer is called buffer layer and is strongly linked to the silicon carbide surface via dangling bonds (see top panel of Figure 3.1-b). There are several approaches to decouple the graphene layer from the substrate. The most successful methods are insertion of hydrogen between the buffer layer and SiC [74] and high temperature annealing [73]. The hydrogen intercalation method relies on the annealing of the sample at temperatures that range from $600°C$ o $1000°C$ in H atmospheric pressure [74]. The hydrogen saturates the dangling bonds of the substrate decoupling graphene from SiC (see the bottom-left panel of Figure 3.1-b). Alternatively, the buffer layer can be decoupled by thermal annealing at $1300°C$ the sample in ultra-high vacuum [73]. The graphene layer is separated from SiC and a new buffer layer is created (see the bottom-right panel of Figure 3.1-b). It is

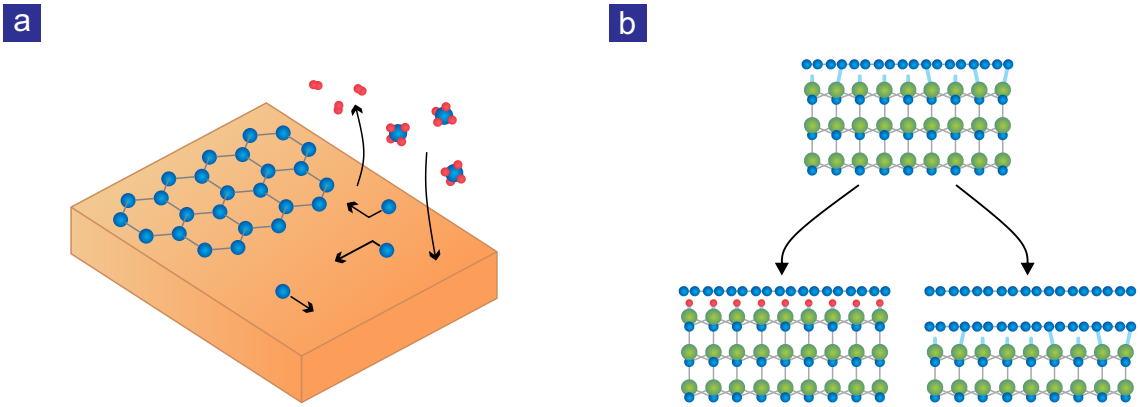

Figure 3.1: Schematics of *CVD* growth and thermal decomposition of silicon carbide. (a) Scheme of *CVD* growth of graphene on copper. Carbon atoms (blue dots), hydrogen atoms (red circles) and methane molecules (agglomerates of blue dot and red circles) are represented. (b) Model of graphene growth via *SiC* decomposition. Carbon atoms (blue dots), hydrogen atoms (red circles), silicon atoms (green dots) and interlayer dangling bonds (turquoise lines) are depicted.

important to notice that the graphitization process is not self-terminating and *SiC* is covered with patches of multilayer graphene of different thickness [72–74].

3.1.2 Top-down production of graphene

The top-down approaches for the synthesis of mono- and multilayer graphene consist in thinning down a natural graphite crystal or *HOPG* crystal. The most common methods are chemical [77] and mechanical exfoliation.

In chemical exfoliation, bulk graphite is intercalated with large molecules (see Section 1.5), therefore the coupling between the different graphene planes becomes weaker and the resulting material shows 2D character [8, 14]. One can chemically remove the intercalant species in order to obtain mono- and multilayer graphene flakes. For example, the sonication of potassium intercalated graphite (KC_6) immersed in ethanol (CH_3CH_2OH) allows obtaining monolayer graphene flakes and carbon nanoscrolls [77]. The nature, quantity and quality of these carbon nanomaterials are not well controllable, therefore this method has attracted limited interest in particular in the transport community.

Mechanical exfoliation is the most successful and widely used fabrication method for graphene. Its popularity stems from its simplicity. Indeed, mechanical exfoliation only relies on an adhesive tape and is also often referred to as the scotch-tape technique [1]. Since the graphite intra-layer covalent bonds ($524 kJ/mol$) are much stronger than the van der Waals inter-layer interactions ($7 kJ/mol$) [78], the graphene crystals can be easily separated. The complete mechanical exfoliation procedure is shown in Figure 3.2 (a)-(h). The fundamental ingredients are: a crystal of either

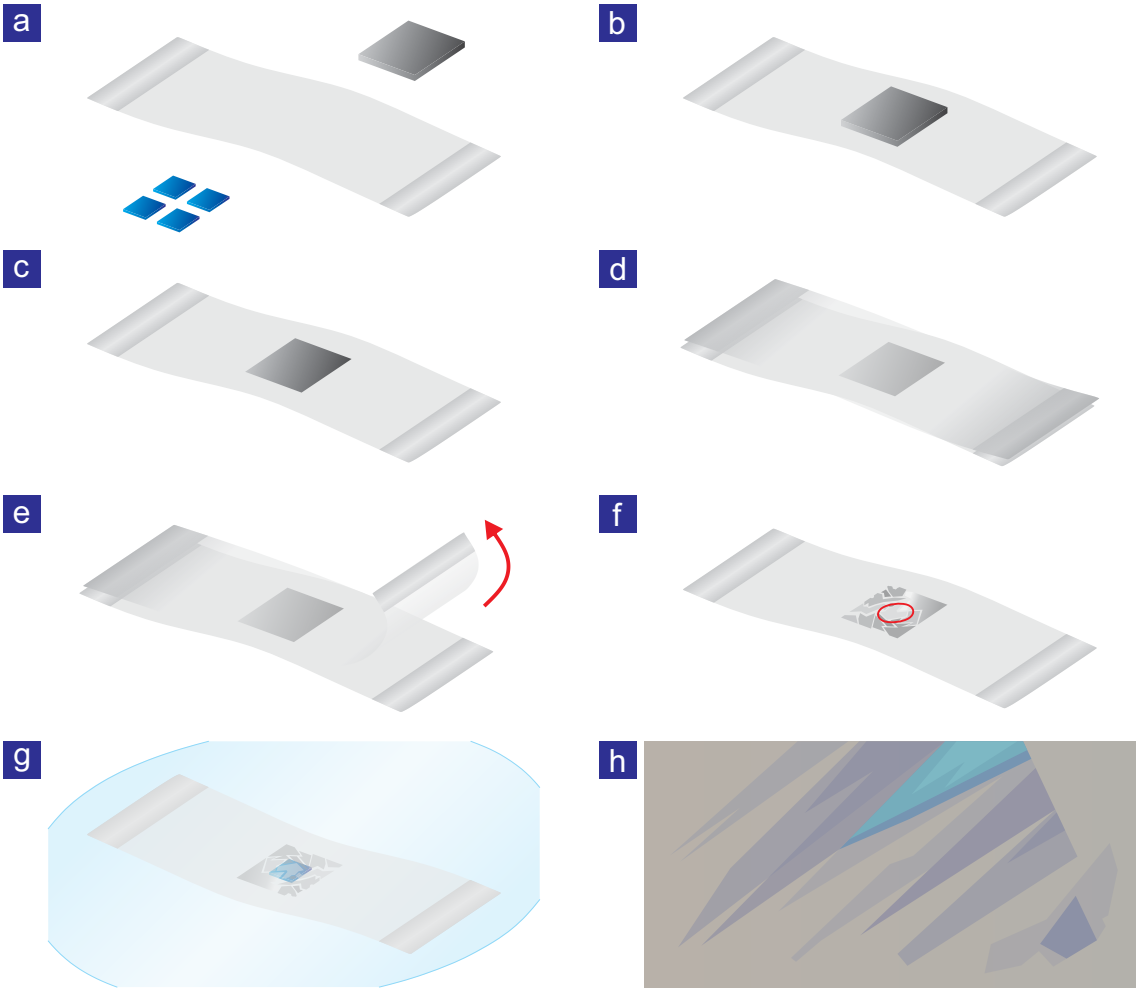

Figure 3.2: ***Schematic representation of the mechanical exfoliation method.***

highly oriented pyrolitic graphite (*HOPG*) or natural graphite, adhesive tape and a target substrates (see Figure 3.2-a). A piece of graphite is placed on a strip of adhesive tape and gently pressed against it. The graphite crystal is then removed with tweezers and its top layers are transferred to the scotch-tape (see Figure 3.2-b and -c). A second adhesive tape strip is placed on the thin graphitic layer and subsequently removed. A thinner graphite layer is transferred on the second tape. The repetition of these steps several times (from 5 to 10) allows obtaining areas of few layers of graphene on the final piece of scotch tape. These cleavage steps are performed by pressing and removing the tape always in the same direction.This helps to maximize the dimensions of the final graphene crystals. The graphitic thin regions can be identified as grayish areas (see Figure 3.2 form (d) to (f)). The tape with few layers graphene is gently pressed for a few minutes on an insulating substrate that has been pre-heated to 130° C. The pressure can be applied by placing the target substrate on the back of a pre-heated glass beaker in order to maintain a constant temperature for a longer time (see Figure 3.2-g). A higher temperature increases the

adhesion of graphene on the substrate, because the water molecules evaporate from the surface of the target. Different size and thickness graphene flakes are transferred to the substrate (see Figure 3.2-h). Typical dimensions of mechanically exfoliated graphene monolayers are $20 \times 20\ \mu m^2$. To remove the residuals of the glue coming from the scotch-tape, the substrate is cleaned in N-Ethylpyrrolidone (or N-Methyl-2-pyrrolidone), acetone and isopropanol. Finally, the substrate is dried with a nitrogen jet. Mechanical exfoliation allows obtaining the highest quality graphene samples. The charge carrier mobility is high and the defect concentration low [14]. Therefore, mechanical exfoliation is the preferred technique for basic research of transport in graphene and multilayer graphene.

3.2 Evaluating the number of layers

Since it is only one atomic layer thick, the detection of graphene is not obvious. The mechanical exfoliation method produces a random distribution of graphene flakes of different thickness (Section 3.1.1). In this paragraph we present the most common methods used to identify the layer thickness of flakes produced by mechanical exfoliation. Section 3.2.1 describes how to find graphene by optical microscopy. Raman is the second most common method used to evaluate the thickness of graphene crystal stacks. It is illustrated in Section 3.2.2.

3.2.1 Optical contrast of graphene

Since it is gapless, graphene is opaque. The opaticity of graphene and the increase of the optical path of the incident light where graphene is present, produces an optical contrast with respect to the bare substrate [1]. Figure 3.2-h shows a schematic of graphene layers with different thicknesses placed on a silicon wafer capped by 300 nm of silicon dioxide. The contrast of graphene depends on the number of layers, the substrate material and its thickness. The expected optical contrast can be modelled by simply using the Fresnel law [79].

The optical contrast is defined as the relative variation of the intensity of the reflected light from the substrate in the presence (I_{G+Sub}) and absence (I_{Sub}) of graphene:

$$C = \frac{I_{Sub} - I_{G+Sub}}{I_{Sub}}. \tag{3.1}$$

In order to calculate the intensity of the reflected light, the exact geometry of the substrate-graphene stack and the complex refractive index of all the materials need to be considered [79]. It is important to remember that the refractive index depends on the wavelength of the incident light [10, 25].

Suitable substrates usually consist of a doped semiconductor capped with a thin layer of an electrical insulator. In this case, the sample geometry consists of a semi-infinite semicondutor described by a complex refractive index $n_{semi}(\lambda)$, an insulator

characterized by thickness d_{ins} and refractive index $n_{ins}(\lambda)$, the graphene with thickness d_{gra} and refrective index $n_{gra}(\lambda)$ and surrounding ambient (air) characterized by a refractive index n_0. In this geometrical configuration, the intensity of the reflected light in the presence of graphene is given by [79]:

$$I(n_{gra}) = \Big|\big(r_1 e^{i(\Phi_{gra}+\Phi_{ins})} + r_2 e^{-i(\Phi_{gra}-\Phi_{ins})} + r_3 e^{-i(\Phi_{gra}+\Phi_{ins})} + r_1 r_2 r_3 e^{i(\Phi_{gra}-\Phi_{ins})}\big) \times \big(e^{i(\Phi_{gra}+\Phi_{ins})} + r_1 r_2 e^{-i(\Phi_{gra}-\Phi_{ins})} + r_1 r_3 e^{-i(\Phi_{gra}+\Phi_{ins})} + r_2 r_3 e^{i(\Phi_{gra}-\Phi_{ins})}\big)^{-1}\Big|^2. \tag{3.2}$$

Here, the relative reflection indices are defined as:

$$\begin{aligned} r_1 &= \frac{n_0 - n_{gra}}{n_0 + n_{gra}}, \\ r_2 &= \frac{n_{gra} - n_{ins}}{n_{gra} + n_{ins}}, \\ r_3 &= \frac{n_{ins} - n_{semi}}{n_{ins} + n_{semi}}, \end{aligned} \tag{3.3}$$

and the phase shifts of the reflected light due to the changes in the optical paths are given by:

$$\begin{aligned} \Phi_{gra} &= 2\pi n_{gra} g_{gra}/\lambda \\ \Phi_{ins} &= 2\pi n_{ins} g_{ins}/\lambda. \end{aligned} \tag{3.4}$$

The intensity of the reflected light in the absence of graphene is given by Equations 3.2, 3.3 and 3.4 with $n_{gra} = n_0 = 1$.

The assumption of a semi-infinite semiconductor is acceptable, since its thickness is much larger than the wavelength of the incident light as well as its penetration depth. The model fails if the thickness of the oxide layer is many times the wavelength of the incident light ($d_{ins} \gg \lambda$), since the light coherence is lost.

Real graphene devices are usually produced using a silicon wafer capped by silicon dioxide [1]. Figure 3.3-a shows the contrast of monolayer graphene on silicon dioxide as a function of the thickness of the SiO_2 and of the wavelength of the incident light. At a fixed silicon dioxide thickness, the contrast of graphene strongly varies with λ (especially for thicker SiO_2), because the refractive indices strongly depend on the wavelength. In the visible light range (400 nm - 700 nm), the maximum contrast occurs for a silicon dioxide layer of about 80 nm. The second maximum shows up at about 300 nm of SiO_2.

A 300 nm thick silicon dioxide layer ensures good visibility and good endurance of the dielectric to an applied electric field [14, 23]. Therefore, we concentrate further investigations of the graphene visibility on this thickness of the dielectric. The optical contrast of graphene increases with the number of layers (see Figure 3.3-b). The increment is sub-linear, i.e. the contrast of N-layer graphene is not simply given by N times the contrast of monolayer graphene ($C(N) \neq N \cdot C(1)$). The

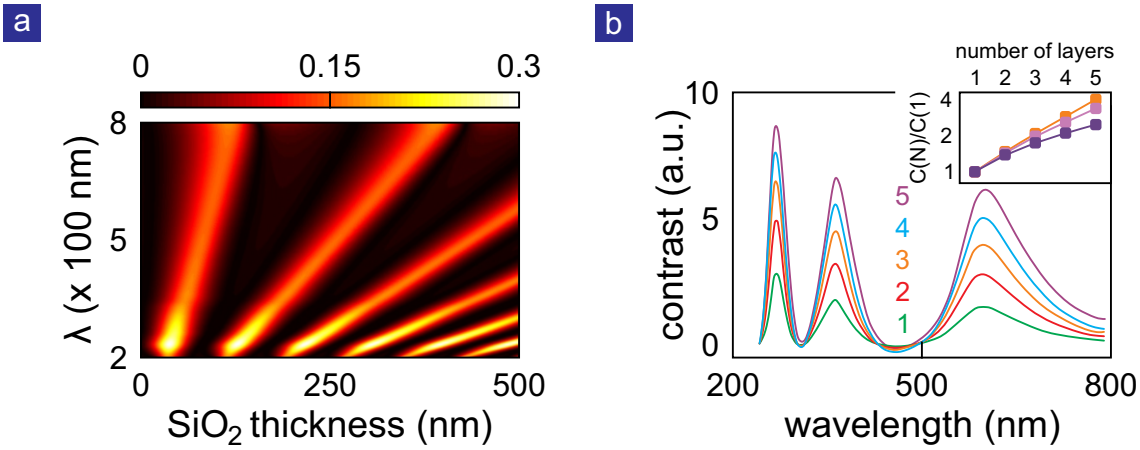

Figure 3.3: Calculated optical contrast of graphene on SiO_2. (a) Optical contrast of monolayer graphene deposited on silicon dioxide as a function of the oxide thickness and the wavelength of the incident light. (b) The wavelength dependence of the optical contrast of few layer graphene on 300 nm SiO_2. The inset shows the variation of the optical contrast for the maxima at 260 nm (dark violet), 360 nm (lilac) and 605 nm (orange) of incident light with the number of layers.

sub-linearity of the contrast on the number of layers is illustrated in the inset to Figure 3.3-b for all the maxima. It is interesting to note that these maxima in the optical contrast behave almost linearly with the number of layers N, if N is small. A direct evaluation of the graphene thickness is possible by measuring the optical contrast, if the number of layers does not exceed 5. For thicker graphene samples, only a rough estimate of the thickness is possible.

3.2.2 Raman spectroscopy of graphene

In Raman spectroscopy the back-emitted light by the sample is detected and its wavelength and intensity are analyzed. Part of the emitted light has the same wavelength as the incident light. It is attributed to elastic scattering (Rayleigh scattering). The remaining emitted light has different frequencies (higher or lower) than the incident radiation, because its emission involves inelastic scattering of photons [80]. Possible excitations giving rise to Raman scattering are phonons, plasmons, crystal defects, excitons etc.

Figure 3.4-a shows the Raman spectra of graphite and monolayer graphene acquired at 514 nm. The graphite spectrum is composed of three peaks: the so-called G-peak at 1583 cm^{-1}, the peak at $\sim$ 2700 cm^{-1} referred to as $2D$ peak and the G^*-peak centered at 3250 cm^{-1} [81]. Monolayer graphene shows the same three peaks of graphite at approximately the same positions. Therefore the Raman features of graphite and graphene share the same origin [82].

The G Raman peak is generated by scattering of incident photons with the Raman active lattice vibrations. This scattering is a single photon process that

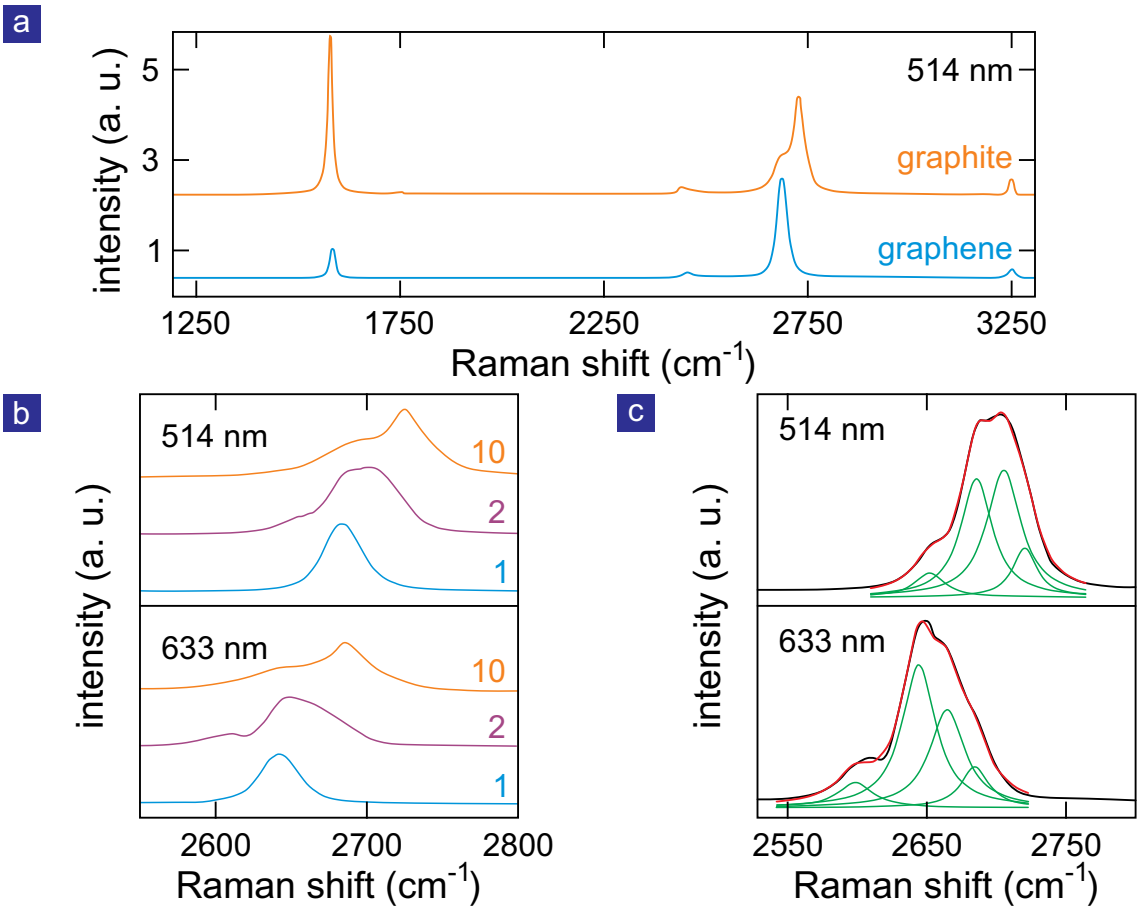

Figure 3.4: Raman spectroscopy of graphene. (a) Raman spectra of monolayer graphene and graphite acquired at 514 nm. (b) Comparison of the $2D$ peak for mono-, bi- and ten-layer graphene acquired at 514 nm and 633 nm. (c) $2D$ peak of bilayer graphene measured at 514 nm and 633 nm. The red lines depict the fitting of the peak and the green lines show the components of the fit.

happens at the doubly degenerate zone center Γ [81,82]. Graphene and graphite have four possible vibrational modes (see Figure 3.5-a). A_{2u} and E_{1u} are infrared active modes [83] and describe translations of the whole graphene (graphite) crystal [8]. B_{2g} represents an acoustic phonon where the atoms of the two sublattices vibrate perpendicularly to the plane in opposite directions. All these three vibrational modes are Raman inactive and, therefore, do not participate in the creation of the G peak. The only Raman active vibrational mode is E_{2g} mode, which corresponds to an in-plane vibration of the lattice, where the carbon atoms of the A and B sublattices vibrate in opposite direction [8, 83]. The G peaks of graphene and graphite show a comparable intensity [82]. In Figure 3.4-a the spectra are renormalized in order to obtain a similar intensity of the $2D$ peaks. The G peak of graphene is slightly red-shifted compared to the graphite one, because graphene's the G peak is strongly affected by charge doping [84].

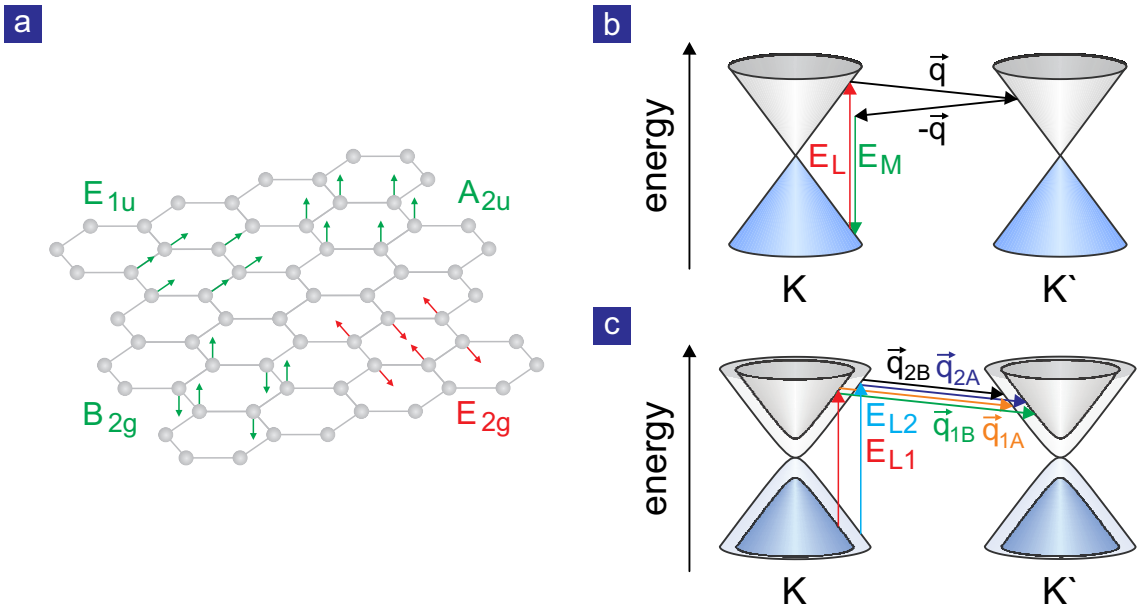

Figure 3.5: Origin of the Raman peaks of mono- and bilayer graphene. (a) Raman inactive (green) and active (red) lattice vibrations of graphene. (b) Double resonance mechanism of monolayer graphene. (c) Double resonance mechanisms in bilayer graphene. The energy of the incident light, allowed scattering mechanisms and emitted light are depicted.

The G^* peak is the second order harmonics of the E_{2g} vibrational mode. The frequency of G^* is greater than the double of the frequency of the G mode ($f_{G^*} > 2f_G$), because there is an overbending of the longitudinal in-plane Raman active band near the zone edges [81].

The $2D$ peak in the Raman spectrum allows one to differentiate between mono-, bilayer graphene, and graphite [82]. Figure 3.4-b compares the Raman $2D$ peaks of mono-, bi- and ten-layer graphene acquired for two different wavelenghts of the incident light: 514 nm and 633 nm. The spectrum of ten-layer graphene is very similar to the graphite one [13, 14]. The $2D$ Raman feature of graphene is composed of a single, sharp component roughly four times more intense than the G-feature (see Figure 3.4-b). In bilayer graphene, the $2D$ Raman feature is much broader and blue shifted. It consists of four different lines (as shown in Figure 3.4-c) with two of them having higher intensity than the other two. In ten layer graphene (graphite), the $2D$ peak is broad (it is formed by two components) and is blue shifted with respect to the $2D$ line of mono- and bi-layer graphene (see Figure 3.4-b). In the remainder of this section we explain these layer dependent changes in the $2D$ feature.

A common feature of the $2D$ peak independent of the number of layers is the shift with the wavelength of the incident light (see Figure 3.4-b). This dispersive nature of the $2D$ Raman band can be explained by the underlying double resonance (DR) process that connects the energy of the incident light to the band structure of the system [85]. The DR process in graphene occurs between the energy states near

the K and K' points in the first BZ and involves four steps: (1) an electron-hole pair is excited by the incident light of energy E_L (depicted as red vertical arrow in Figure 3.5-b), (2) inelastic electron-phonon scattering of momentum ($\mathbf{q}$) causes a transition from the Dirac cone centered at K to the one at K', (3) inelastic electron-phonon scattering with opposite momentum ($-\mathbf{q}$) induces a change from the Dirac cone centered in K' back to the one at K, and (4) the electron-hole pair recombines by emitting a photon of energy (E_M). The Raman shift is twice the energy of the interacting phonon. Since the energy and momentum need to be conserved, the Raman frequency depends on the energy of the incident light (see Figure 3.4-b). The $2D$ peak of monolayer graphene is formed by a single peak [82].

The electronic dispersion of bilayer graphene near the Dirac point involves four bands, two π bonding and two π^* antibonding bands centered around the edge points K and K' of the first BZ. As a result there are four allowed double resonance paths in bilayer graphene (see Figure 3.5-c) that are characterized by a different energy. Hence, the splitting of the electronic bands causes the four contributions to the $2D$ peak (shown in Figure 3.4-c) [82]. In graphite there are only two allowed electron-phonon scattering paths generating a double resonance [81], therefore the $2D$ peak of graphite is formed by two lines only (see Figure 3.4-b). The dispersive nature of the $2D$ peak of bilayer graphene and graphite has the same origin as in monolayer graphene.

In conclusion, Raman spectroscopy is a powerful tool to determine the thickness of single and multilayer graphene samples. It is possible to distinguish the number of layers up to five layers [82]. Therefore, this tool can be used together with the optical contrast method (Section 3.2.1) for the selection of suitable flakes for device fabrication.

3.3 Transfer technique

The ability to precisely position graphene on top of other materials paves the way for the production of vertical van der Waals heterostructures. For instance, graphene can be placed on top of hexagonal boron nitride (h-BN) to increase the charge carrier mobility [66, 86, 87] and screen the fluctuating potential background of the silicon dioxide substrate [88]. A small angle between the isomorphic crystal structure of graphene and h-BN creates a periodic Moiré pattern and, in the presence of a magnetic field, gives rise to the so-called Hofstadter butterfly [3, 89, 90]. More complex van der Waals heterostructures of graphene, hexagonal boron nitride and molybdenum disulphide (MoS_2) are conceivable and it has even been speculated that such stacks can be used as fast and flexible memories [91].

In the literature, a wide variety of different transfer techniques have emerged during the last few years. The first attempts were performed using graphene flakes mechanically exfoliated on silicon dioxide. Poly(methyl methacrylate) (PMMA) was spin-coated on the substrate and the SiO_2 was etched away. Then, the graphene flake on the PMMA membrane was precisely aligned to the target position under an optical microscope [67]. The main disadvantage of this method arises from residuals

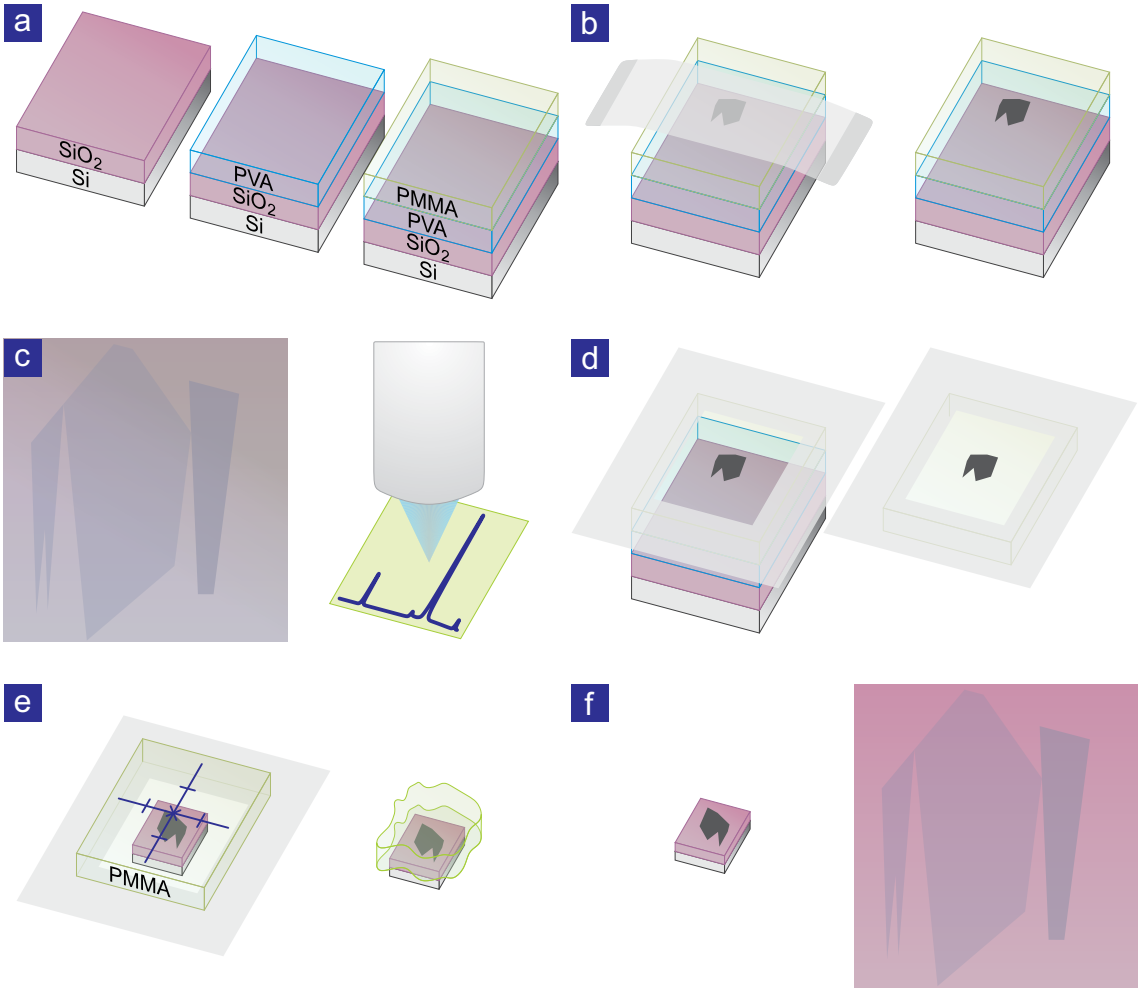

Figure 3.6: ***Schematic illustration of the transfer technique.***

of silicon dioxide remaining on graphene. To overcome this problem, many techniques involving mechanical exfoliation directly on a polymer layer [66, 86, 87, 90] have been developed. A sacrificial layer is placed between the silicon dioxide and the polymer supporting the graphene. It is dissolved in order to have a transparent membrane through which optically detect the graphene position is possible. The transparent polymer membrane is used to press the graphene on the target and is dissolved at the end of the transfer process [66,86,87]. In this paragraph, we describe the specific transfer technique we have used in the fabrication of our devices.

In this work, polyvinyl alcohol (PVA) has been used as sacrificial layer and PMMA as the support polymer layer. PVA can be dissolved in water, while poly(methyl methacrylate) is hydrophobic and floats on a water surface. The PMMA support layer can be lifted from the water surface, turned upside down and can be held in order to transfer the graphene on the target. A more detailed description of the steps involved in this transfer method follows:

1 - Spin-coating of PVA and PMMA on Si/SiO_2 substrate. A 2 cm × 2 cm SiO_2 substrate is cleaned in an O_2 plasma for 20 minutes (P = 200 W at a pressure of 0.4 mbar). Immediately after removal out of the plasma system, a solution of DI water and polyvinyl alcohol (H_2O : PVA = 100 ml : 5 g) is spin-coated on the substrate (rotation speed 6000 rpm for 40 s). The substrate is baked at 130° C for 2 minutes to solidify the PVA layer (90 nm thick). Then PMMA (200 K, 5%) is spin-coated on the PVA layer (rotation speeds 3000 rpm for 5 s and 8000 rpm for 30 s). Finally, the substrate is backed again at 130° C for 2 minutes to solidify the PMMA layer (200 nm thick). The total thickness of about 300 nm makes the graphene visible by optical microscopy (see Section 3.2.1). Figure 3.6-a shows schematically the different steps described above.

2 - Mechanical exfoliation of graphene on SiO_2/PVA/PMMA stack. The substrate and a petri dish are heated up to 130° C for several minutes to evaporate water. This is known to improve the adhesion of graphene. Graphene is mechanically exfoliated onto the warm substrate (placed on the petri dish to maintain temperature above ambient) as explained in Section 3.1.2. Figure 3.6-b shows the substrate during and after exfoliation.

3 - Search for graphene on the substrate. The substrate is scanned under an optical microscope to find graphene flakes using the optical contrast (Section 3.2.1). To double check the graphene thickness, Raman spectroscopy (Section 3.2.2) is performed on the optically selected graphene flakes (see Figure 3.6-c). Finally, an individual flake is selected.

4 - Release of PMMA/graphene stack form the SiO_2 substrate. A plastic transparent and flexible frame is glued with double-sided tape on the sides of the substrate paying attention to leave the chosen graphene flake uncovered (see Figure 3.6-d). The substrate/frame structure is placed floating on the surface of warm (70°C) DI-water. After a wait time ranging from a few minutes to several hours, the PVA layer is dissolved by the warm water. Then, the SiO_2 substrate sinks and the PMMA/graphene-frame structure floats on the water surface. Hence, graphene is never in contact with water.

5 - Placement of graphene on the target. A target 4×4 mm^2 SiO_2 substrate is placed on a homemade aligner and heated up to 110° C to evaporate the water adsorbed on the surface. The flexible frame is glued on a transfer stage. The transfer stage is positioned above the target substrate with the graphene facing down. Graphene is precisely aligned to the target. The distance between SiO_2 substrate and PMMA membrane is slowly decreased (taking care to keep the alignment). When the membrane touches the substrate, the PMMA layer can be cut away around the sides of the target substrate (see Figure 3.6-e).

6 - Improvement of graphene adhesion and cleaning of the substrate. The freestanding PMMA layer frequently exhibits wrinkles. They can decrease the adhesion to the target substrate and the transferred graphene washes away when the PMMA is removed. To avoid this problem, the substrate is heated

up to 160°C for 10 minutes before the cleaning procedure. Most of the wrinkles disappear and the graphene strongly sticks to the substrate. The substrate is cleaned in cold acetone (3 h), N-Ethylpyrrolidone (or N-Methyl-2-pyrrolidone) at 65° C for 4 hours, cold acetone (10 minutes) and cold isopropanol (10 minutes). At the end of this procedure, the graphene flake is lying on the clean target substrate (see Figure 3.6-f).

Exfoliating graphene on PMMA has a second, important advantage. Since PMMA is strongly hydrophobic the mechanically exfoliated flakes tend to be larger than the ones directly exfoliated on silicon dioxide. In particular, the monolayers mechanically exfoliated on PMMA are one order of magnitude bigger in size than the ones produced on silicon dioxide. Therefore, we have also used this transfer technique to produce graphene samples on normal SiO_2.

3.4 Device fabrication

In order to study the transport properties of graphene, it is necessary to fabricate electrical contacts.

We start form an arbitrarily-shaped, mechanically exfoliated graphene flake on a SiO_2 substrate (see Figure 3.7-a). The fabrication steps to produce a well defined Hall bar geometry are shown in Figure 3.7-(b)-(f). A PMMA layer is spin-coated on the substrate and the desired shape is exposed by electron beam lithography (EBL). The exposed PMMA can be dissolved in Methyl Isobutyl Ketone (MIBK). The PMMA remaining on the surface acts as a mask (see Figure 3.7-c). The area of graphene not covered by PMMA is removed by reactive ion etching (RIE). Subsequently, the PMMA mask itself is removed by immersing the sample in warm (65°C) NEP (or NMP) for four hours. Then, the sample is cleaned in cold aceton and isopropanol, and it is dried with a nitrogen jet. Finally, the sample is annealed at 350° C for several hours in forming gas atmosphere ($p \sim 150$ mbar) to remove the residues of PMMA.

The steps to fabricate contacts are shown in Figure 3.7-(g)-(l). A double layer of PMMA is spin-coated on the substrate. Contact patterns are exposed with electron beam lithography, then PMMA is developed. To improve the electrical contact between the leads and graphene, the substrate is placed in an oxygen plasma oven for a few seconds ($p \sim 400$ mbar, $P \simeq 200$ W and $t \sim 4$ s) prior to the deposition of the metallic layers. Then, 5 nm of chromium and 30 nm of gold are thermally evaporated in vacuum ($p < 10^{-6}$ mbar). Subsequently, the PMMA is removed as well as the metal lying on top (lift-off) by immersing the sample in warm (65°C) NEP (or NMP) for four hours. The sample is further cleaned in a flow of acenton and isopropanol. It is dried in nitroget jet. Finally, the sample is annealed at $\simeq 350°$ C for several hours in forming gas atmosphere ($p \sim 150$ mbar).

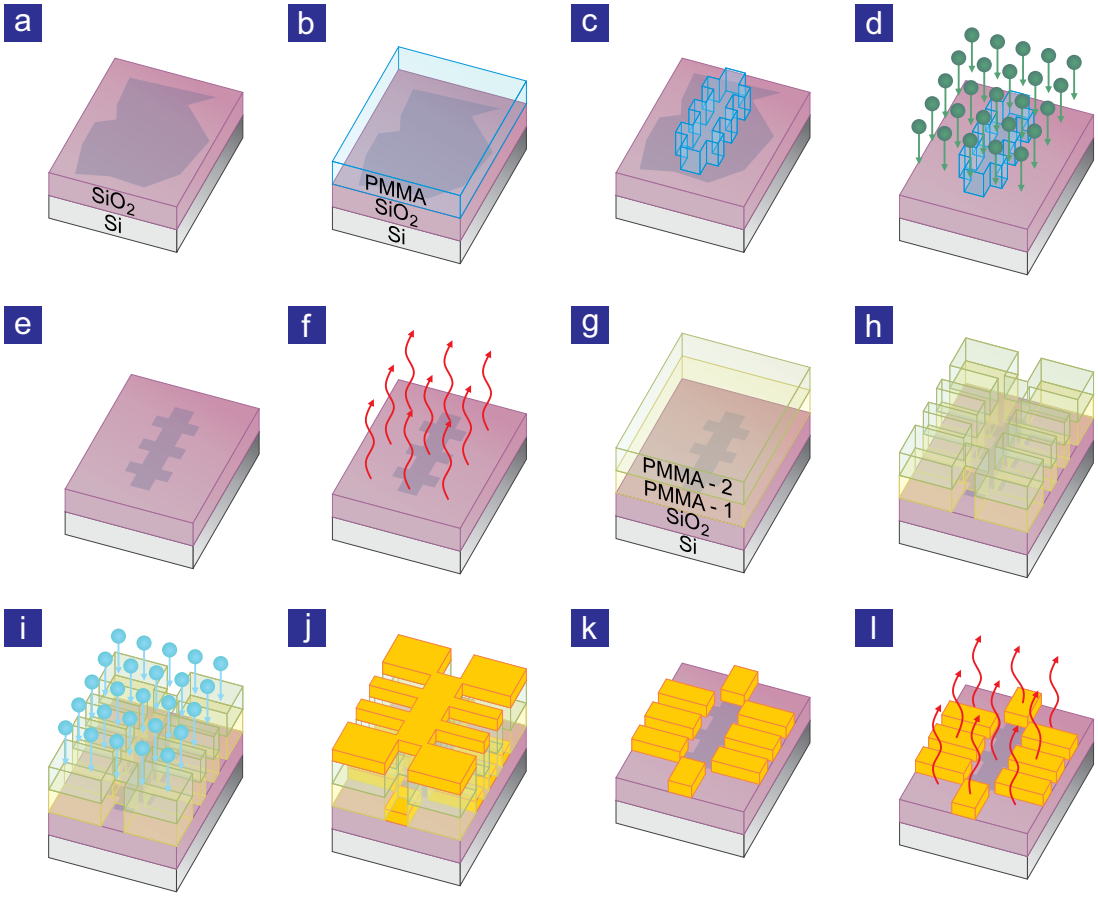

Figure 3.7: Schematic of the various fabrication steps to create electrically contacted graphene devices.

3.5 Electrolyte preparation

Although many ionic liquids are available on the market, for our studies we choose a homemade polymer electrolyte. As explained previously, polymer electrolytes are particularly suitable for low temperature studies of small samples. Furthermore, the non-volatility of PEs played an essential role in our choice.

The polymer electrolyte is produced by UV-curing a reactive mixture of ethoxylate dimethacrylate (BEMA, average M_n: 700), poly(ethylene glycol)methylether methacrylate (PEGMA, average M_n: 475) and lithium bistriuoromethanesulfonimidate (LiTFSI) in the presence of a free radical photo-initiator (Darocur1173) [6,92]. The photo-chemical curing is performed with a 4 W UV lamp. All operations involving the electrolyte are performed in the controlled Ar atmosphere of a glove box, because lithium strongly reacts with oxygen and nitrogen. Here we briefly describe the detailed recipe to make the electrolyte and to position an electrolyte drop on the sample:

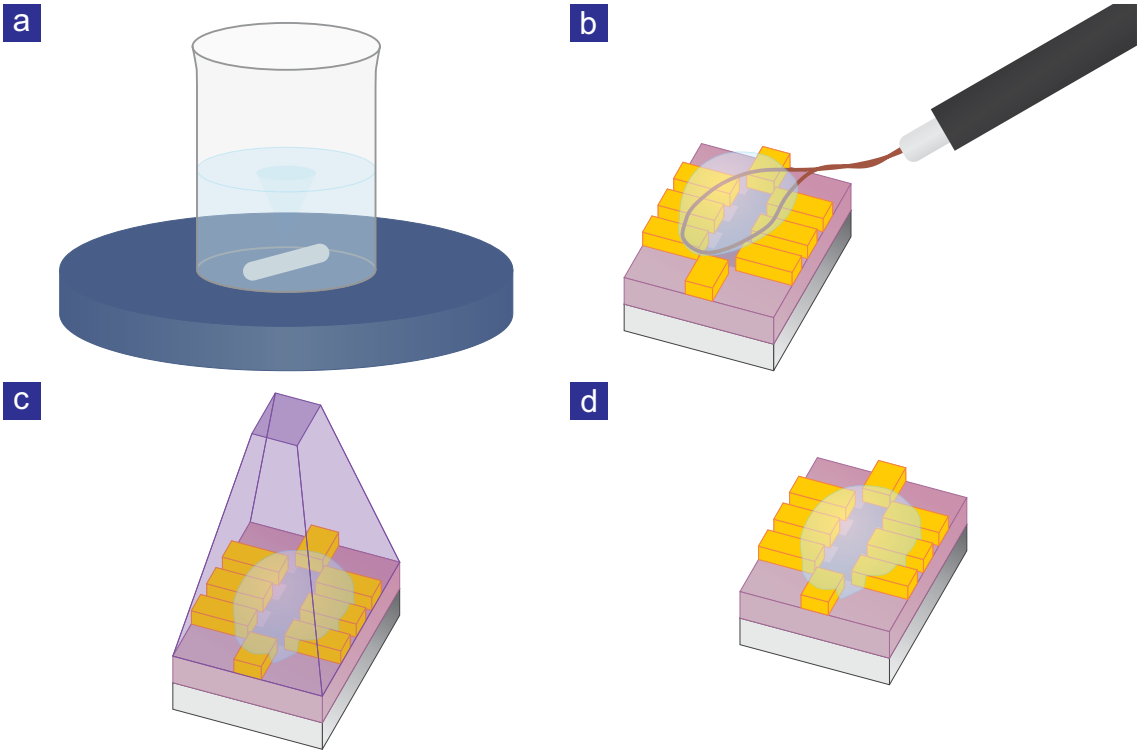

Figure 3.8: Schematic representation of preparation and deposition of the electrolyte on the sample.

1 - Mixing of the chemicals. BEMA and PEGMA are viscous liquids and are mixed with a magnetic stirrer in a 7 : 3 ratio for 10 minutes. Then, the 10% in weight of LiTSFI is added and the solution is mixed until the lithium-based salt is completely dissolved (approximately after 20-30 minutes). Finally, the 3% in weight of the photo-initiator is added and the solution is mixed for another 5 minutes.

2 - Placement of the electrolyte on the sample. The electrolyte is precisely positioned with a thin metallic wire bended into a submillimeter hook(see Figure 3.8-b). This wire is mounted on a pen-like holder and dipped into the electrolyte solution. After retracting from the solution, a small drop remains on the metallic wire. Using the pen-like holder and a microscope with a long focal distance objective, the drop is placed onto the sample. It can be precisely shaped and moved further with the same hook if necessary.

3 - UV curing of the electrolyte. The sample is placed under a 4 W UV-lamp (see Figure Figure 3.8-c). The distance between the lamp and the electrolyte is around 35 cm. The electrolyte is cured for 3 minutes. The electrolyte then has turned into a rubbery solid. The polymer network (created by the curing) prevents the chemical interaction of lithium with the ambient atmosphere and the sample can be taken out from the glove box and mounted on the sample

holder.

3.6 Summary of the fabrication procedures

Finally, we give a coarse overview of all the steps needed to produce an electrolyte-gated graphene device in Figure 3.9-(a)-(f).

Graphene is mechanically exfoliated (Section 3.1.2) on a PVA/PMMA stack (a). Then, the substrate is scanned under an optical microscope to find graphene flakes (Section 3.2.1). The thickness of suitable candidates is double checked by Raman spectroscopy (Section 3.2.2). The selected graphene sheet is precisely transferred (c) on a target position of a Si/SiO_2 substrate (Paragraph 3.3). The flake is patterned in a geometry suitable for transport measurements, and electrical contacts are fabricated (Paragraph 3.4) by means of EBL. Then, an electrolyte drop is placed on top of the graphene (e) in a dry glove box (Paragraph 3.5). Finally, the sample is inserted in a sample holder suitable for electronic transport experiments (f).

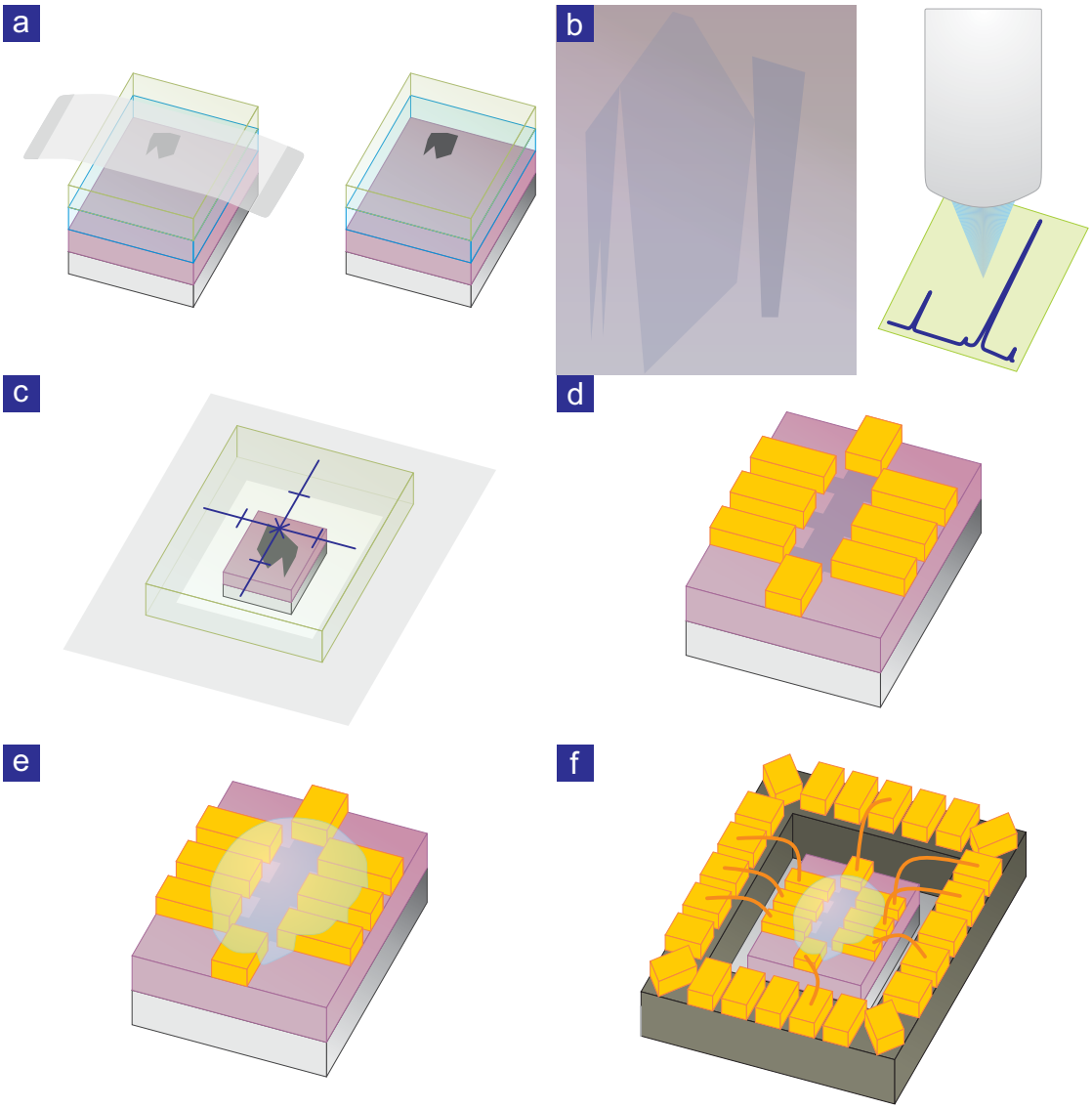

Figure 3.9: Summary of the fabrication of electrolyte-gated graphene devices.

Chapter 4

Charge concentration studies on electrolyte gated graphene

Electrolyte gating of graphene is a rather new topic in solid state physics. Several groups have carried out charge transport studies [93–95]. None of those works have analyzed in detail the dependence of the charge injection on sample thickness and substrate composition. In particular, non-linearity and zero-magnetic field offsets in the Hall traces were not addressed in these experimental works nor the data analysis.

In this Chapter, we present Hall measurements performed on electrolyte gated mono-, bi- and multilayer graphene. Paragraph 4.1 describes the measurement technique and the experimental details used to record the data. In Paragraph 4.2, the dependence of the charge injection on the applied gate voltage is examined. Particular attention is paid to the linearity of the Hall trace and sample thickness dependencies. Three different regions in n versus V_G are identified: hole doping at zero gate voltage (Paragraph 4.3), linear increase of the charge carrier density for low applied gate voltages (Paragraph 4.4), and a decrease of n for higher values of V_G (Paragraph 4.5). The non-monotonic gate voltage dependence of the injected charges is attributed to charge trap states at the surface of the insulating substrate (Section 4.5.1). The interaction between the charge carriers in graphene and the traps in the substrate can be used to perform spectroscopy of the supporting insulator and get information about the oxide quality and stoichiometry (Section 4.5.2). Finally, we discuss the hysteresis in the charge concentration when increasing and decreasing the gate voltage (Paragraph 4.6).

4.1 Measurement technique

In order to keep track of the charges induced by electrolyte gating in graphene, we have performed Hall measurements for different values of gate voltage. The electrostatics of the electric double layer (i.e. electric field screening) is expected to change with the sample thickness. Therefore, we studied mono-, bi- and multilayer graphene.

Measurements were conducted at room temperature, because the electrolyte

freezes at lower temperatures. This implies that the ions become immobile and a change of gate voltage does not affect the strength of the electric double layer. The temperature was kept constant by two separate feedback loops. The temperature of the variable temperature insert (VTI) of a He-4 cryostat was kept constant at 300 K. The samples were placed in a closed and evacuated sample rod, because a gas flow can damage the device. Only a small amount of He exchange gas (in the order of 10^{-2} mbar) was inserted into the sample space to have a better thermalisation of the sample. The sample rod contains a temperature sensor and a dedicated heater both placed in the vicinity of the sample. Since the heat exchange between VTI and sample is not perfect, the temperatures of VTI and sample are slightly different. Therefore, the second control loop in the sample rod allows us to keep the temperature of the sample constant.

Standard low-frequency ac lock-in techniques were employed with a 100 nA ac-current oscillating at frequencies ranging from 10 Hz to 15 Hz. The small current prevents heating of the sample, since graphene can sustain current densities up to 1 mA/μm without breakdown [96]. The ac signal decouples the electronic transport in graphene from the ionic conductivity of the electrolyte, because the ionic dynamics is slower (see Section 2.3).

The magnetic field was swept from positive to negative values. This prevents mistakes in the evaluation of the carrier density, because small displacements of the opposing Hall probes as well as inhomogeneity may cause an offset in the Hall signal at zero magnetic field. Also same non-linear behavior is present in the Hall trace with respect to magnetic field [97].

4.2 Hall measurements on electrolyte gated graphene

The Hall traces of monolayer graphene are shown in Figure 4.1. At zero gate voltage the transverse resistance is linear with magnetic field. The negative slope of $R_H(B)$ reveals the hole nature of the conducting charges [10, 25]. By increasing the gate voltage, we are able to tune the charge transport from hole- to electron-type. For $V_G = 0.1$ V the slope of R_H is still negative, but the Hall trace is non-linear. Non-linear Hall traces are commonly attributed to multiband conduction or an inhomogeneous distribution of charges across the sample [97]. Since in graphene a single band participates to transport, our measurements reveal that our samples are characterized by spatially separated conducting channels. Furthermore, the Hall trace at $V_G = 0.2$ V shows inversion and suppression of the Hall coefficient. The inversion can be explained by the change of the majority carriers from hole to electrons. The non-linear Hall trace and the suppression of R_H can be attributed to the simultaneous presence of electron and hole channels in the device [10, 25, 97].

By further increasing the gate voltage, the Hall trace becomes linear again (see Figure 4.1). This suggests that the charge inhomogeneity decreases for increasing V_G. Linearity is never perfect, because the charge distribution across the sample remains to some extent inhomogeneous. The slope of the transverse resistance versus magnetic field decreases with increasing gate voltage and the electron concentration

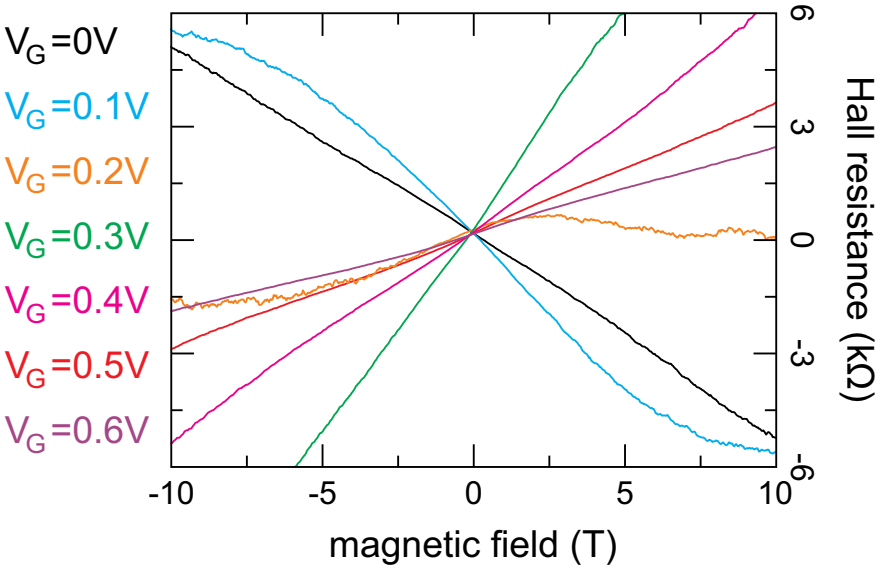

Figure 4.1: Hall traces of electrolyte-gated monolayer graphene. The Hall resistance is plotted against the magnetic field for different values of gate voltage.

as expected. The charge concentration n is the average of the values determined from the slopes of the Hall traces at high positive and negative magnetic field. This allows us to minimize the uncertainty and avoid problems due to the Hall voltage offset at zero field [97].

The gate voltage dependence of n and R are plotted in Figure 4.2. Initially, the sample is hole doped. When increasing the gate voltage, cations start to accumulate at the graphene surface and electron doping is induced in the sample. The charge neutrality point is located between $V_G = 0.2$ V and $V_G = 0.3$ V. Here,the strong non-linear Hall trace indicates that electron and hole channels are simultaneously contributing to conduction.

For gate voltages up to 1.6 V, the electron concentration increases almost linearly with V_G (see Figure 4.2). Accordingly, the longitudinal resistance decreases. A further increase of gate voltage causes a rather sudden decrease of the charge carrier density and a rise of the longitudinal resistance. Finally, at high values of gate voltage ($V_G > 2.1$ V) n rises again and this is accompanied by a drop of R as well.

In order to understand the complicated behavior of the charge carrier concentration with gate voltage, we have performed the same kind of measurement on bi- and multilayer graphene samples. The thickness of the multilayer samples is about 7-10 layers. It is difficult to determine the thickness more accurately, because the optical contrast [79] and Raman spectroscopy [82] methods fail for flakes with more than 5 layers (see Paragraph 3.2). Figure 4.3 shows the dependence of carrier density and longitudinal resistance on gate voltage of bi- (a) and multilayer (b) graphene. In agreement with monolayer graphene, both bi- and multilayer graphene are hole-doped at $V_G = 0$ V. The initial hole doping in bilayers is substantially higher than

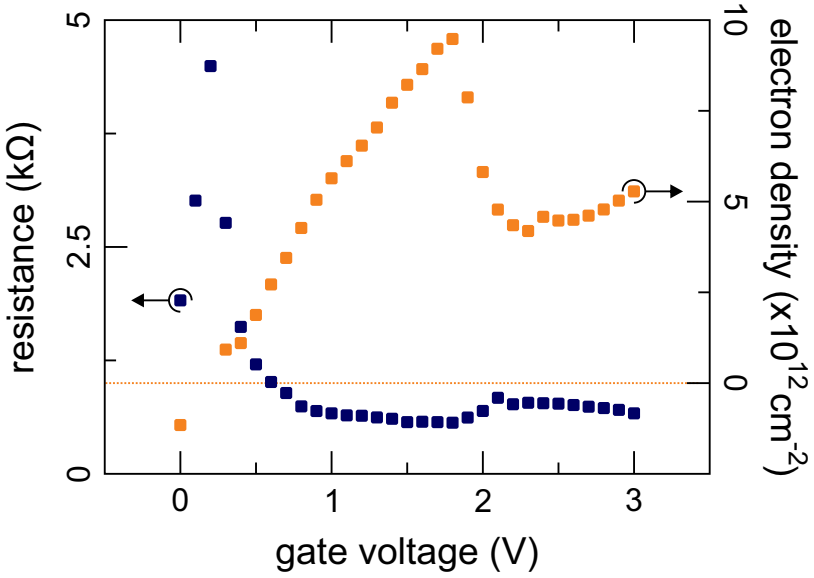

Figure 4.2: Resistance and carrier density of monolayer graphene. Longitudinal resistance (blue squares) and induced carrier density (orange squares) are plotted against gate voltage for a monolayer graphene sample.

in monolayer graphene. It is not possible to reliably determine the carrier density at $V_G = 0$ V in multilayer graphene. The hole doping in multilayer graphene can be extracted from the behavior of the longitudinal resistance. Figure 4.3-b shows that the minimum conductivity point is located around $V_G = 0.1$ V. Therefore, at zero gate voltage holes are the majority charge carriers contributing to transport.

At higher values of gate voltage, n increases quite linearly with V_G both in bi- and multilayer graphene. This is in agreement with the behavior of monolayer graphene devices (see Figures 4.2 and 4.3). Bilayer graphene shows a decrease of the carrier density (and increase of resistance) in the range 2.1 V$< V_G <$2.5 V. A further increase of the gate voltage causes a rising carrier density and a lowering of the longitudinal resistance. Multilayer graphene behaves differently from mono- and bilayers. The induced charge carrier density increases monotonically for all values of the gate voltage (see Figure 4.3-b). The longitudinal resistance of multilayers exhibits a non-monotonic dependence on the carrier density. This behavior has already been observed in trilayer graphene. It has been attributed to the filling of a new band [94].

From the Hall measurements performed on mono-, bi- and multilayer graphene, three main conclusions can be drawn:

1. At zero gate voltage in all cases hole doping is observed.
2. At low gate voltage the density increases linearly.
3. In mono- and bilayer graphene, the density changes non-monotonically at high V_G.

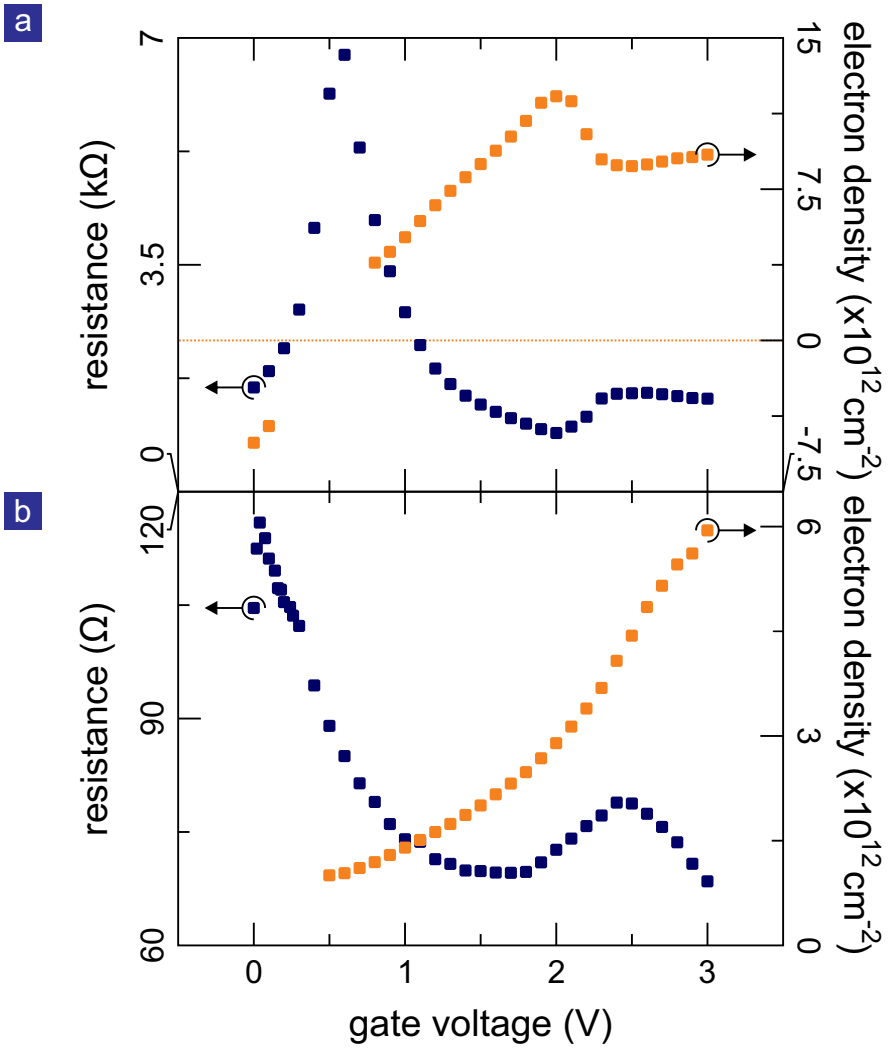

Figure 4.3: Resistance and carrier density of bi- and multilayer graphene. Longitudinal resistance (blue squares) and induced carrier density (orange squares) are plotted against gate voltage for (a) bi- and (b) multilayer graphene.

These observations are treated and explained in the next sections. In Paragraph 4.3 the reasons of the initial hole doping are described. The linear dependence of n with gate voltage is addressed in Paragraph 4.4. Finally, the sudden decrease of charge concentration with increasing V_G is discussed in Paragraph 4.5.

4.3 Hole doping at zero gate voltage

All the samples (mono- bi- and multilayers) are hole doped at zero gate voltage. We will show here that the sign of the initial doping can be explained by the difference in surface charge concentration of the sample and the counter electrode.
As pointed out in Paragraph 2.2, an electric double layer forms at every interface

between an electrolyte and a solid. When the sample and the counter electrodes are made of the same material, the charge accumulation at the interfaces with the electrolyte is very small (see Figure 4.4-a). The formation energy of such EDL is about 25 meV for graphite immersed in a lithium based electrolyte [56]. Therefore, the potential drop across the bulk of the electrolyte is approximately zero and no net ionic current flows.

When two different materials are connected by an electrolyte, two strong electric double layers form at the interfaces [56,60]. This feature is related to the difference in surface potential (and surface charges) between different materials and happens also if the electrodes are externally kept at the same potential [98]. The material with more negative surface potential (electron charge density) attracts cations and repels the anions towards the surface of the second electrode. EDLs form at the interfaces of the electrolyte and the two electrodes (see Figure 4.4-b). The strength of the electric double layers is proportional to the difference of the surface potential between the two electrodes.

The electrodes are externally kept at the same potential, therefore the potential difference created by the electric double layer formation needs to be compensated by an opposite voltage drop in the bulk of the electrolyte. This is depicted in Figure 4.4-b. The voltage drop across the electrolyte implies the flow of an ionic current. The current increases during the EDLs formation and saturates to a constant values when the ionic distribution at the interface is in equilibrium [98]. Since the surface potentials are weak, the electric double layers form on a long time scale and the ionic current increases for severals minutes, as shown in Figure 4.4-b.

In our samples, one electrode is made of graphene (mono-, bi- or multilayer) and the other of gold. Au shows a high and negative surface charge density [10]. Graphene lying on silicon dioxide is most frequently p-doped. This is due to adsorbed water molecules and residuals of lithography resist [99]. Therefore, the cations immersed into the electrolyte move towards gold and anions proceed towards the graphene surface. This explains the initial hole doping of graphene when it is kept at the same potential as the Au counter electrode (see Figure **??**). Furthermore, the ionic current measured in our devices at zero gate voltage is negative (compensating the EDLs potential) and saturates after the complete formation of the EDLs (see the lower panel of Figure 4.4-b). Therefore, we can attribute the initial strong hole doping of our samples to the high surface charge carrier density of the Au counter electrode compared to graphene.

4.4 Linear electron doping with gate voltage

As pointed out in Paragraph 4.3, in our devices the free charge carriers at zero gate voltage are holes. The anions of the electrolyte are located near the sample surface as illustrated schematically in Figure 4.5-b. All the further arguments of this section are based on monolayer graphene, but they are still valid for bi- and multilayers.

Increasing the gate voltage, cations are attracted from the sample and anions move towards the counter electrode. For $V_G < 0.5$ V, cations substitute only par-

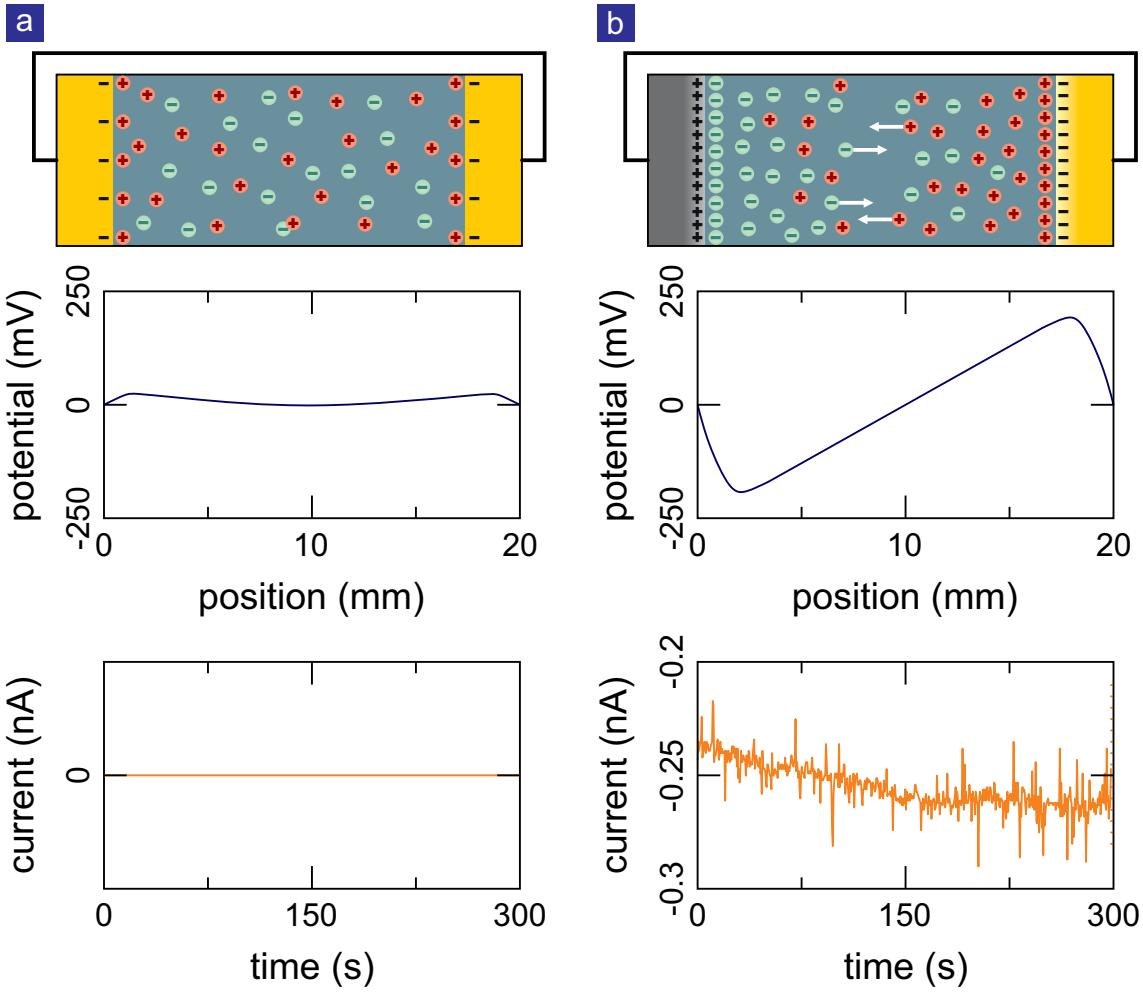

Figure 4.4: Ionic configuration in a battery with shortcut electrodes. Schematic representation of ionic distribution, spatial distribution of the potential drop and time dependence of the ionic current at $V_G = 0$ V for devices with two electrodes of the same material (a) and different materials (b).

tially the anion near the sample surface (as shown in Figure 4.5-c). Therefore, the sample is divided in areas characterized by hole and electron doping. This regime is commonly called the electron-hole puddle regime [100].

Substrate induced electron-hole puddles in monolayer graphene close to the MCP have been studied by scanning single-electron transistor measurements [100], scanning tunneling microscopy [101], magneto-transport [102] and Kelvin probe force microscopy of different substrates [88]. For graphene deposited on silicon dioxide, the different methods are consistent in reporting a typical strength of the charge fluctuations on the order of 10^{11} cm^{-2} [88, 100–102]. The use of boron nitride as insulating support seems to decrease the charge inhomogeneity by at least one order of magnitude [88].

Since in electrolyte gated graphene the arrangement of ions changes with gate

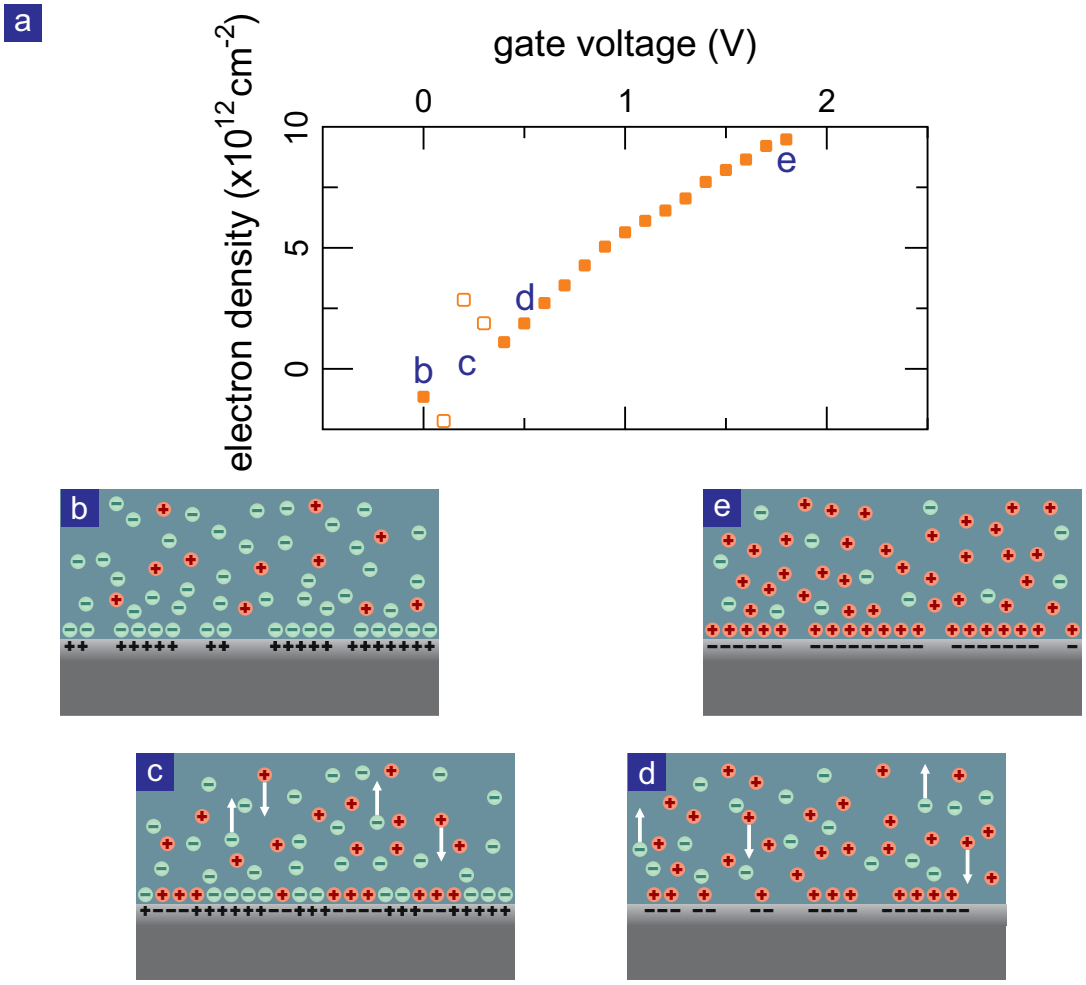

Figure 4.5: Arrangements of ions for different values of gate voltage. (a) Carrier density plotted against gate voltage for a monolayer graphene device. The open dots represent the charge concentration in the electro-hole puddle regime. (b-e) Ionic configuration near the sample surface for values of gate voltage indicated in (a).

voltage, the amplitude of the density inhomogeneity and the dimension of the puddles vary with V_G. When two types of charges coexist the Hall voltage diminishes and may even vanish, because the contributions of electrons and holes sum up [10]. As a consequence, the Hall effect provides an overestimation of the charge carrier concentration when the graphene is in the electron-hole puddle regime. In particular, the estimated charge concentration diverges when moving towards the MCP (see open dots in Figure 4.5-a). The transport is due to only one charge type when the divergence of the evaluated n is suppressed. Therefore, we give a first estimate of the amplitude of the electron-hole puddles by taking the end of the divergent behavior of n as the electron-hole puddle amplitude. Both in mono- and bilayer samples, the puddles are on the order of 10^{12} cm^{-2}. This first, rough estimate tells us that the presence of the electrolyte increases the strength of the electron-hole puddles by one

order of magnitude compared to graphene on silicon dioxide [88, 100–102].

A further increase of gate voltage moves anions away from the sample (as shown in Figure 4.5-d). In this regime the electronic carrier density is rather low, because the packing of cations on the sample surface is partial. At high values of gate voltage, the ionic packing increases (as shown in Figure 4.5-e) and higher values of charge concentration can be achieved in the sample (see Figure 4.5-a). The increase of charge carrier density with gate voltage is almost linear and is described well by the EDL capacitor model [60].

The small deviations from linearity of the dependence of carrier density with gate voltage are likely due to the non-ideality of the electrolyte [56, 60] or possibly also due to errors in the density estimate with the Hall effect [10,97]. The electrolyte model neglects second order effects, as well as thermodynamic currents and partial conductivity of the bulk of the electrolyte [56]. Therefore, the EDL formation energy is not simply described by Equation 2.1. Furthermore, the Hall trace for inhomogeneous materials is not perfectly linear [10] and the average density is determined when $\mu B \gg 1$ [97]. In our calculations, the charge carrier density is determined by the slope of the Hall trace at high magnetic field.

Multilayer graphene shows a linear dependence of carrier density on gate voltage only for low values of V_G (see green symbols in Figure 4.6), because for high applied bias the polymer dissociation could take place [56, 60]. The same effect happens in mono- and bilayer graphene, but it is disguised by the loss of charge at those gate voltages (see Figure 4.8-a).

Analyzing the slope of n vs.V_G for different devices of same and different thickness, we can get the efficiency of the electrolyte for mono-, bi- and multilayer graphene placed on silicon dioxide. Monolayer samples show an average charging of the EDL of $(6.5 \pm 0.5) \times 10^{12}$ cm^{-2}/V, bilayer devices are characterized by a carrier injection of $(10.3 \pm 0.6) \times 10^{12}$ cm^{-2}/V, while the increase rate of charge concentration for multilayer graphene is $(14.2 \pm 0.8) \times 10^{12}$cm^{-2}/V. The efficiency increases with the device thickness, because the screening of the electric field enhances with the number of layers [103].

4.5 Drop of charge concentration at high gate voltage

Figure 4.6 shows the dependence of the induced charge carrier concentration on the applied gate voltage for mono-, bi- and multilayer graphene samples. Mono- and bilayers show a non-monotonic behavior of n with V_G, while multilayers do not exhibit any drop of charge carrier density for high values of bias applied to the electrolyte.

The onset of the decrease occurs at lower gate voltage and carrier density for mono- than bilayer graphene (as shown in Figure 4.6). The value of V_G related to the drop changes from sample to sample, and it is related to the efficiency of the device (quality of the electrolyte and ratio between the areas of channel and gate

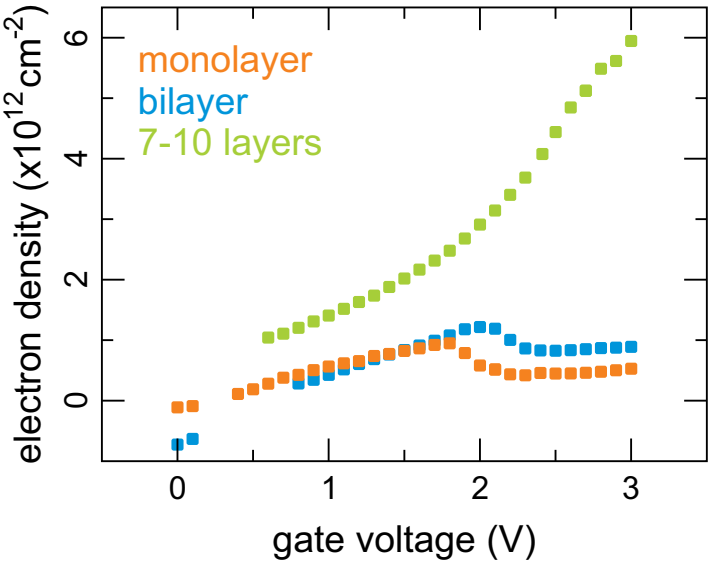

Figure 4.6: Charge accumulation in electrolyte gated samples. The dependence of carrier density on gate voltage is plotted for mono- (orange dots), bi- (azure squares) and multilayer (green symbols) graphene samples.

electrode). In contrast, the values of carrier density are consistent for samples of the same thickness.

Possible explanations are a drop of the strength of the EDL due to electrochemical interactions inside the electrolyte [60], lithiation of the gold electrodes [104] or a loss of the charges to states outside of graphene for instance due to interactions with the substrate [105]. We exclude electrochemical modifications of the electrolyte and lithiation of the Au electrodes, because the drop in the carrier density depends on the sample thickness. Therefore, the process responsible for the carrier density drop has to be related to the differences in the energy spectra of mono- bi- and multilayer graphene. The most plausible reason for the non-monotonic behavior of the charge carrier concentration with gate voltage is filling of charge traps in the SiO_2 substrate [106, 107].

In the next sections, we will introduce charge trap states in insulators (Section 4.5.1) and describe their importance for electrolyte gated graphene devices (Section 4.5.2)

4.5.1 Trap states in silicon dioxide

Silicon dioxide grown on silicon shows different types of defects depending on the growth technique [106–109], the thermal annealing procedure [107, 110] and the presence of dopants [111, 112]. Both the energy and the density of defects vary with the sample preparation technique and the oxide thickness.

The most common defects in silicon dioxide are: oxygen vacancies in $Si \equiv O$

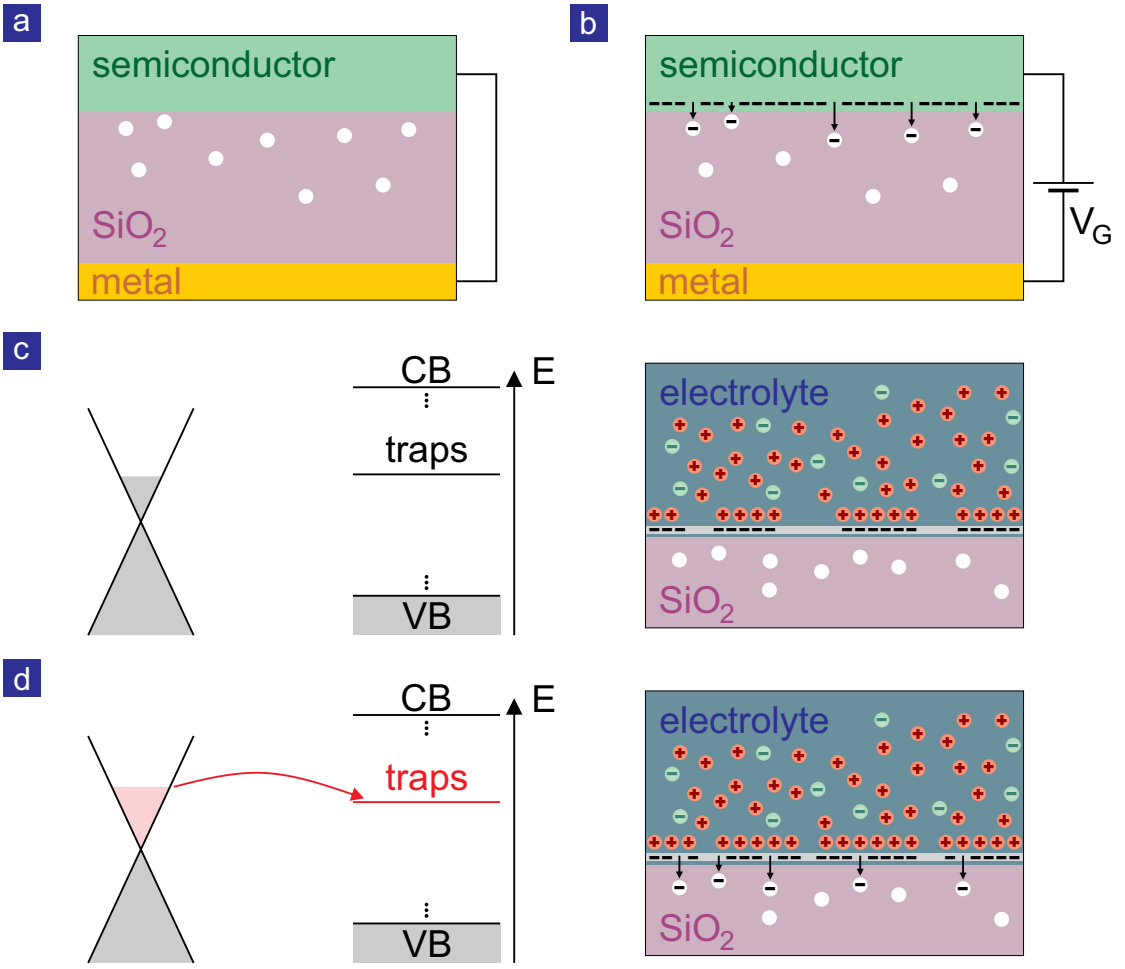

Figure 4.7: Charge trap states in silicon dioxide. Trap states in silicon dioxide in solid gating configuration: with $V_G = 0V$ (a) and with applied gate voltage (b). Explanation of filling the trap states in silicon dioxide in electrolyte gated devices: empty (c) and occupied (d) states in SiO_2.

bonds, holes on missing O in Si-O bonds and Si or O vacancies near dopants [106]. Some of these defects act as trap states, because they can capture electrons or holes [113].

In Figure 4.7-a we illustrate in a cartoon-like fashion the influence of trap states in a conventional field effect transistor. The white dots represent the trap states in the silicon dioxide. When the gate electrode and the semiconductor are kept at the same potential, there is no charge accumulation in the channel and the traps states are empty. When applying a gate voltage charges accumulate into the channel and the chemical potential rises. When the electrons in the channel have enough energy (the gate voltage is sufficiently high) to tunnel into the trap states near the semiconductor-oxide interface [105], an increase of V_G causes the filling of trap states into SiO_2 (as shown in Figure 4.7-b). The carrier density in the channel does not

increase but saturates. A further increase of gate voltage causes the filling of the traps into the bulk of the oxide. If a conductive path of filled traps through the insulator (between semiconductor and metal) is formed, the oxide breaks-down, the field effect mechanism is impeded and charge accumulation into the channel of the transistor is not possible anymore.

The energy and the position of the trap states of different insulating materials have been determined by several techniques, such as electron spin resonance (ESR) [106], high-frequency C-V measurements [109,111], electron paramagnetic resonance (EPR) [108] and electric-field induced second harmonic generation (SHG) [112]. Also electrolyte gated graphene devices may provide some information about such trap states as described below.

4.5.2 Graphene-based spectroscopy of trap states

Because one can control the occupancy of the trap states in the insulator by changing the voltage to the electrolyte, it is possible to extract the energy of the defects in the oxide. A schematic of an electrolyte-gated graphene device is shown in Figure 3.9. Since we want to sense the trap states at the oxide surface, the important area of the device is the interface between the silicon dioxide and the graphene (see right side of Figures 4.7-c and d).

Defect free silicon dioxide is a high energy gap insulator (E_G =8.9 eV [114]). Charge trap states are allowed electronic states (as shown in the left side of Figures 4.7-c and d) within the energy gap when defects are present in the oxide crystal structure [105]. The energy position of the traps with respect to the graphene band structure depends on the band alignment of the graphene monolayer and the oxide interface. The latter has been studied by internal photoemission spectroscopy (IPE). The difference between the graphene charge neutrality point and the silicon oxide conduction band (CB) is about 3.6 eV. The barrier height at the interface between the graphene and the SiO_2 is largely insensitive to the presence of another material covering the graphene [115].

When a positive voltage is applied to the gate electrode, the electron concentration in graphene increases. As a consequence, its Fermi level rises. The energy difference between the CB of silicon dioxide and the Fermi level of the graphene decreases. For low gate voltages, the charge carrier concentration in graphene is low and the Fermi level lies at a lower energy than the trap states in silicon dioxide (as shown in Figure 4.7-c). Therefore, the oxide acts as an insulator and all the charges induced by the electrolyte reside in the graphene. When E_F of graphene reaches the energy of the trap states in the substrate, electrons can tunnel from graphene to the silicon dioxide (see Figure 4.7-d) by the so-called Fowler-Nordheim tunneling [116]. In our experiments, the induced carrier density decreases for higher values of gate voltage (see Figure 4.6), because avalanche tunneling takes place when the energetics allows the traps to get partially filled [116]. The electron tunneling takes place only from graphene to the surface traps of SiO_2 (see Figure 4.7-d).

By knowing the charge carrier concentration in the sample, it is possible to

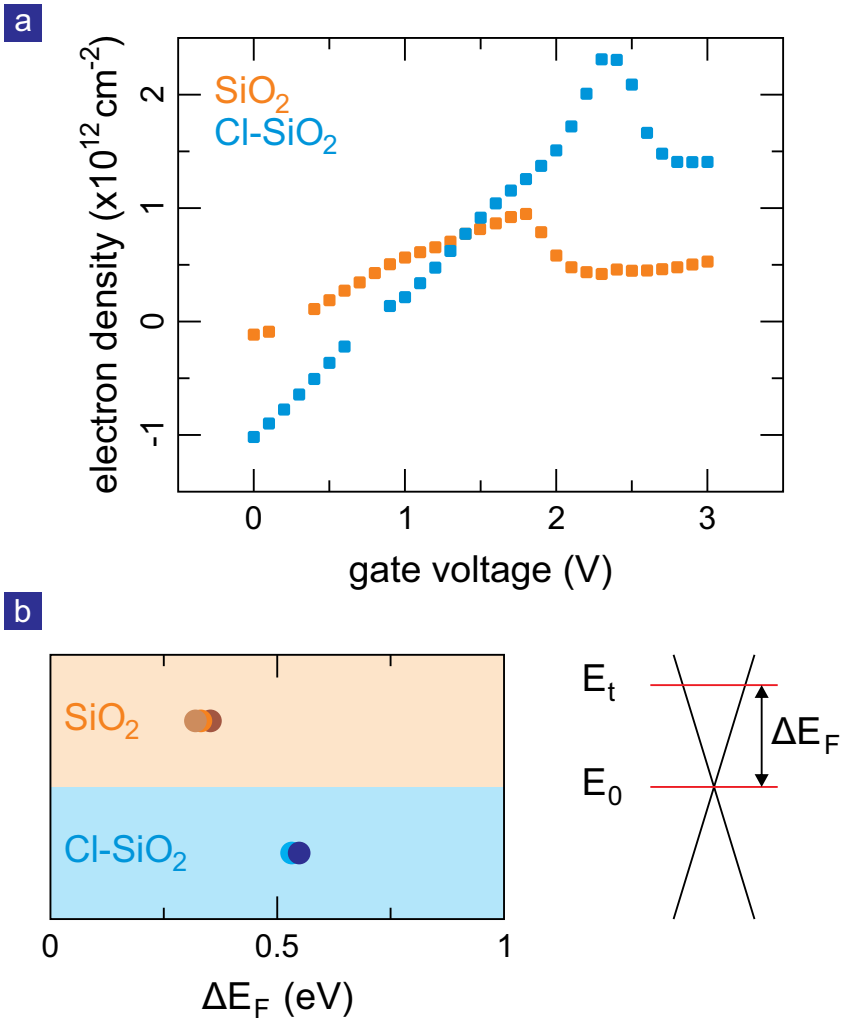

Figure 4.8: Charge trap state spectroscopy of different substrates. (a) Charge carrier concentration vs. gate voltage for monolayer graphene placed on As doped SiO_2 (orange squares) and B doped chlorinated SiO_2 (azure symbols). (b) Increase of the Fermi level of graphene between V_G=0 and the onset of the drop of n for As doped SiO_2 (warm dots) and B doped Cl-SiO_2 (cold symbols).

determine the Fermi energy of graphene and, therefore, its location with respect to the energy level of the trap states in the supporting oxide. The density of states going from mono- to multilayer graphene increases [2]. Therefore, the Fermi energy in multilayer graphene is smaller than in monolayer at the same induced carrier density (see Chapter 1). As a consequence, the filling of traps signaled by a drop in the carrier density appears at higher charge densities in bilayer graphene than in monolayer graphene (see Figure 4.6). Multilayer graphene does not even show any non-monotonic behavior, because it is not possible to induce a high enough carrier density.

We have used electrolyte-gated monolayer graphene devices to determine the

energy distribution of the traps in silicon dioxide. Figure 4.8-a shows the induced carrier density as a function of the gate voltage for monolayer graphene samples placed on different substrates: 300 nm thick dry silicon dioxide thermally grown on arsenic doped silicon (orange symbols), and 300 nm thick dry chlorinated silicon dioxide thermally grown on boron doped silicon (azure squares). The drop in the carrier density appears at higher carrier concentration for graphene placed on chlorinated silicon dioxide than for graphene on conventional silicon dioxide. Figure 4.8-b shows the energies extracted from the onset of the carrier density drop for different devices fabricated on the two substrates. The energy of the traps is calculated as follows. At the charge neutrality point, the Fermi level of graphene lies at $E_0 \approx -3.6$ eV (the conduction band of SiO_2 is set at $E = 0$) [115]. When filling the trap states, the Fermi level of graphene has been raised by a value ΔE_F that can be calculated from the DOS of graphene and the carrier concentration at which the drop in density occurs (see Figure 4.8-b). The values of ΔE_F for samples produced on the same type of substrate match, and the variation between the different substrates is on the order of 180 meV. The energy of the traps can be calculated as $E_t = E_0 + \Delta E_F$. For As doped SiO_2 the energy of the trap states is $E_t \approx -3.24$ eV, while the traps in B doped chlorinated SiO_2 are located at about 3.06 eV below the CB of the silicon dioxide.

In our measurements, the SiO_2 thermally grown on As doped silicon shows traps at lower energy than the chlorinated silicon dioxide grown on B doped silicon (as shown in Figure 4.8-b). This observation is in agreement with reports on trap states in the literature [112, 116, 117]. Boron induced traps lie about 560 meV below the conduction band of SiO_2 [116], they therefore can not be responsible to the loss of charges in our samples. Chlorination of silicon dioxide decreases the density of trap states related to silicon dangling bonds and moves them to higher energies [109]. Therefore, the higher energy measured in chlorinated silicon dioxide is likely attributed to the passivating effect of chlorine.

In conclusion, electrolyte gated monolayer graphene can be used to determine the energy of charge trap states in insulators. The energy range is limited by the efficiency of the electrolyte. The resolution can be controlled and be less than meV.

4.6 Hysteresis in charge concentration

By comparing the behavior of the charge carrier concentration during a sweep up and sweep down of the gate voltage, it is possible to extract more information about the formation of the EDLs, the ionic arrangement on the sample surface and the filling of the trap states at the oxide surface. The dependence of n with increasing and decreasing V_G in monolayer graphene deposited on As doped SiO_2 is shown in Figure 4.9. In the following, we discuss the down sweep.

The charge carrier concentration was determined through Hall measurements. During the down sweep, the charge carrier concentration monotonically drops. Since the time constant of detrapping charges from silicon dioxide is longer than the mea-

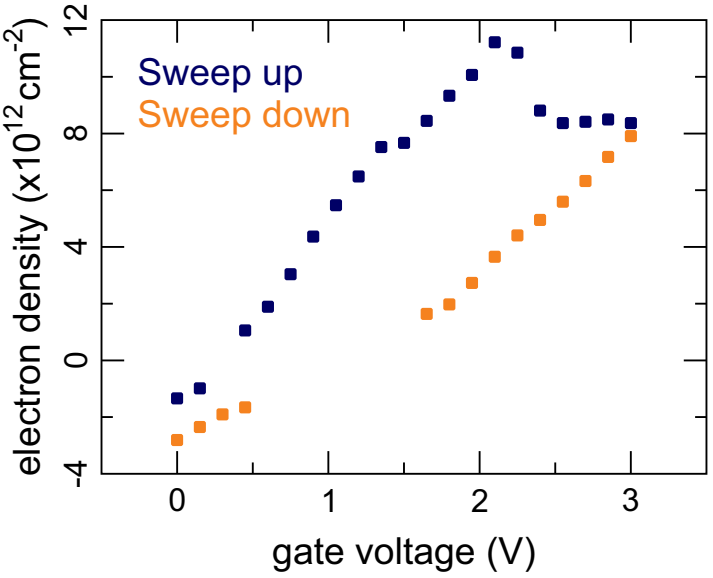

Figure 4.9: Hysteresis of charge concentration in monolayer graphene. Charge carrier density measured in monolayer graphene for increasing (blue squares) and decreasing (orange symbols) gate voltage.

surement duration [106–109], the electrons trapped at the oxide surface keep acting as a source of hole doping in graphene (as in a traditional field effect transistor). As a consequence, the electronic concentration for decreasing gate voltage is lower in comparison with the initial up sweep. We note that at zero gate voltage the carrier concentration remains different and also the amplitude of the electron hole puddles has increased from 1×10^{12} cm^{-2} to approximately 1.6×10^{12} cm^{-2}. Presumably the charge traps enhance the charge disorder near the minimum conductivity point.

In conclusion, despite decreasing the gate voltage the trap states remain filled partially, because the time constant to empty the trap states is much longer than the measurement duration. This causes hysteretic behavior and an increase of the charge inhomogeneity in graphene.

Chapter 5

Charge Inhomogeneity in Electrolyte Gated Graphene

Disorder plays a fundamental role for charge transport [118]. The origin of disorder can be classified in two families: short-range scatters (as atomic defects) and long-range scatters (as charge impurities) [10, 25]. Both types of scattering centers are usually present simultaneously and cause local changes of the carrier density in the conduction band [118]. In monolayer graphene, point vacancies and ripples act as short range scatters [119], while long range scatters are due to residuals of PMMA or adsorbents [99] on the sample surface. These defects induce a spatial inhomogeneity of the charge density and electron-hole puddles form near the charge neutrality point (Dirac point) [2].

A single electronic band system (as monolayer graphene) characterized by a spatially homogeneous charge distribution does not show any magneto-resistance [120]. A system with multiple occupied electronic bands with different carrier mobilities does exhibit a classical magneto-resistance [121]. A large magneto-resistance MR, that does not saturate, was reported in inhomogeneous single band semiconductors, as well as silver chalcogenides [122], doped tellurides [123] and non-magnetic InSb [124]. The observed MR has attracted a lot of interest from theoreticians and a wide range of possible explanations has been proposed [125–128]. The most common interpretation is that the magneto-resistance originates from a spatially inhomogeneous charge distribution across the material [127–130]. Also graphene has been shown to posses a large magneto-resistance near the charge neutrality point [102, 131], and several models have been proposed [102, 119, 120].

We start this chapter by presenting the magneto-resistance data measured in our mono-, bi- and multilayer graphene devices for different values of the gate voltage (Paragraph 5.1). Paragraph 5.2 gives an overview of the theories describing a strong magneto-resistance in non-magnetic materials with particular attention to the models used to fit our experimental data: a self consistent effective medium approximation (Section 5.2.1) and a model assuming quadratic behavior of the MR with magnetic field (Section 5.2.2). Paragraph 5.3 contains the fits of our data with the two theoretical models. Finally we compare the fitting parameters obtained from the two models (Section 5.4).

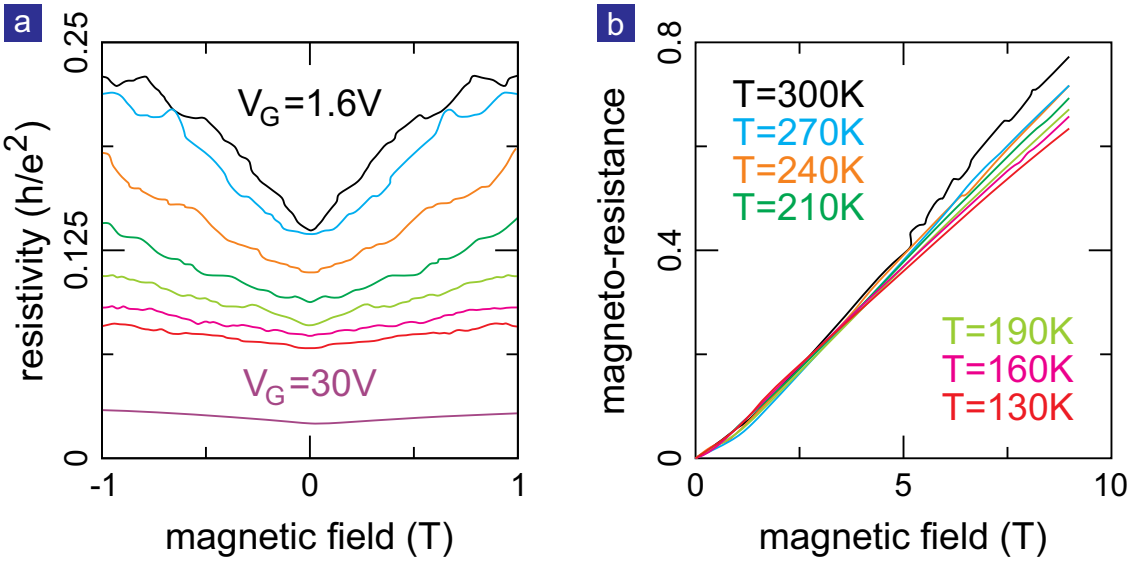

Figure 5.1: Magneto-resistance in graphene based devices. The dependence of transverse MR on the applied perpendicular magnetic field for (a) monolayer graphene near CNP (adapted from [102]) and (b) multilayer CVD grown graphene (adapted from [131]).

5.1 Magnetoresistance measurements in graphene based devices

The magneto-transport properties of monolayer graphene near the charge neutrality point have been intensively studied in view of the unconventional linear band structure [100,102,119,120,132]. The magneto-resistance is the normalized variation of resistance of the sample due to the application of a magnetic field. Mathematically it is defined as follows:

$$MR = \frac{R(B) - R(B=0)}{R(B=0)}. \tag{5.1}$$

The magnetic field can be applied perpendicular to the current direction (transverse magneto-resistance) or in the plane where the current flows (longitudinal magneto-resistance). Monolayer graphene near the CNP was shown to posses a large transverse magneto-resistance at temperatures ranging from 1.6 K to 300 K [102, 120]. At 1.6 K, the MR is strong near the charge neutrality point and vanishes when the chemical potential is tens of meV (see Figure 5.1-a). At the CNP local potential fluctuations create electron-hole puddles [132]. A conductor with electrons and holes can exhibit large magneto-resistance [121]. Also in epitaxially grown graphite (~ 50 layers) on silicon carbide [131] a linear magneto-resistance has been observed. This MR persists up to room temperature (see Figure 5.1-b). Its slope increases with rising temperature. This was attributed to the inhomogeneity of the samples, as

a result of the grain boundaries. Grains ($\sim$ 1.5 μm) are much smaller than the device dimensions. In both cases, strength and spatial distribution of the inhomogeneity originate from the sample preparation process [102, 120, 131]. They can not be altered in-situ.

To the best of our knowledge, no detailed studies of the magneto-resistance in electrolyte gated graphene devices have been performed. During Hall measurements carried out at room temperature in electrolyte gated graphene devices (see Chapter 4), we also recorded the longitudinal resistance of the samples (transverse MR) with the applied perpendicular magnetic field for all the values of gate voltage. Figure 5.2-a shows such data obtained on monolayer graphene at gate voltages ranging from 0 to 3 V. The MR is symmetric around $B = 0$, and hence we conclude that there are no significant contributions from the Hall resistance that would break this symmetry [10]. The behavior of the magneto-resistance strongly depends on the applied gate voltage. In particular, for low values of V_G the longitudinal resistance of the sample at 10 T is several times larger than in the absence of a magnetic field. In the high gate voltage regime, however the MR is much lower. In both cases, the magneto-resistance appears to have a roughly quadratic dependence on B in the low field regime, and becomes approximately linear (with sublinearity for low gate voltages) for high magnetic fields. The value of the magnetic field at which the MR crosses over from a quadratic to a linear dependence on B changes with the applied gate voltage, and the general trend is that this threshold field increases with gate voltage (see Figure 5.2-a).

We also performed measurements on bilayer graphene. Figure 5.2-b shows the magneto-resistance of a bilayer graphene sample for different gate voltage values. As for monolayer graphene, the magneto-resistance has an approximately quadratic behavior at low magnetic field and a linear dependence on B at high fields. Furthermore, the transition between the two behaviors moves to higher magnetic fields with increasing values of the gate voltage.

Mono- and bilayer graphene show an increase of the MR in the vicinity of the MCP and the drop of density at high gate voltage due to trap surface states. Since they show the charge neutrality point near $V_G = 0$ and do not exhibit any non-monotonic behavior of n with gate voltage, it is interesting to study also the behavior of the MR in multilayer graphene samples. The magneto-resistance of multilayer graphene for different values of gate voltage is illustrated in Figure 5.3. The MR drops monotonically with increasing gate voltage. The decrease is faster for low carrier densities. At low magnetic field the MR exhibits a quadratic dependence on the magnetic field irrespective of the value of V_G. For high fields, the magneto-resistance is linear near the minimum conductivity point, while it has a sub-linear dependence on B at high gate voltages.

In conclusion, the magneto-resistance is quadratic for low and linear (or sublinear) for high magnetic field, and it seems to decrease with increasing gate voltage for mono-, bi- and multilayers. On top of this general behavior, local enhancements of the MR are observed near the MCP and where charges are lost to the trap states in through the substrate. Below we analyze possible reasons for this behavior of the MR with applied gate voltage.

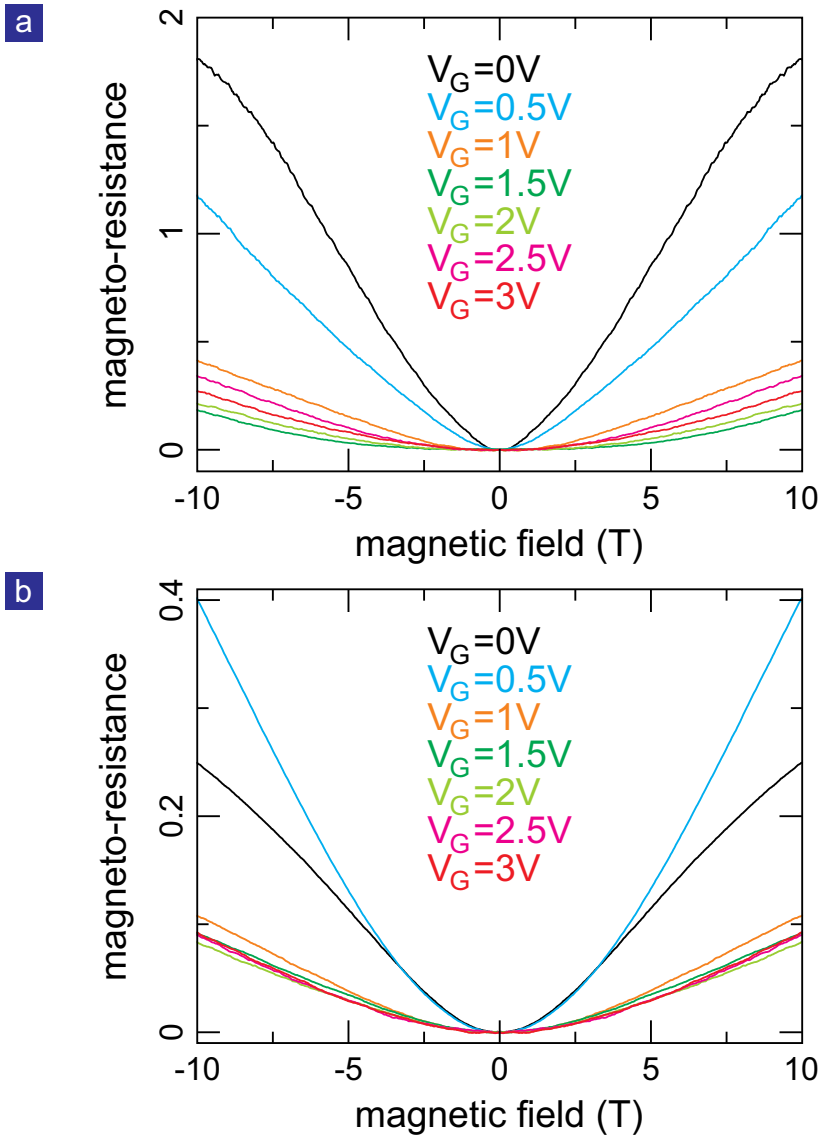

Figure 5.2: Magneto-resistance of electrolyte gated graphene. The dependence of the transverse MR of (a) mono- and (b) bilayer graphene devices on applied magnetic field is shown for different values of the gate voltage.

5.2 Theoretical models for high magneto-resistance

The experimental discovery of high magneto-resistance in charge inhomogeneous non-magnetic materials [122–124] has attracted strong theoretical interest. A large variety of different explanations has been proposed. The theories can essentially be classified in three categories: macroscopic models [125, 126], microscopic quantum explanations [127] and microscopic semiclassical theories based on different effective medium approximations (EMAs) [102, 120, 128–130, 133–138]. A more detailed de-

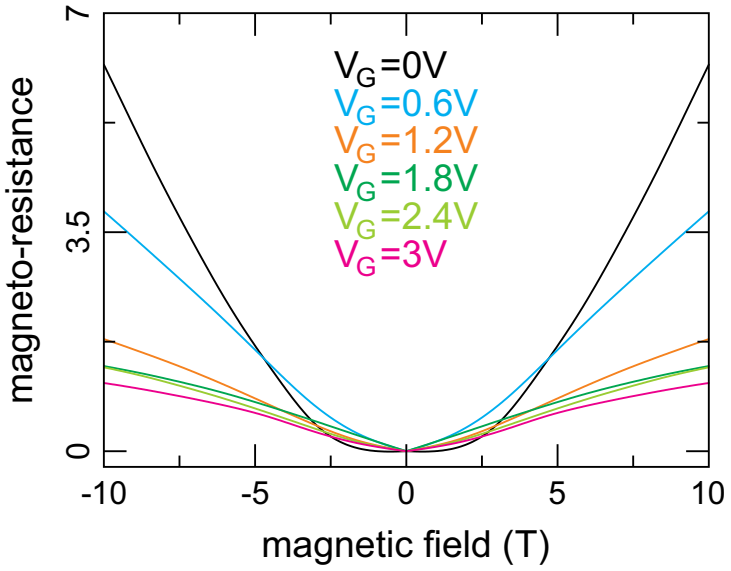

Figure 5.3: Magneto-resistance of an electrolyte gated multilayer graphene. The dependence of transverse MR on the applied magnetic field is shown for different values of the gate voltage.

scription of the different categories (with a special focus on the theories used to fit our experimental data) follows.

Macroscopic models describe the problem with a resistor network [125, 126]. These theories focus on the high magnetic field regime and were developed to account for the linear behavior of the MR in silver chalcogenides [122]. The numerical solution of resistor network models gives a different behavior for networks composed of an odd or even number of resistors [126]. Extrapolating the physical properties of the studied systems within these models is challenging [120], because single resistors can not be associated with any characteristic of the material. Therefore, we decided to exclude such theories to fit our experimental data.

A microscopic model for large and linear magneto-resistance in inhomogeneous semiconductors was proposed [127]. This model is based on the idea that gapless semiconductors in case of disorder very often have a very low effective mass. Therefore, they can be treated as materials with a linear band dispersion. A second assumption is that the average carrier density is very low and only a Landau level is occupied. This hypothesis is not valid in our samples (since we measure high magneto-resistance at densities up to 10^{13} cm^{-2}), so this theory can not explain our experimental findings.

The third approach is the use of an effective medium approximation to describe the behavior of charge transport in a conductor exposed to a perpendicular magnetic field. The EMA approach has been widely used for materials where the physical properties have a complicated distribution and an exact analytical description of their average values can not be derived. The sample is partitioned in areas char-

acterized by different values of physical properties and their average macroscopic values are calculated [133]. These kinds of approximations have been widely used to address the high magneto-resistance in charge inhomogeneous conductors, because in these systems percolation effects between areas of different densities are unimportant [139]. Early works were based on composite materials characterized by scalar conductivities [118, 133]. More recent theories have treated materials with non-scalar conductivity tensors in order to better capture the magneto-transport features both in the Hall trace and the longitudinal resistance [128–130, 134–138].

EMA theories whose assume that the 2D carbon layer is broken up into electron and hole puddles occupying different fractional areas and that is homogeneous within each puddle, have been developed [128,130,138] to explain recent experimental works showing high magneto-resistance in single band conductors [102, 122, 124]. These theories however only produce a non zero magneto-resistance when multiple bands are occupied (transport electron- and hole-like) [120].

To our knowledge, only two theories are able to properly describe high magneto-resistance in non-magnetic materials when the average carrier density is higher than the charge fluctuations, i. e. with only one charge carrier type [120,129]. One model relies on a self-consistent effective medium approximation and does not assume any asymptotic behavior of the MR with magnetic field [129]. The second theory assumes quadratic behavior of the resistance with increasing magnetic field [120]. In the next sections, we introduce these two models whose will be used to fit our experimental transport data.

5.2.1 SEMA MODEL

The SEMA model is a self-consistent effective medium approximation (SEMA). It allows obtaining information about the microscopic properties of the sample [129]. It does not assume a specific asymptotic behavior (linear or quadratic), but as a result it contains a large number of fitting parameters [129]. A detailed explanation of this SEMA theory follows.

The 2D electrical conductivity problem is transformed in an another equivalent, isomorphic and solvable conductivity problem that is easier to deal with. We consider a 2D medium with a spatially varying resistivity tensor:

$$\hat{\rho}(\mathbf{r}) = \rho_0 \hat{\xi}(\mathbf{r}). \tag{5.2}$$

Here, ρ_0 is the scalar resistivity and $\hat{\xi}(\mathbf{r})$ is a dimensionless 2×2 tensor. Locally, the resistivity can be described by the relation:

$$\mathbf{E}(\mathbf{r}) = \hat{\rho}(\mathbf{r})\mathbf{J}(\mathbf{r}) \tag{5.3}$$

where $\mathbf{E}(\mathbf{r})$ is the electric field and $\mathbf{J}(\mathbf{r})$ is the current density. A rotation of 90° gives a solvable problem defined by:

$$\mathbf{E}'(\mathbf{r}) = a\mathbf{E}(\mathbf{r}) + b\hat{R}\rho_0\mathbf{J}(\mathbf{r}) \tag{5.4}$$

and

$$\mathbf{J}'(\mathbf{r}) = c\mathbf{J}(\mathbf{r}) + d\hat{R}\rho_0^{-1}\mathbf{E}(\mathbf{r}) \tag{5.5}$$

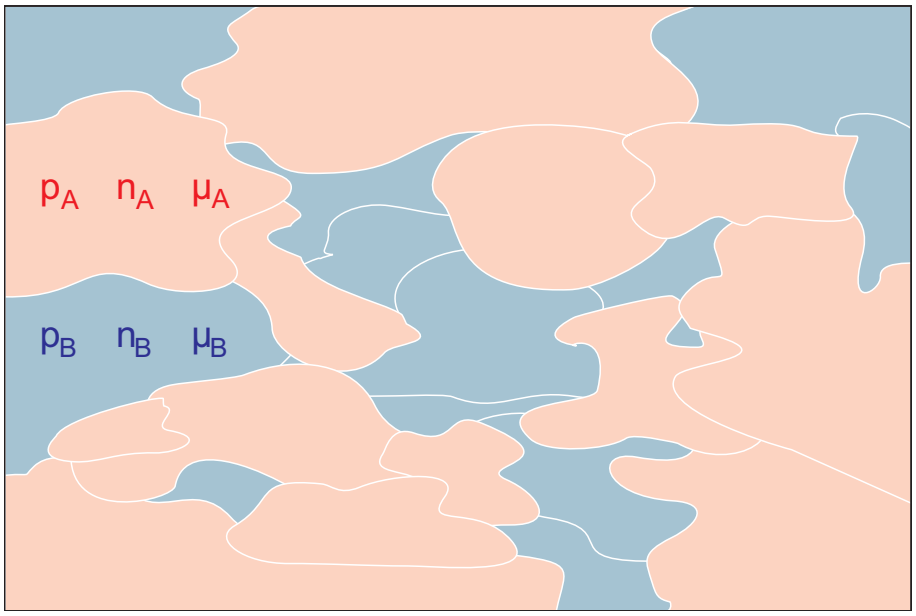

Figure 5.4: Schematic representation of the SEMA device. The sample is partitioned in areas A (B) characterized by areal fraction p_A (p_B), density n_A (n_B) and mobility μ_A (μ_B).

where a, b, c and d are constants, $\hat{R}$ is the rotation tensor, $\mathbf{E}'(\mathbf{r})$ is the electric field of the new problem and $\mathbf{J}'(\mathbf{r})$ is the new current density. Obviously, the relation between electric field and current density of the new problem is $\mathbf{E}'(\mathbf{r}) = \hat{\rho}'(\mathbf{r})\mathbf{J}'(\mathbf{r})$, where a, b, c and d are chosen to ensure that the new local resistivity tensor is symmetric. It takes on the following form:

$$\hat{\rho}'(\mathbf{r}) = \rho_0\hat{\xi}'(\mathbf{r}) = \rho_0[a\hat{\xi}(\mathbf{r}) + b\hat{R}][c\hat{I} + d\hat{R}\hat{\xi}(\mathbf{r})]^{-1} \tag{5.6}$$

with $\hat{I}$ being the unit tensor.

The effective resistivity of the 2D composite materials is defined as the areal average of the resistivity across the different regions and the previous equations can still be used when substituting the local quantities with the average ones:

$$\hat{\xi}'_e = (a\hat{\xi}_e + b\hat{R})(c\hat{I} + d\hat{R}\hat{\xi}_e)^{-1}. \tag{5.7}$$

In this case, the composite material is made of 2 types of regions characterized by different carrier densities (n_A and n_B) and mobilities (μ_A and μ_B), as shown in a cartoon-like fashion in Figure 5.4. Regions of type A (B) occupy a fractional area p_A (p_B) with $p_A + p_B = 1$. A perpendicular magnetic field breaks the symmetry of the resistivity tensor of each area: α_i and β_i are the ohmic and Hall resistivities of area i (with $i = A, B$). Mobility and ohmic resistivity of each region are assumed to be magnetic field independent. The Hall resistivities of region A and B are assumed to be different, because the two areas are characterized by different carrier densities.

The ohmic and Hall resistivities are given by:

$$\begin{aligned} \alpha_i &= e\mu_i n_i \qquad i = A, B, \\ \beta_i &= \alpha_i \mu_i H \qquad i = A, B, \end{aligned} \tag{5.8}$$

where e is the electronic charge and H is the magnetic field.

The imposed symmetry on $\hat{\rho}'(\mathbf{r})$ requires the following choice of the constants a, b, c and d in Equation 5.6:

$$\begin{aligned} a &= d = 1 \\ b &= \frac{\Delta_B - \Delta_A \pm \sqrt{(\Delta_B - \Delta_A)^2 + 4(\beta_B - \beta_A)(\beta_B \Delta_A - \beta_A \Delta_B)}}{2(\beta_B - \beta_A)} \\ c &= \frac{\Delta_A - \Delta_B \pm \sqrt{(\Delta_B - \Delta_A)^2 + 4(\beta_B - \beta_A)(\beta_B \Delta_A - \beta_A \Delta_B)}}{2(\beta_B - \beta_A)}. \end{aligned} \tag{5.9}$$

Here, $\Delta_i = \alpha_i^2 + \beta_i^2$ (with $i = A, B$). The square root is added when $\beta_A < \beta_B$, while it is subtracted in the opposite case. The resistivity of the transformed problem is:

$$\hat{\xi}'(\mathbf{r}) = \xi'_A \hat{I} \theta_A(\mathbf{r}) + \xi'_B \hat{I} \theta_B(\mathbf{r}) \tag{5.10}$$

where

$$\xi'_i = \frac{\alpha_i}{c + \beta_i} \qquad i = A, B \tag{5.11}$$

and

$$\theta_i(\mathbf{r}) = \begin{cases} 1 & \text{if } \mathbf{r} \in \text{area occupied by component } i = A, B \\ 0 & \text{otherwise.} \end{cases} \tag{5.12}$$

Now, we can relate the effective resistivity of the initial problem with the effective ohmic resistivity of the transformed system:

$$\begin{aligned} \alpha_e &= \frac{b + c}{1 + \alpha_e'^2} \alpha'_e \\ \beta_e &= \frac{b - c\alpha_e'^2}{1 + \alpha_e'^2}. \end{aligned} \tag{5.13}$$

Finally, to derive the effective resistivity of the transformed problem we consider $p_A \neq p_B$ and we use the self-consistent medium approximation (SEMA). A SEMA requires the presence of inclusions in an uniform and counterfeit host sample. The change in the areal averaged current density caused by an inclusion is required to vanish when averaged over a length as long as several inclusions. This approximation yields a quadratic equation, whose solution is the effective resistivity of the transformed system:

$$\alpha'_e = (\frac{1}{2} - p_A)(\xi'_B - \xi'_A) + \sqrt{(\frac{1}{2} - p_A)^2 (\xi'_B - \xi'_A)^2 \xi'_A \xi'_B}. \tag{5.14}$$

By substituting equation (5.14) to (5.13) the resistivity of the initial problem is found. This solution gives an approximate result for the magnetic field dependence of

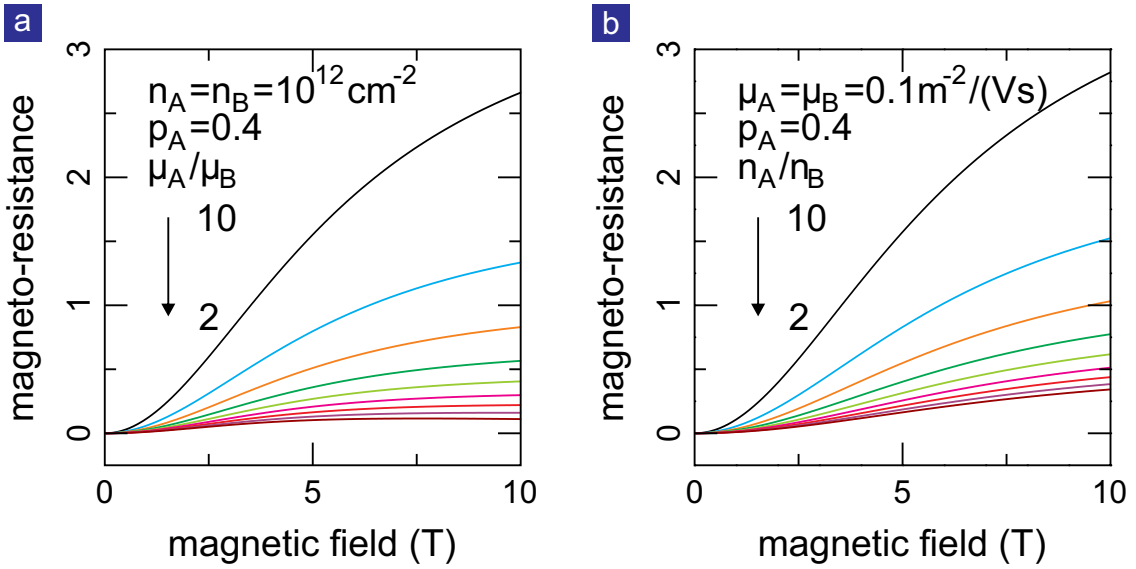

Figure 5.5: Magneto-resistance calculated with the SEMA model. Dependence of MR on magnetic field calculated with the SEMA model for: (a) $n_A = n_B = 1 \times 10^{12} cm^{-2}$ and $10 \leq \mu_A/\mu_B \leq 2$, and (b) $\mu_A = \mu_B = 1000 cm^2/(V \cdot s)$ and $10 \leq n_A/n_B \leq 2$.

the conductivity of an inhomogeneous medium characterized by two sets of mobilities (μ_A and μ_B), densities (n_A and n_B) and areal fractions (p_A and p_B). In the high magnetic field regime the longitudinal resistivity saturates, and the further the areal fractions are from being equal, the earlier the saturation takes place. Furthermore, when $p_A \gg p_B$ the effective longitudinal resistivity mostly depends on the electrical properties of portion A and the MR value is small.

Figure 5.5 shows the magneto-resistance resulting from this SEMA model. Since this model has five free parameters (p_A and p_B are related by $p_A + p_B = 1$), we fix three of the parameters and calculate the dependence of the MR on the remaining two. In particular, we set $p_A = 0.4$ and $n_A = n_B = 1 \times 10^{12} cm^{-2}$ varying the ratio μ_A/μ_B form 10 to 2 (as shown in Figure 5.5-a). The magneto-resistance decreases with decreasing mobility ratio. For the lowest values of μ_A/μ_B, the MR is non-monotonic. Figure 5.5-b depicts the MR in the case of $p_A = 0.4$, $\mu_A = \mu_B = 1000 cm^2/(V \cdot s)$ and $10 \leq n_A/n_B \leq 2$. In this case, the magneto-resistance approaches zero when the ratio n_A/n_B drops, but it is always monotonic.

In conclusion, when the conductivities of the constituents become similar the longitudinal magneto-resistance vanishes (see Figure 5.5). This is in agreement with the model for homogeneous conductors in a perpendicular magnetic field [10, 129]. Furthermore, this approach gives the best results in the high magnetic field regime and can be used to fit experimental data up to 10-15 T [129].

5.2.2 Quadratic approach

The starting point of this theoretical approach is to assume a quadratic magnetoresistance for sufficient low magnetic fields [120]. This assumption is supported by several experimental works on different materials [102, 120, 122, 123]. The quadratic equation describing the dependence of resistivity on the applied perpendicular magnetic field looks as follows:

$$\rho_{xx}(B) = \rho_{xx}(B=0)[1 + A(\mu B)^2], \tag{5.15}$$

where A is a dimensionless parameter used to fit the data and μ is the charge carrier mobility. The aim of the model is to determine the value of A depending on the charge disorder of the sample.

The carrier density is assumed to have a Gaussian distribution around an average carrier density n_0 with fluctuations given by n_{rms}. The Gaussian distribution has been theoretically justified for monolayer graphene [132] and experimentally determined using the scanning single-electron transistor technique [100].

The parameter A is calculated by means an effective medium approximation that considers a continuous Gaussian distribution of the carrier density [120]. The EMA is derived considering a single homogeneous region (of conductivity σ) incorporated in a uniform medium of conductivity σ^{EMA}. The spatially integrated inhomogeneities of the electric field are assumed to be zero [119]. Therefore, for a $2D$ systems we get the following space integral:

$$\int d^2r \, \frac{\sigma(\mathbf{r}) - \sigma^{EMA}}{\sigma(\mathbf{r}) + \sigma^{EMA}}. \tag{5.16}$$

The effective medium conductivity can be calculated averaging the Gaussian disorder distribution $P[n, n_0, n_{rms}]$ [119] and using a quadratic depolarization tensor valid for 2D conductors [134]. The following set of coupled integral equations allows calculating the EMA conductivity and, therefore, the parameter A:

$$\begin{aligned} &\int dn \; P[n, n_0, n_{EMA}] \; \frac{\sigma_{xx}^2[n] - (\sigma_{xx}^{EMA})^2 + (\sigma_{xy}^{EMA} - \sigma_{xy}[n])^2}{(\sigma_{xx}^{EMA} + \sigma_{xx}[n])^2 + (\sigma_{xy}^{EMA} - \sigma_{xy}[n])^2} = 0 \\ &\int dn \; P[n, n_0, n_{EMA}] \; \frac{\sigma_{xy}[n]) - \sigma_{xy}^{EMA}}{(\sigma_{xx}^{EMA} + \sigma_{xx}[n])^2 + (\sigma_{xy}^{EMA} - \sigma_{xy}[n])^2} = 0. \end{aligned} \tag{5.17}$$

Here, the conductivities $\sigma_{xx}[n]$ and $\sigma_{xy}[n]$ are derived from a homogeneous density model [119]. From Equations 5.17, it follows that the effective medium transverse conductivity $\sigma_{xy}[n]$ is zero when either $B = 0$ or $n_0 = 0$, as already calculated with other EMA theories [119, 132]. The theoretical model can be solved for any 2D material, charge inhomogeneity distribution and scattering potential under the above adopted assumption [120].

If the mobility is independent of the density, Equations 5.17 are simplified considerably and for a Gaussian charge distribution take on the following form:

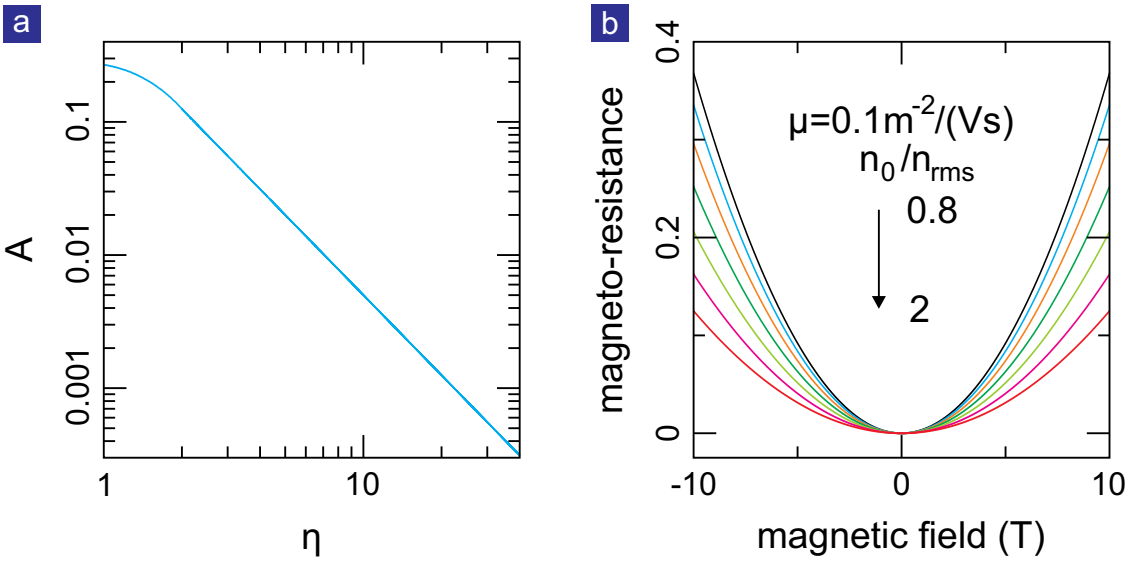

Figure 5.6: Theoretical curves calculated with the quadratic EMA. (a) Dependence of the dimensionless fitting parameter A on $\eta = n_0/n_{rms}$. (b) Magneto-resistance vs. magnetic field for $\mu = 0.1m^2/(V \cdot s)$ and $2 \leq n_0/n_{rms} \leq 0.8$.

$$\begin{aligned} \int_{-\infty}^{\infty} dy\, e^{-(y-\eta)^2/2}\, \frac{y^2 - y_1^2 + \tilde{b}^2(y_2 - y)^2}{(|y|+y_1)^2 + \tilde{b}^2(y_2 - y)^2} &= 0 \\ \int_{-\infty}^{\infty} dy\, e^{-(y-\eta)^2/2}\, \frac{y_2 - y}{(|y|+y_1)^2 + \tilde{b}^2(y_2 - y)^2} &= 0, \end{aligned} \tag{5.18}$$

where $\eta = n_0/n_{rms}$ is the ratio between the average charge density and the Gaussian charge density fluctuations, $\tilde{b} = \mu B$ is the dimensionless magnetic field, and $y_1[\eta, \tilde{b}]$ and $y_2[\eta, \tilde{b}]$ are dimensionless parameters. Finally, the coefficient describing the strength of the quadratic dependence of the magneto-resistance takes on the form:

$$A[\eta] = 1 - \left[\left(\frac{y_2[\eta, 0]}{y_1[\eta, 0]} \right)^2 + \frac{1}{2\mu^2} \frac{\partial_B^2 y_1[\eta, 0]}{y_1[\eta, 0]} \right]. \tag{5.19}$$

The mobility can be calculated with the semiclassical Boltzmann theory [132] starting from experimental data. It is important to notice that the solutions for density dependent and density independent μ have been shown to be very similar [120]. Therefore, we analyze the results obtained with the simpler model assuming that the mobility is independent of the density.

Figure 5.6-a shows the dependence of the magneto-resistance coefficient A on the ratio between the average carrier density n_0 and the amplitude of the carrier density fluctuations n_{rms}. In the other models using a similar EMA, MR vanishes rapidly when $n_0 > n_{rms}$ [120]. It is important to notice that this model is able

to describe the magneto-resistance when the average carrier density is higher than the density fluctuations and can be used to describe the transport properties of every inhomogeneous two-dimensional electronic system. In the high η region, the coefficient A follows a power law $A \sim (n_0/n_{rms})^{-2}$. Substituting the solution of Equation 5.19 in Equation 5.15, the quadratic magneto-resistance can be calculated. For a fixed mobility, the magneto-resistance decreases with decreasing η. In other words, the MR is suppressed in systems with improved homogeneity (see Figure 5.6-b).

In conclusion, this theoretical model is capable of describing the quadratic behavior of the MR in charge inhomogeneous systems characterized by an average carrier density n_0 higher than the superposed charge fluctuations n_{rms}. Therefore, we can use this model to fit our experimental MR data of mono-. bi- and multilayer graphene in the low magnetic field region [120].

5.3 Determination of the charge inhomogeneity

In this section, we discuss the results of fitting of the experimentally measured magneto-resistance using the SEMA model (Section 5.3.1) and the quadratic MR model (Section 5.3.2). The fitting parameters of both models give information about the degree of charge inhomogeneity in electrolyte-gated samples with different layer thickness.

5.3.1 Fit with the SEMA theory

Figure 5.7-a shows the experimental MR together with fists using the SEMA model for four values of the gate voltage in a monolayer graphene sample. The self-consistent effective medium approximation describes very well the functional dependence on B of our experimental data, but to verify the validity of the model we have also to analyze the behavior of the fitting parameters.

For gate voltages lower than 1.5 V, the carrier density of regions A and B increases (see Figure 5.7-b). It is interesting to notice that for $V_G = 0.2$ V the charge carriers in regions A are holes, while in regions B they are electrons. As a consequence, the SEMA model agrees with the Hall measurements (see Figure 4.1) confirming that electron-hole puddles are present near the CNP of monolayer graphene. The mobility of the two regions increases as we approach the minimum conductivity point, and μ_A is always lower than μ_B (at the same time $n_A > n_B$). The fractional area of region A decreases with increasing density (see the inset of Figure 5.7-c). Since one of the regions is growing and the difference in the density of the two areas stays constant for increasing average density, the model indicates increasing charge order in electrolyte gated monolayer graphene for $V_G < 1.8$ V.

The non-monotonic behavior of n *vs* V_G at higher voltages is accompanied by a drop in the density of both regions. At the same time, the mobilities of areas A and B become with gate voltage (see Figure 5.7-c). In any case, the values of the

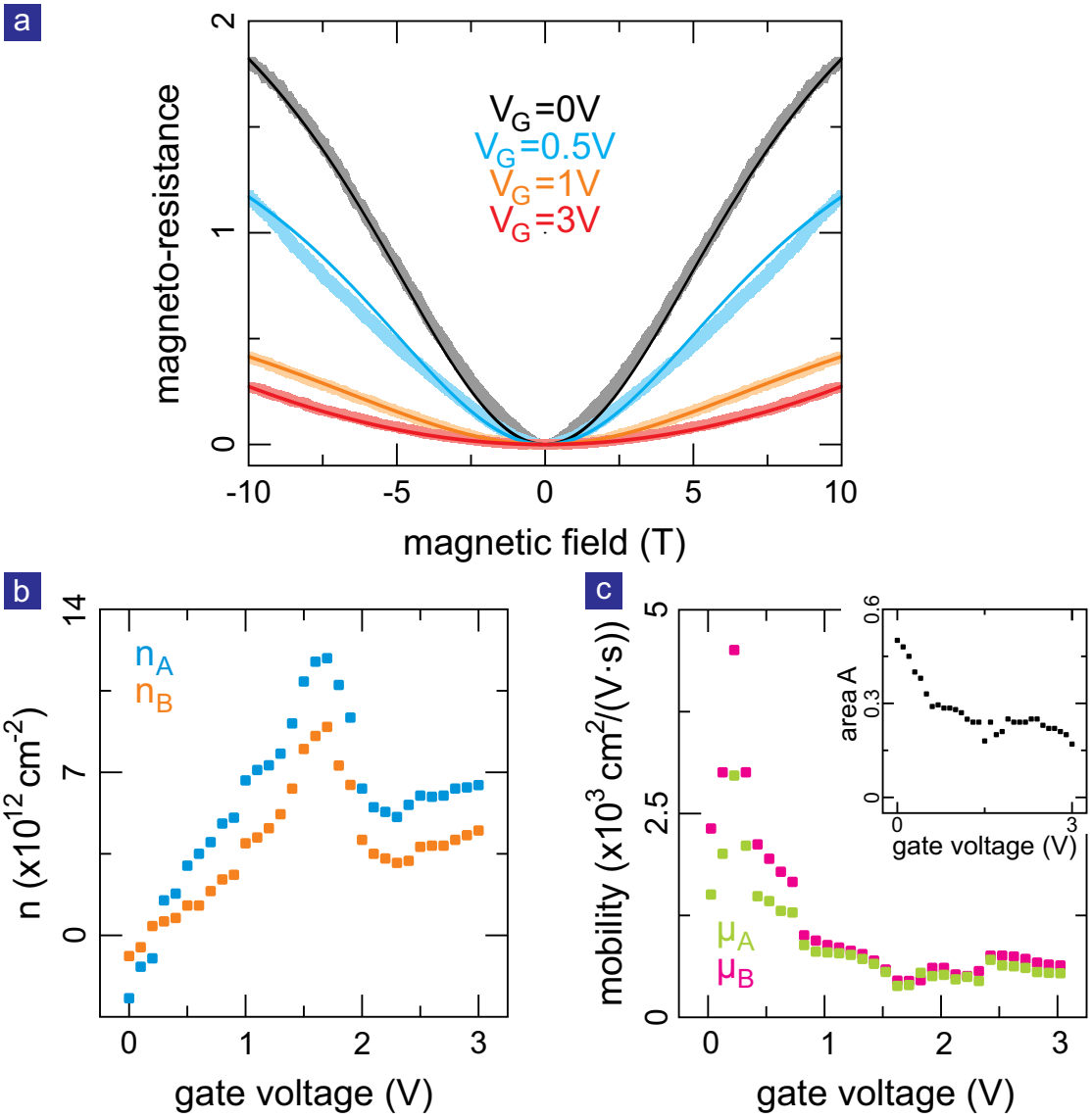

Figure 5.7: Monolayer graphene: fitting of MR with the SEMA model. (a) Dependence of experimental (thick lines) and fitted (thin lines) magneto-resistance on magnetic field for different values of gate voltage. Fitting parameters: (b) densities of area A (n_A) and B (n_B), (c) mobilities μ_A and μ_B of the two areas (Inset: spatial fraction of area A).

mobilities for a specific carrier density before and after filling the trap states are different. In particular, the mobility for $V_G = 3$ V is lower than for $V_G = 1.8$ V (the carrier concentration is the same). This indicates increasing disorder driven by filling the trap states at the surface of the insulating substrates.

For higher values of gate voltage, the trap states are completely full (as described in Section 4.5) and the densities of the two regions increases again (with a constant difference between areas A and B). At the same time, the fractional area

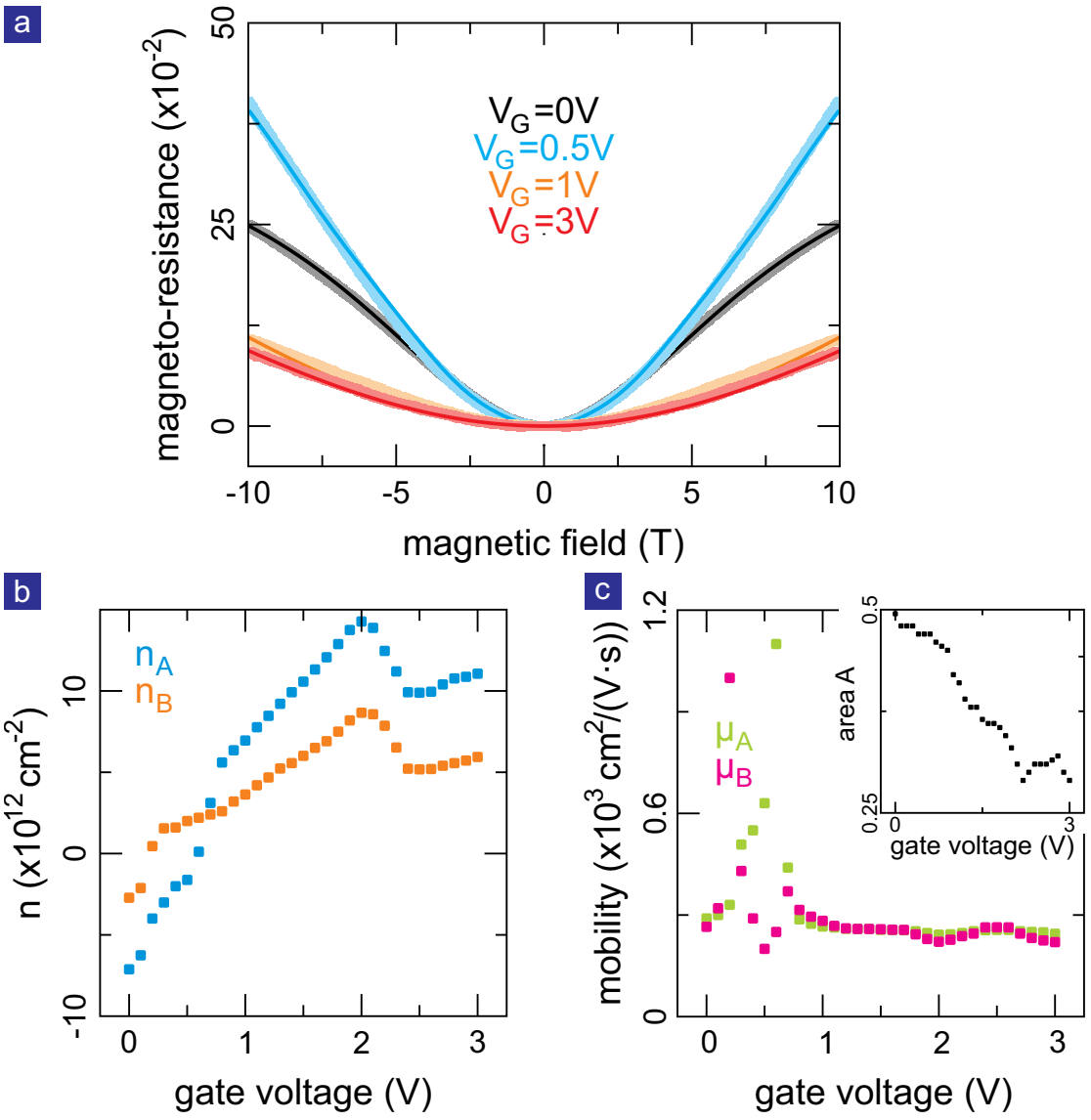

Figure 5.8: Bilayer graphene: fitting of MR with the SEMA model. (a) Dependence of the experimental (squares) and fitted (lines) magneto-resistance on magnetic field for different values of gate voltage. Fitting parameters: (b) densities of area A (n_A) and B (n_B), (c) mobilities μ_A and μ_B of the two areas (Inset: spatial fraction of area A).

B increases again. Therefore, the system seems to move to a more ordered charge carrier configuration.

The analysis of the magneto-resistance of electrolyte gated bilayer graphene gives similar results as for monolayers (see Figure 5.8). The initial hole doping at $V_G = 0$ is confirmed in the extracted densities of regions A and B. Electron and hole puddles coexist up to gate voltage of approximately 0.6 V (as indicated by the Hall measurements shown in section 4.4). The mobility of area A increases when

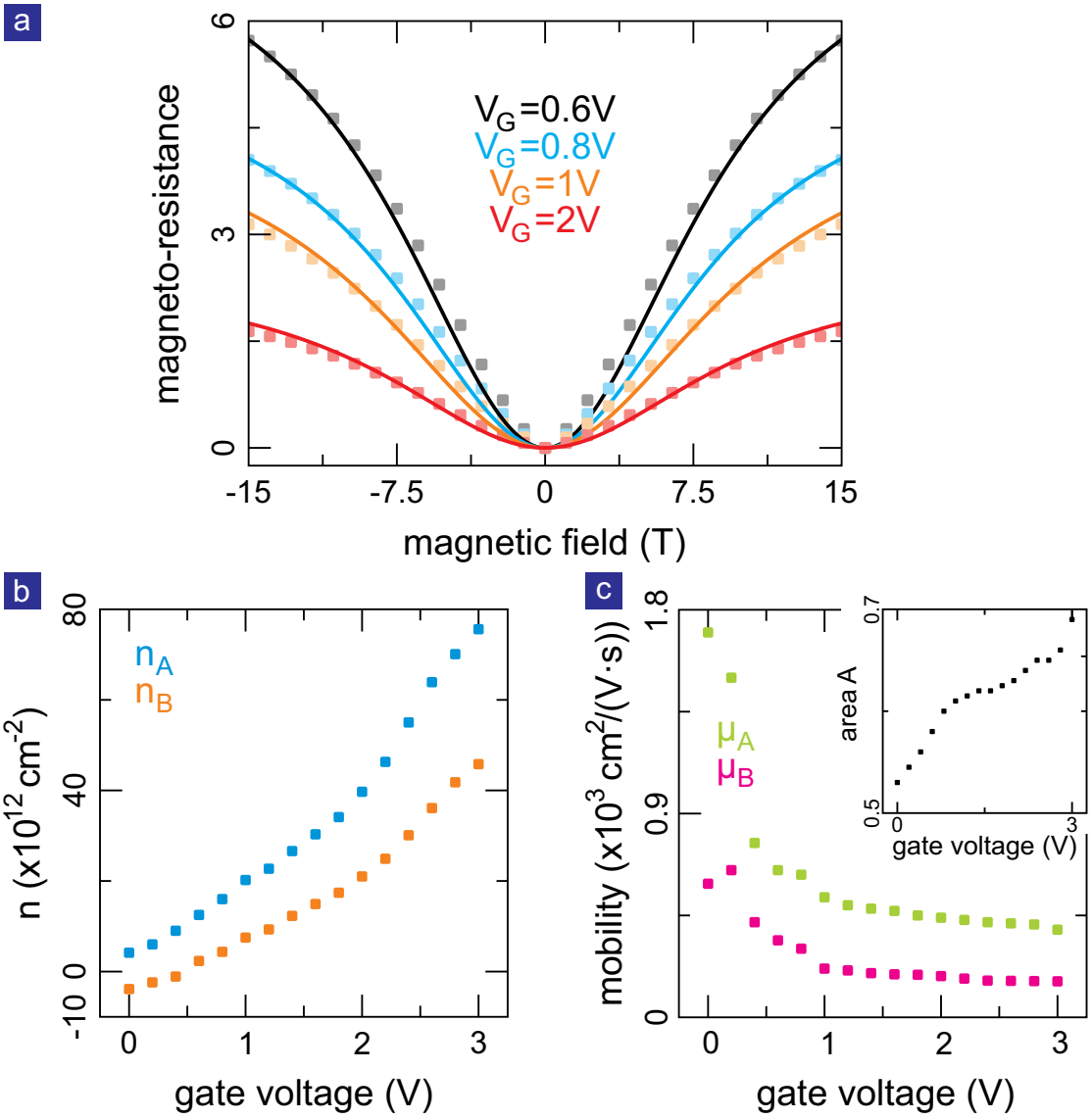

Figure 5.9: Multilayer graphene: fitting of MR with the SEMA model. (a) Dependence of experimental (squares) and fitted (lines) magneto-resistance on magnetic field for different values of gate voltage. Fitting parameters: (b) densities of area A (n_A) and B (n_B), (c) mobilities μ_A and μ_B of the two areas (Inset: spatial fraction of area A).

approaching the MCP. This is expected in bilayers. The mobility of regions B, μ_B reveals an unexpected behavior: at the CNP it drops to very low values and returns to the typical value when moving away from the electron-hole puddle region (see Figure 5.8-c). This can arise from localization at the charge neutrality point.

The areal fraction A monotonically decreases up to $V_G = 2.1$ V. For higher values of gate voltage, areas A grow again and the two carrier densities (n_A and n_B) simultaneously drop. This corresponds to the non-monotonic behavior of the

charge carrier density as measured by the Hall effect (see section 4.5). As in the case of monolayers, the filling of the oxide traps increases the disorder of the system. When further increasing the gate voltage the average carrier density rises and the MR decreases. As consequence, both densities n_A and n_B increase and p_A drops again.

The fitting of the data obtained on multilayer graphene reveals the presence of electron-hole puddles at zero gate voltage. Indeed n_A is always positive (electron), while n_B is negative (holes) for $V_G \leq 0.4$ V. This voltage range corresponds to the electron-hole puddle region determined by the Hall effect (see Figure 4.3-b). For higher values of gate voltage, the measured magneto-resistance monotonically decreases and the average charge concentration increases. As a result, the two fitted densities increase (as expected), and the areal fraction of one of the areas (in this case A) monotonically rises. The fitted mobilities μ_A and μ_B drop for increasing carrier density (gate voltage) as known from conventional field effect graphene devices [2].

In conclusion, mono-, bi- and multilayer graphene share the same behavior for low gate voltage (and near the charge neutrality point). The SEMA model indicates ordering of the system with increasing gate voltage. When the filling of trap states occurs, the decrease of charge carrier concentration in the channel is accompanied by an enhanced magneto-resistance. This is interpreted (within the SEMA approach) as an increase of the charge disorder due to the random distribution of the now charged oxide traps. The interpretation that the non-monotonic behavior is associated with the occupation of trap states in the SiO_2 is supported also by the monotonic behavior of the MR in multilayer graphene where screening prevents a filling of such traps.

5.3.2 Fit with the quadratic EMA model

In this Section we present the fit of the experimental data with the quadratic EMA approach (introduced in Section 5.2.2). This model assumes a quadratic magneto-resistance and is valid in the low magnetic field regime [120] (where MR is always quadratic). Here, we fit mono- and bilayer measurements, because multilayer data contain only few points for low magnetic field.

Figure 5.10-a shows the fit of experimental MR with the quadratic EMA in the range $[-3T, 3T]$ for different values of gate voltage. The only fitting parameter of the quadratic approach is the ratio between the average charge density and superposed fluctuations η (as shown in Section 5.2.2). Around the charge neutrality point, the average density and fluctuations have similar values, therefore their ratio is close to unity. This is in agreement with the fact that we can reliably determine the charge concentration with the Hall effect when the average density is higher than the fluctuations.

Increasing the gate voltage, the value of η rises: the influence of fluctuations become less important for the transport properties of the sample. In other words, the charge disorder of the sample drops. When the traps start to fill up, the ratio η decreases again (as shown in 5.10-b). The disorder induced by the filled oxide trap states is stronger than the "self-ordering" of the electric double layer for increasing gate voltage. When increasing V_G further, the ratio η rises again: the self-ordering

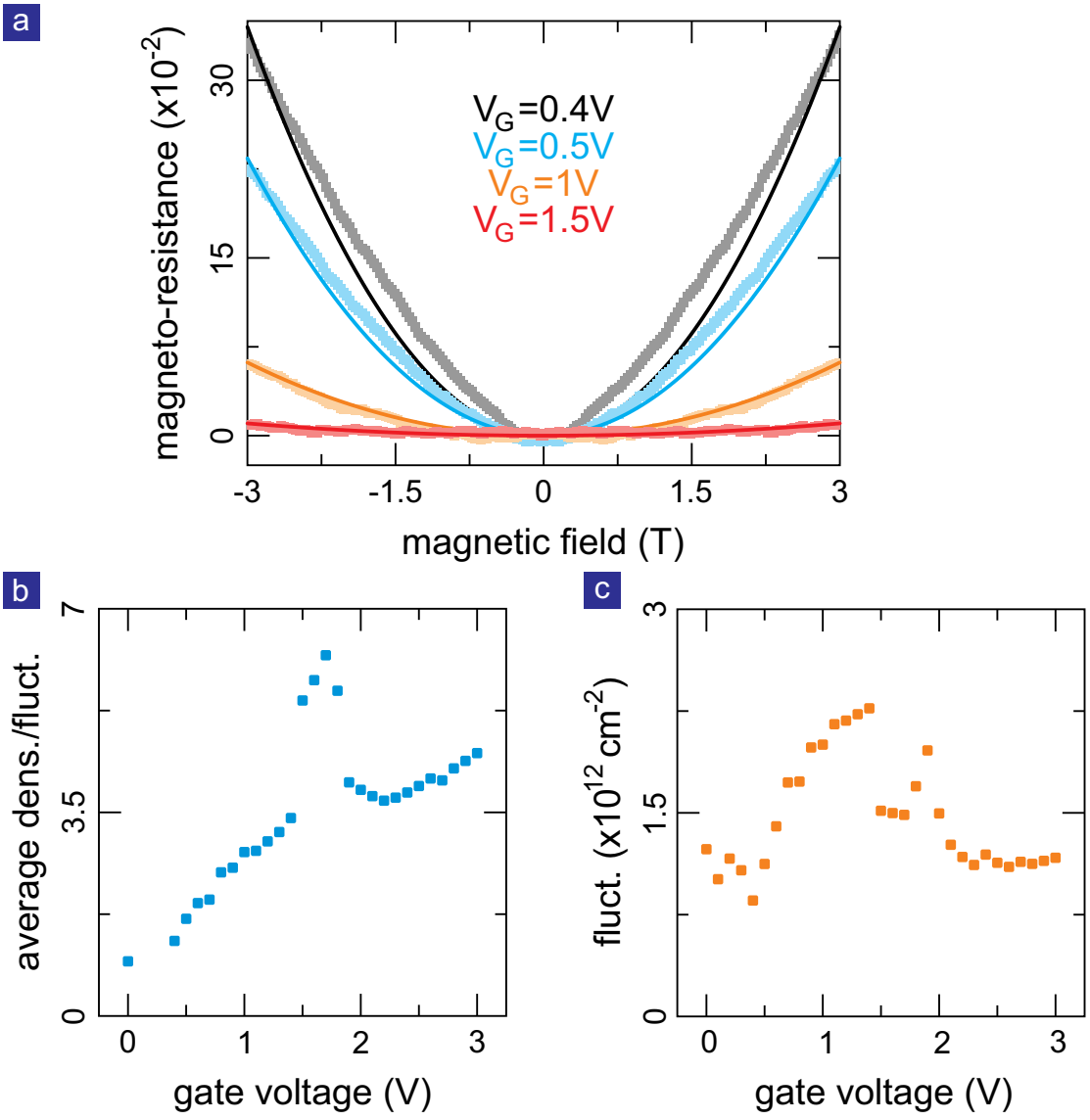

Figure 5.10: Monolayer graphene: fitting of MR with the quadratic EMA model. (a) Dependence of experimental (thick lines) and fitted (thin lines) magneto-resistance on magnetic field for different values of gate voltage. (b) Ratio between average density and charge fluctuations. (c) Absolute value of fluctuations.

of the ionic concentration becomes stronger than the disorder induced by the traps.

Knowing the ratio η and the average carrier density n_0, we can calculate the absolute value of the density variations n_{rms}. The latter is plotted for all the values of gate voltage in Figure 5.10-c. The absolute value of the n_{rms} increases for low values of gate voltage ($V_G \leq 1$ V). For intermediate gate voltages ($1 \leq V_G \leq 1.7$ V), n_{rms} saturates and eventually decreases. At the onset of the charge carrier concentration drop at $V_G = 1.7$ V, n_{rms} increases (i.e. the disorder rises). Finally, for even higher bias voltages ($V_G \geq 2V$), n_{rms} decreases and saturates around 1.2×10^{12}

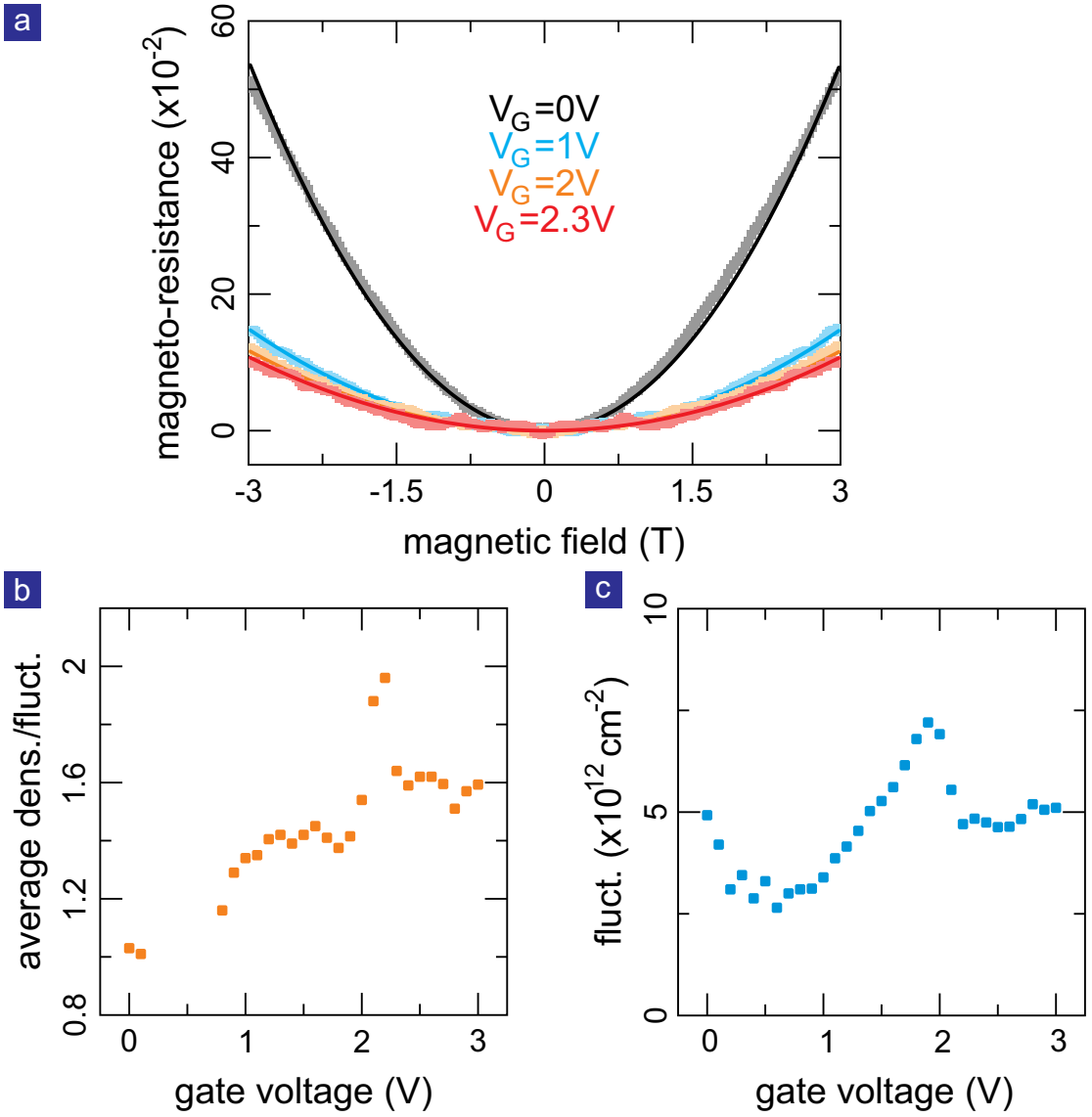

Figure 5.11: Bilayer graphene: fitting of MR with the quadratic EMA model. (a) Dependence of experimental (squares) and fitted (lines) magneto-resistance on magnetic field for different values of gate voltage. (b) Ratio between average density and charge fluctuations. (c) Absolute value of the charge density variation.

cm^{-2}. It is interesting to notice that n_{rms} is always on the order of 10^{12} cm^{-2}, that is one order of magnitude higher than in graphene placed on SiO_2 [88, 100–102]. This observation as well as the gate voltage dependence clearly indicate that the density variations are caused by the electrolyte gate.

The same analysis can be performed for bilayer graphene. The low magnetic field MR follows a quadratic behavior, and the EMA model fits the experimental data with high accuracy (as shown in Figure 5.11-a). The fitting parameter ν for bilayer

graphene follows the same gate voltage dependence as for monolayer graphene. Near the minimum conductivity point the charge fluctuations are bigger than the average carrier density and the Hall trace is non-linear. When the conduction is due to a single type of charge carrier (electrons or holes) the fluctuations are comparable to the average carrier density, therefore their ratio η approaches the unity (as shown in Figure 5.11-b). The ratio increases up to $V_G = 2.2$ V. At the onset of the filling of trap states ($V_G = 2$ V) charge transfer occurs and disorder becomes stronger again. At these values of carrier density, most the charge carriers reside in the top graphene layer in contact with the electrolyte. Therefore, the second graphene layer partially screens the inhomogenity stemming from trapped charges in the oxide. When the trap-induced disorder becomes more important, the ratio η decreases again and, finally, saturates for high values of V_G (as shown in Figure 5.11-b).

The amplitude of the density variations follows the same behavior as in monolayer graphene: n_{rms} first increases with increasing gate voltage, then it decreases when the average carrier density drops and finally saturates in the high gate voltage regime (as shown in Figure 5.11-c). The value of n_{rms} is constantly on the order of magnitude of 10^{12} cm^{-2}, that is the same of monolayer graphene and higher than in field-effect devices with a conventional gate [88, 100–102].

In conclusion, electrolyte-gated mono- and bilayer graphene show the same behavior of the charge disorder with gate voltage and order of magnitude of the charge density variations. The value is higher than for conventional gating (graphene on SiO_2 or BN) and changes with the bias applied to the electrolyte. Therefore , the analysis of the experimental data within the quadratic EMA theory suggests that the disorder is created by the electrolyte. The filling of trap states in the insulator increases the disorder.

5.4 Discussions

In order to evaluate the validity of the two models, we compare the results obtained by fitting the same magneto-resistance data. Since the two models use different fitting parameters, we need to find a common representation of the charge inhomogeneity provided by the different theories. The SEMA model (Section 5.2.1) provides the absolute values of the charge density in the two different regions, while the quadratic EMA theory (Section 5.2.2) provides the strength of charge fluctuations around an average value. So, we take the densities obtained from the SEMA model and we calculate the charge density variations. We compare the dependence of the ratio between the average density and the charge density fluctuations η as a function of the gate voltage within the two models for mono- and bilayer graphene. Since in monolayer graphene it is straightforward to convert the charge density to the energy of the Fermi level, we compare also the energy fluctuations associated with the charge inhomogeneity. Finally, we plot η also as a function of the average charge carrier density in order to correlate the behavior with the disorder induced by the electrolyte by the traps in the insulating substrate.

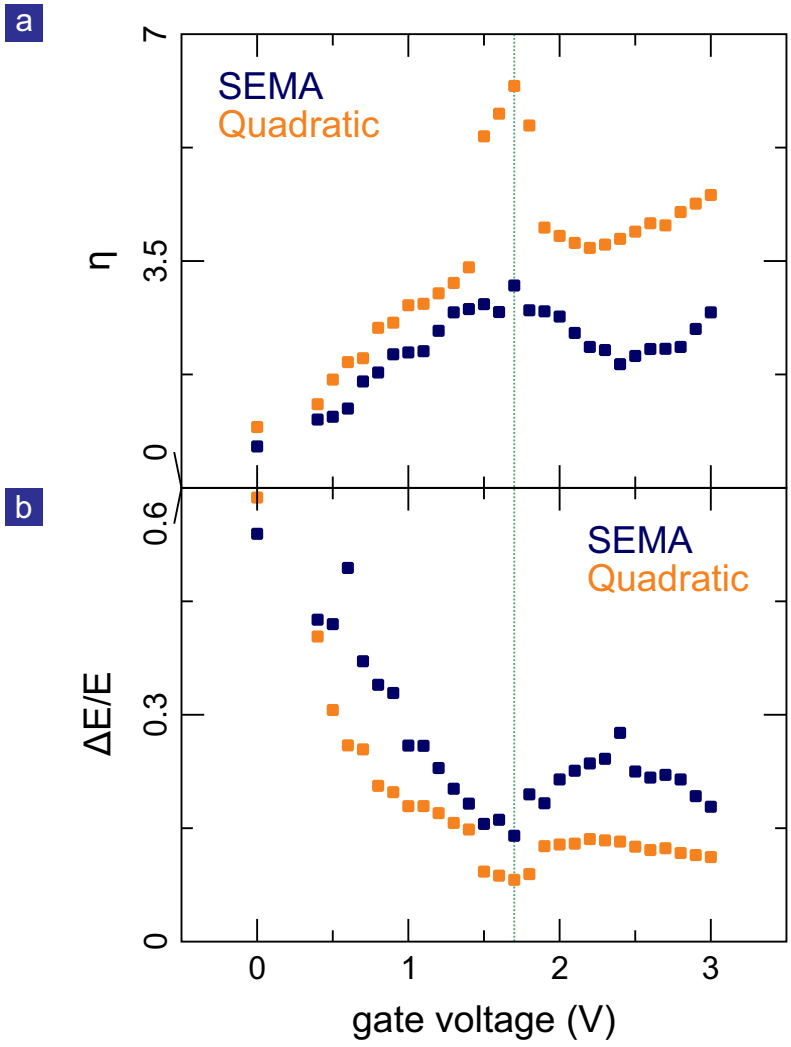

Figure 5.12: Monolayer graphene: comparison between the models. (a) The ratio between average carrier density and charge fluctuations as a function of the gate voltage for the SEMA (blue dots) and the quadratic EMA (orange symbols) model. (b) The relative fluctuation of the Fermi energy as a function of the gate voltage for the SEMA (blue dots) and the quadratic EMA (orange symbols) model. The vertical dotted green line marks the onset of the non-monotonicity of the average carrier density with gate voltage.

The dependence of η on the gate voltage is shown in Figure 5.12-a for the two different models. In the low gate voltage regime, the two models give a similar estimate of the charge fluctuations. In particular, both models give $\eta \sim 1$ for the first gate voltages with a reliable evaluation of the carrier density via Hall effect measurements. In both cases, the ratio between the average density and charge fluctuations rises for increasing V_G until the onset of the filling of the trapped states is reached. It is important to notice that the quadratic EMA model always provides

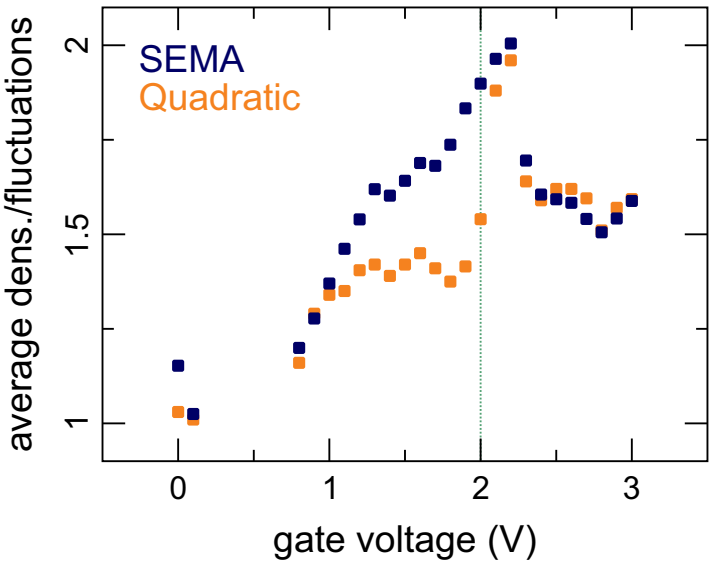

Figure 5.13: Bilayer graphene: comparison between the models. Dependence of the ratio between average carrier density and charge fluctuations on the gate voltage for SEMA (blue dots) and quadratic EMA (orange symbols) models. The vertical dotted green line depicts the onset of the non-monotonicity of average carrier density with gate voltage.

higher order of the charge distribution in the samples than the SEMA theory. Near the filling of the trap states, the models diverge in absolute value (see Figure 5.12-a). In the high gate voltage region, the ratio η shows a similar behavior for the two models, but the absolute value remains considerably different. In any case, the qualitative and quantitative agreement between the two models is good: in the worst case the density fluctuations determined with the SEMA approach have double the strength than those of the quadratic theory.

In monolayer graphene, the conversion of charge carrier concentration to a Fermi energy is straightforward [2], as shown in Section 1.4. Figure 5.12-b shows the relative fluctuations of the Fermi energy due to the charge inhomogeneity obtained with the two theoretical models. These energy fluctuations are the main reason for the strong magneto-resistance in charge inhomogeneous materials [125–128]. Therefore, the decrease of $\Delta E/E$ properly describes the drop of the MR with increasing gate voltage (see Figure 5.2) for gate voltages lower than 1.7 V. The increase of the magneto-resistance for higher values of gate voltage is explained by the increase of the energy fluctuation associated with the filling of trap states. For both models, the energy fluctuations have a maximum value around 60% and a minimum (at the onset of the trap filling) on the order of $10 - 15\%$.

The comparison of the fitting parameters of bilayer graphene obtained within the two models is shown in Figure 5.13. As for monolayer graphene, the ratio η grows from unity (near the minimum conductivity point) to about 2 (near the onset of the

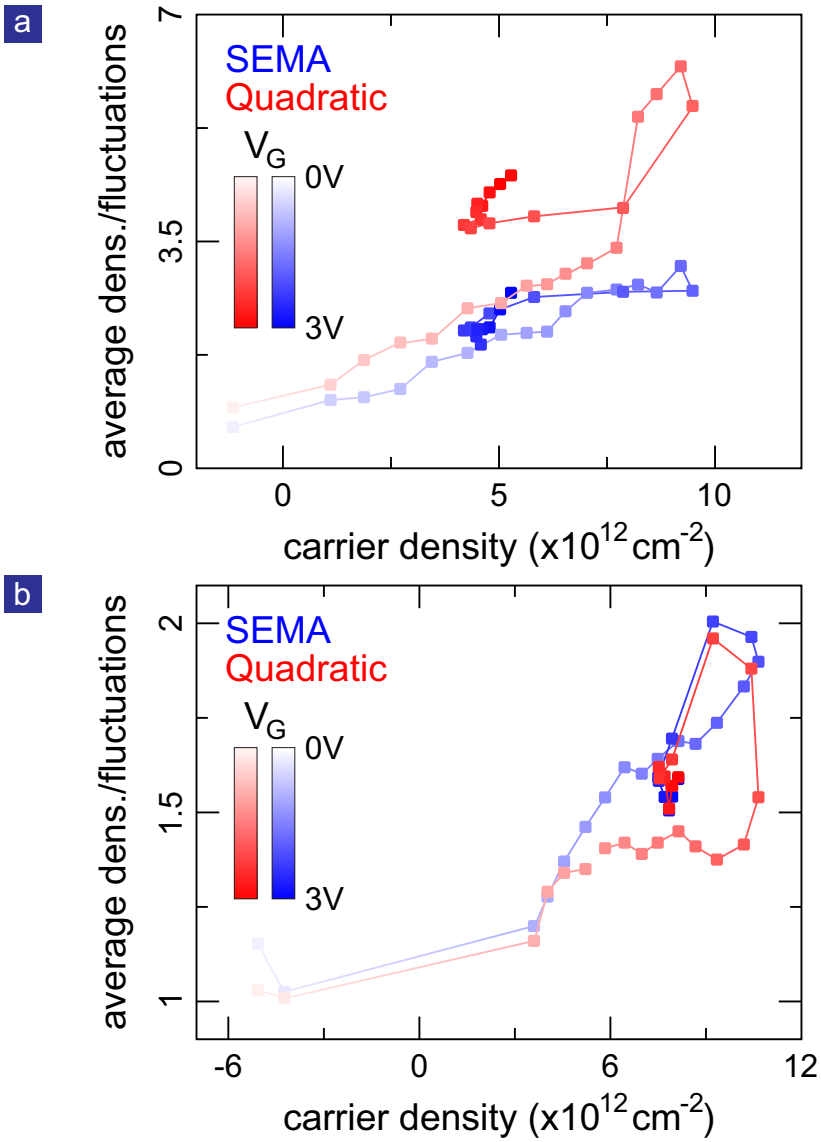

Figure 5.14: Dependence of η on the average charge concentration. (a) Monolayer graphene: η obtained with the SEMA model (blue squares) and the quadratic approach (red symbols) plotted against the average charge concentration. (b) Bilayer graphene: η obtained with the SEMA model (blue squares) and the quadratic approach (red symbols) plotted against the average charge concentration. Increasing values of gate voltage are depicted by enhanced darkness of the symbols.

filling of traps). For gate voltages lower than 2 V, the quadratic approach yields a higher disorder of the system. As in the monolayer case, the quadratic approach shows a jump of η near the average density drop. For high values of V_G the disorder estimated by the two models fits also from a quantitative point of view.

In multilayer graphene the conversion of the charge carrier concentration into a Fermi energy is not straightforward, because of screening. This may cause a non-

linear dependence on the density and the number of layers [103]. A proper evaluation of the Fermi energy may require a self-consistent recalculation of the electronic band dispersion.

5.5 Conclusions

Figure 5.14 shows η vs. n_0 for mono- (a) and bilayer (b) graphene, where the color gradient of the symbols represents the different values of gate voltage. In monolayer graphene, the quadratic EMA theory extracts higher charge order than the SEMA model for the entire carrier density range. At the same average charge concentration the charge fluctuations are stronger for lower values of gate voltage (i.e. before the trap states filling) within both descriptions. Bilayer graphene shows a similar behavior as monolayers, but the SEMA theory yields a slightly more disordered system after the average carrier density has dropped due to filling of the trapped states. The amplitudes of the density fluctuations given by the two models are the same for large gate voltage. Within the SEMA model, the fluctuations at the same average density have a similar value before and after the drop of charge concentration both in mono- and bilayer samples. According to the quadratic approach more ordering exists, but in bilayer graphene the difference in the amplitude of the fluctuations is lower than in the monolayer case.

Differently from solid gated graphene, the strength of the charge inhomogeneity changes with gate voltage both for mono- and bilayers. This is different from conventional graphene field effect devices. Polar adsorbates on the silicon dioxide substrate and residuals of the device fabrication process cause these electron hole puddles and there is no variation with gate voltage [99].

The maximum value of charge inhomogeneity in conventional gated samples is on the order of 10^{11} cm^{-2} [88, 100–102]. Therefore, for an average charge concentration of 10^{13} cm^{-2} the value of η would be 100. This is at least 35 times bigger than what we measure in electrolyte gated mono- and bilayer graphene. Therefore, we can conclude that electrolyte gating enhances the charge disorder of graphene by at least one order of magnitude.

Chapter 6

Evidence for intercalation in bilayer graphene

Intercalation with different species and concentrations allows to tune the electrical, thermal and magnetic properties of the host graphitic based material. The intercalation process has been intensively studied during the last five decades [8]. All attempts have suffered from the presence of structural defects in the graphite crystal. Bilayer graphene is the thinnest graphitic material that can be intercalated. Studying the intercalation process in high quality bilayers (exfoliated graphene) may further insights into the intercalation process. This chapter is devoted to the study of intercalation of bilayer graphene using electrolyte gating. In the first paragraph (6.1), we present the differences in the behavior of the charge concentration at high gate voltage between mono-, bi- and multilayer graphene. This is followed by an analysis of the temperature dependence of the resistivity of bilayer graphene when intercalation has taken place (paragraph 6.2). In paragraph 6.3, we discuss the magneto-transport properties of bilayer graphene at low temperature. Finally, we summarize all arguments that indeed indicate that intercalation takes place under high applied gate voltages in electrolyte gated bilayer graphene (paragraph 6.4).

6.1 Charge concentration at high gate voltage

Hall measurements were carried out on electrolyte gated graphene at higher gate voltages as investigated in the chapter 4 where the behavior was studied for $V_G \leq 3$ V. Figure 6.1 displays the dependence of the carrier concentration on the gate voltage for graphene devices of different thickness. Here we focus on high gate voltages. Monolayer graphene shows a different behavior than bi- and multilayer graphene. In monolayers the charge carrier concentration increases linearly with the gate voltage. At high voltages, the slope is smaller than for low values of V_G. This is probably due to the simultaneous filling of the oxide trap states, that decreases the gating efficiency. In bi- and multilayers n rises quickly for gate voltage values exceeding 3.5 V. The rate at which n increases is bigger than for low V_G and the

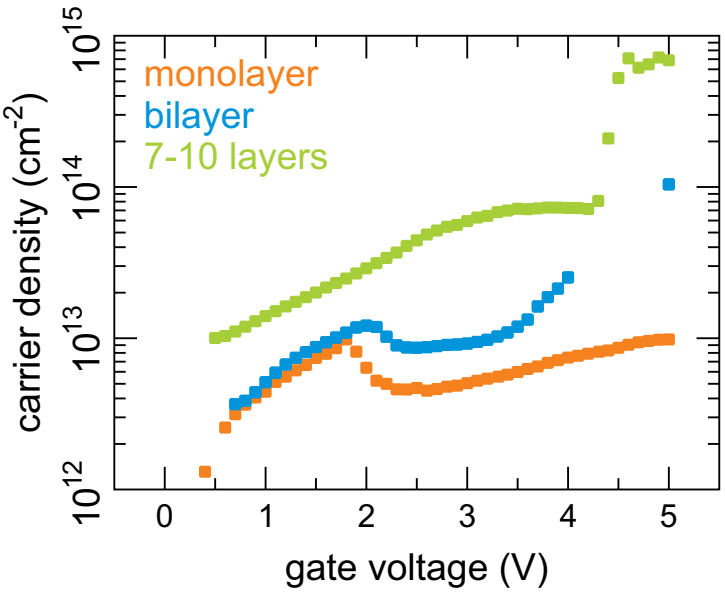

Figure 6.1: Carrier density of electrolyte gated graphene. The charge carrier concentration extracted from Hall measurements is plotted against the gate voltage for mono- (orange dots), bi- (azure squares) and multilayer (green symbols) graphene.

overall increase is about one order of magnitude. For multilayer graphene the rise of the charge carrier concentration is abrupt. Its steepness is higher than for bilayers. The different behavior between monolayer and multilayer (thickness $\geq$ 2 layers) graphene at large gate voltage is attributed to the intercalation of lithium ions in between the graphene layers [8]. When the gate voltage is large enough, Li ions acquire enough energy to enter in between the graphene planes. As a consequence, the charge carrier concentration rises [29, 34]. Since each lithium ion donates one electron to graphene, it is possible to evaluate the concentration of intercalants through Hall effect data. The charge carrier concentration due to the electric double layer is deduced by extrapolating the linear increase of n with V_G before intercalation took place. The ion concentration is taken as the difference between the carrier density evaluated by the Hall effect and the extrapolated EDL contribution. In bilayer graphene the Li density is estimated to be about 9×10^{13} cm^{-2}. The density of carbon atoms in graphene is 3.8×10^{15} cm^{-2} [140]. Considering that the Li ions are sandwiched between two graphene layers, the resulting GIC has formula LiC_{80}. In case of multilayer graphene the chemical formula of the compound ranges from LiC_{38} (considering 7 layers) to LiC_{54} (considering 10 layers).

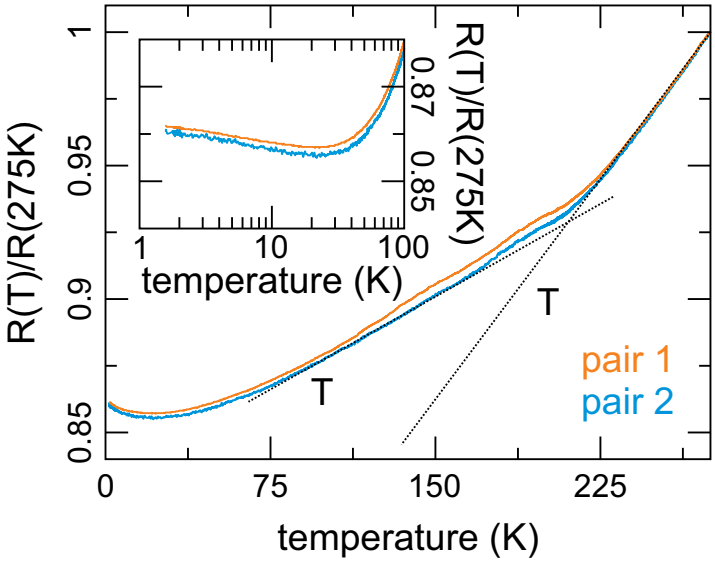

Figure 6.2: Temperature dependence of the normalized resistance. The normalized resistance R(T)/R(275K) of bilayer graphene (at $n = 1.04 \times 10^{14}$ cm^{-2}) is plotted against the temperature for two different pairs of electrodes (orange and azure lines). Regions with linear temperature dependence of the resistance are highlighted by dotted lines. The inset shows the low temperature dependence of the normalized resistance.

6.2 Temperature dependence of the transport properties

We have investigated the temperature dependence of the transport properties of electrolyte gated bilayer graphene at the maximum charge carrier concentration ($n = 1.04 \times 10^{14}$ cm^{-2}). Figure 6.2 displays the evolution of the normalized resistance (R(T)/R(275K)) with decreasing temperature for two different pairs of electrodes. Both resistances show the same behavior. A linear temperature dependence is measured for $T \geq 225$ K. This is usually observed in metallic electronic systems. Generally, it is attributed to phonon scattering [10]. A linear dependence of resistance with temperature was already observed in electrolyte gated monolayer graphene at high carrier concentrations [93]. In the range 100-150 K the resistance has a linear dependence on temperature with a different slope (see Figure 6.2). In electrolyte gated monolayer graphene, a steeper T^4 dependence of the resistance (related to electron-phonon scattering in the quantum limit) has been reported in the same temperature range [93]. At low temperature ($T \leq 50$ K), the sample resistance shows a logarithmic increase with decreasing temperature (see inset of Figure 6.2). In a two dimensional electronic system, two mechanisms can give rise to a logarithmic resistance increase: weak localization (WL) [141] and electron-electron

Coulomb interaction [142]. Weak localization is the result of the interference of electron waves propagating in opposite direction around a closed loop [141]. These closed loops are created when scattering from static defects dominates [34]. In electronic systems without spin-orbit coupling such electron interference is constructive, because the electrons traveling along two opposite paths acquire exactly the same phase [143]. This causes an increase of the overall resistance. The electron-electron Coulomb interaction in the metallic regime ($k_F l \gg 1$ where l is the mean free path) leads to diffusive behavior of the charge carriers [142] and the resistance of the 2D electronic system increases when lowering the temperature. Both phenomena are due to disorder [34] and could be the reason for the low temperature behavior of the resistance of our samples.

6.3 Magneto-transport at low temperatures

It is possible to distinguish between WL and Coulomb interaction as the scattering mechanism responsible for the observed temperature dependence at low temperature [34]. A perpendicular magnetic field destroys weak localization, because it annihilates the constructive interference of the electron waves traveling along opposite paths [144]. As a consequence, the resistivity drops with increasing (low) magnetic field. On the contrary, the electron-electron Coulomb interaction is not sensitive to small perpendicular magnetic fields [145]. This implies that the resistance does not change with an applied perpendicular magnetic field. Figure 6.3 depicts the magneto-transport data acquired at different temperatures. We conclude that the observed peak at zero magnetic field (the small shift is due to the persistent field of the magnet) is a characteristic feature of weak localization [143, 144]. The logarithmic increase of resistance with decreasing temperature (shown in paragraph 6.2) originates from WL. Weak localization persists up to $T \simeq 100$ K. This value is much higher than what was previously measured in bilayer graphene [144]. It suggests a strong disorder of the electronic system.

Below we analyze the temperature dependence in more detail. This allows to evaluate the scattering mechanisms involved. In bilayer graphene, the magneto-conductance due to weak localization can be expressed as [143]:

$$\begin{aligned} \Delta\sigma(B) &= \frac{e^2}{\pi h}\left[F\left(\frac{B}{B_\phi}\right) - F\left(\frac{B}{B_\phi + 2B_i}\right) + 2F\left(\frac{B}{B_\phi + 2B_*}\right)\right] \\ F(z) &= lnz \; + \; \Psi\left(\frac{1}{2} + \frac{1}{z}\right) \\ B_{\phi,i,*} &= \frac{\hbar}{4De}\tau^{-1}_{\phi,i,*}. \end{aligned} \tag{6.1}$$

Here, $\Psi(x)$ is the digamma function, D is the diffusion coefficient, τ_ϕ is the dephasing time, τ_i is the temperature independent intervalley scattering time, and

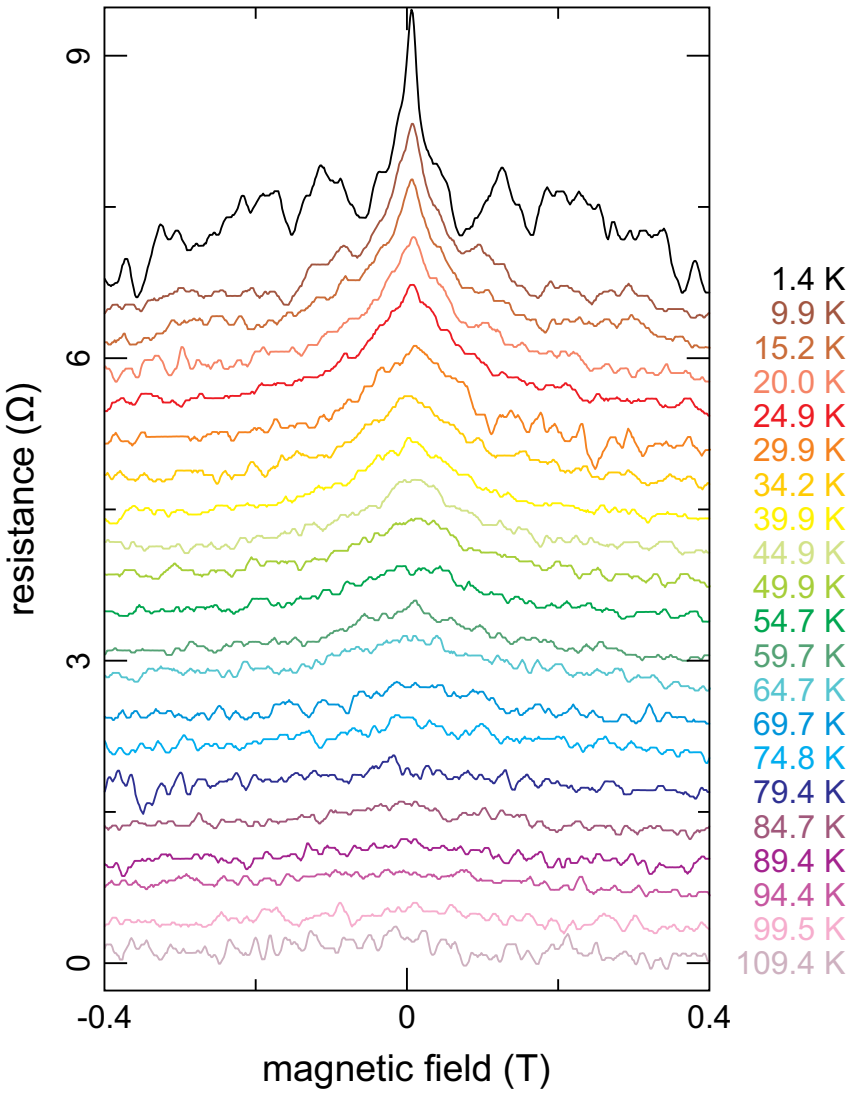

Figure 6.3: Magneto-resistance at different temperatures. Dependence of the longitudinal resistance on the perpendicular magnetic field at different temperatures. The traces are vertically shifted for clarity.

$\tau_* = \frac{\tau_i \tau_W}{\tau_i + \tau_W}$ with τ_W the intravalley scattering time related to the warping and chirality breaking. Strong warping is expected in bilayer graphene at high charge carrier concentration [2]. In this case, the intravalley scattering time is small ($\tau_W \to 0$). The coherence length takes on the form $L_\phi = (D\tau_\phi)^{1/2}$. Figure 6.4-a displays the fit of the magneto-conductance at 1.4 K. Since the warping is assumed to be strong, the fit was performed using the first two terms of equation 6.1 only. The obtained intervalley scattering time has the value $\tau_i = 0.45$ ps for all temperatures. The dephasing rate τ_ϕ^{-1} shows a linear increase with temperature (see Figure 6.4-b). This can be attributed to electron-electron interaction [146]. The coherence length L_ϕ

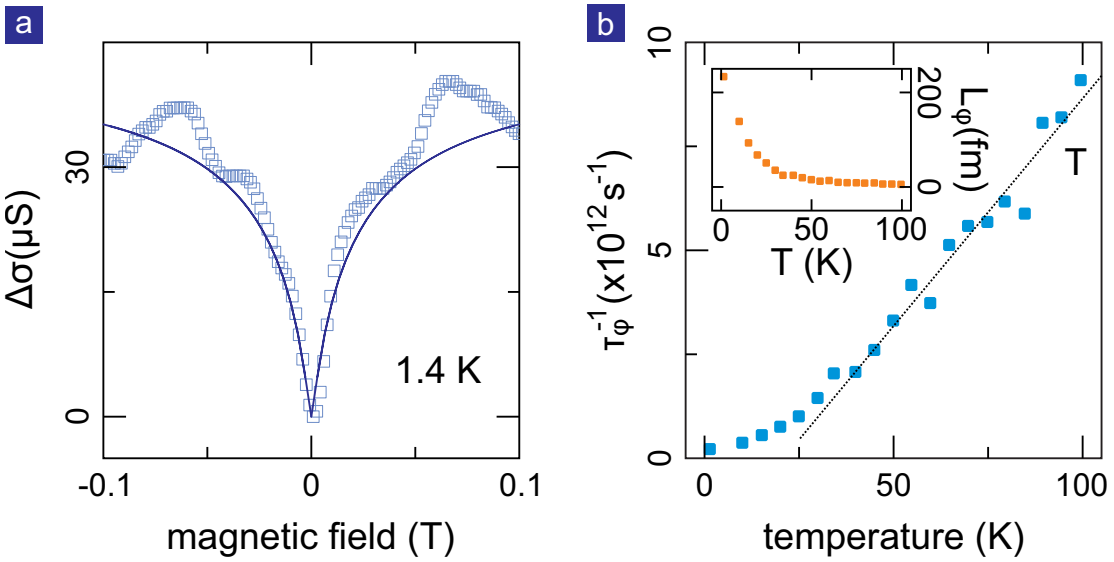

Figure 6.4: Fit of weak localization. (a) Comparison of the experimental data (open squares) with the fit (solid line) for 1.4 K. (b) Temperature dependence of the dephasing rate τ_ϕ^{-1}. The linear dependence is depicted. Inset: coherence length L_ϕ as function if the temperature.

saturates at high temperatures. This is the result of the inhomogeneous distribution of charges across the sample [144]. All the scattering times and the coherence length are shorter than in bilayer graphene exfoliated on silicon dioxide [144]. This confirms that electrolyte gating induced intercalation generates strong disorder in the electronic system. For the sake of completeness we note that away from $B = 0$ aperiodic resistance oscillations appear across the entire magnetic field range shown in Figure 6.3. These are so-called universal conductance fluctuations. They too originate from disorder and coherence effects of the electronic wavefunction [147].

6.4 Conclusions

We determined the charge carrier concentration in electrolyte gated mono-, bi-, and multilayer graphene at high gate voltages. The dependence of n on V_G is different for monolayer graphene and multilayer graphene. This suggests intercalation. We investigated the temperature dependence of the resistance of bilayer graphene in the high gate voltage regime. There are three different behaviors with temperature: for $T \geq 225$ K the resistance depends linearly on the temperature (electron-phonon interaction), in the range 100-150 K the dependence is linear again (with another slope), while for low temperatures the sample resistance shows a logarithmic increase (weak localization). The temperature dependence of the weak localization peak suggests that electron-electron interaction is the leading mechanism of the creation of WL. We note that our observations and conclusions on bilayer graphene are

in agreement with reports on graphite. There too weak localization and electron-electron interaction were addressed as signs of charge disorder due to intercalation [8, 34].

Chapter 7

Zusammenfassung

Graphen ist eine einzelne Schicht von Kohlenstoffatomen, die in einem hexagonalen Gitter angeordnet sind. Es ist der Grundbaustein von Graphit, das aus schwach gebundenen, übereinander geschichteten Graphenlagen besteht. Graphen wurde 2004 durch mikromechanischer Exfolierung von Graphit isoliert [1]. Die Wechselwirkung zwischen Kristallgitter und Ladungsträgern führt zu einer linearen Dispersionsrelation der Elektronen. Daher verhalten sich die Ladungsträger in Graphen wie masselose, chirale Teilchen. Viele interessante physikalische Phänomene wurden in Graphen beobachtet, wie zum Beispiel der ganzzahlige Quanten-Hall-Effekt bei Raumtemperatur, der fraktionale Quanten-Hall-Effekt, der ballistische Transport bei hohen Temperaturen und auch der Hofstadter-Schmetterling [2, 3]. Die Existenz von Supraleitung in Graphen wurde für sehr hohe Ladungsträgerdichten vorhergesagt [4, 5], konnte aber bislang nicht experimentell verifiziert werden. Solch hohe Ladungsträgerdichten konnten in verschiedenen Materialien mittels Feldeffekt unter Verwendung eines Elektrolyten induziert werden [6, 7]. Die dabei erreichten Dichten sind eine Größenordnung kleiner als bei chemischer Dotierung, jedoch zwei Größenordnungen größer als bei Verwendung einer klassischen Gate-Elektrode. Im Gegensatz zur chemischen Dotierung beeinflusst die Ladungserhöhung mittels elektrischen Feldes nicht die Kristallstruktur der untersuchten Materialien. Wird zu diesem Zweck ein Elektrolyt verwendet, so kann es allerdings zu Interkalation von Ionen zwischen den Graphenschichten kommen. Dies bewirkt Veränderungen in den physikalischen Eigenschaften von Graphen [8].

References

[1] Novoselov, K. S., Geim, A. K., Morozov, S. V., Jiang, D., Zhang, Y., Dubonos, S. V., Grigorieva, I. V., and Firsov, A. A. *Science* **306**, 666–669 (2004).

[2] Neto, A. H. C., Guinea, F., Peres, N. M. R., Novoselov, K. S., and Geim, A. K. *Rev. Mod. Phys.* **81**, 109–162 (2009).

[3] Ponomarenko, L. A., Gorbachev, R. V., Yu, G. L., Elias, D. C., Jalil, R., Patel, A. A., Mishchenko, A., Mayorov, A. S., Woods, C. R., Wallbank, J. R., Mucha-Kruczynski, M., Piot, B. A., Potemski, M., Grigorieva, I. V., Novoselov, K. S., Guinea, F., Falko, V. I., and Geim, A. K. *Nature* **497**, 594–597 (2013).

[4] Nandkishore, R., Levitov, L. S., and Chubukov, A. V. *Nature Phys.* **8**, 158–163 (2012).

[5] Profeta, G., Calandra, M., and Mauri, F. *Nature Phys.* **8**, 131–134 (2012).

[6] Daghero, D., Paolucci, F., Sola, A., Tortello, M., Ummarino, G. A., Agosto, M., Gonnelli, R. S., Nair, J. R., and Gerbaldi, C. *Phys. Rev. Lett.* **108**, 066807 (2012).

[7] Ueno, K., Nakamura, S., Shimotani, H., Ohtomo, A., Kimua, N., Nojima, T., Aoki, H., Iwasa, Y., and Kawasaki, M. *Nature Mater.* **7**, 855–858 (2008).

[8] Dresselhaus, M. S. and Dresselhaus, G. *Advances in Physics* **51**, 1–186 (2002).

[9] Chung, D. D. L. *J. Mater. Sci.* **37**, 1475–1489 (2002).

[10] Ibach, H. and Lüth, H. *Solid-State Physics.* Springer-Verlag, (1995).

[11] Wallace, P. R. *Phys. Rev.* **71**, 622–634 (1947).

[12] Slonczewski, J. C. and Weiss, P. R. *Phys. Rev.* **109**, 272–279 (1958).

[13] Partoens, B. and Peeters, F. M. *Phis. Rev. B* **74**, 075404 (2006).

[14] Geim, A. K. and Novoselov, K. S. *Nature Mater.* **6**, 183–191 (2007).

[15] Manes, J. L., Guinea, F., and Vozmediano, M. A. H. *Phis Rev. B* **75**, 155424 (2007).

[16] Koshino, M. and Ando, T. *Solid State Commun.* **149**, 1123–1127 (2009).

[17] McCann, E. and Koshino, M. *Rep. Prog. Phys.* **76**, 056503 (2013).

[18] Zhang, F., MacDonald, A. H., and Mele, E. J. *PNAS* **110**, 10546–10551 (2013).

[19] McCann, E. and Falko, V. I. *Phis. Rev. Lett.* **96**, 086805 (2006).

[20] Trickey, S. B., Müller-Plathe, F., diercksen, G. H. F., and Boettger, J. C. *Phys. Rev. B* **45**, 4460–4468 (1992).

[21] Castro, E. D., Novoselov, K. S., Morozov, S. V., Peres, N. M. R., dos Santos, J. M. B. L., Nilsson, J., Guinea, F., Geim, A. K., and Neto, A. H. C. *Phis. Rev. Lett.* **99**, 216802 (2007).

[22] Ando, T. *J. Phys. Soc. Jpn.,* **80**, 014707 (2011).

[23] Novoselov, K. S., Geim, A. K., Morozov, S. V., Jiang, D., Katsnelson, M. I., Grigorieva, I. V., Dubonos, S. V., and Firsov, A. A. *Nature* **438**, 197–200 (2005).

[24] Hobson, J. P. and Nierenberg, W. A. *Phys. Rev.* **89**, 662 (1952).

[25] Ashcroft, N. W. and Mermin, N. D. *Solid State Physics*. Brooks/Cole, (1975).

[26] McChesney, J. L., Bostwick, A., Ohta, T., Seyller, T., Horn, K., Gonzàlez, J., and Rotenberg, E. *Phys. Rev. Lett.* **104**, 136803 (2010).

[27] Mazin, I. I., Boeri, L., Dolgov, O. V., Golubov, A. A., Bachelet, G. B., Giantomassi, M., and Andersen, O. K. *Physica C* **460-462**, 116–120 (2007).

[28] Emery, N., herold, C., Mareche, J.-F., and Lagrange, P. *Sci. Technol. Adv. Mater.* **9**, 044102 (2008).

[29] Csány, G., Littlewood, P. B., Nevidomsky, A. H., Pickard, C. J., and Simons, B. D. *Nature Phys.* **1**, 42–45 (2005).

[30] Millman, S. E. and Kirczenow, G. *Phys. Rev. B* **26**, 2310–2313 (1982).

[31] Dimiev, A. M., Ceriotti, G., Behabtu, N., Zakhidov, D., Pasquali, M., Saito, R., and Tour, J. M. *Nano Lett.* **7**, 2773–2780 (2013).

[32] Safran, S. A. *Phys. Rev. Lett.* **44**, 937–940 (1980).

[33] Matsumoto, R., Hoshina, Y., and Akuzawa, N. *Mater. Trans.* **50**, 1607–1611 (2009).

[34] Piraux, L., Bayot, V., Michenaud, J.-P., and Issi, J.-P. *Phys. Scripta* **37**, 942–947 (1988).

[35] Weller, T. E., Ellerby, M., Saxena, S. S., Smith, R. P., and Smith, N. T. *Nature Phys.* **1**, 39–41 (2005).

[36] Tortello, M., Sola, A., Sharda, K., Paolucci, F., Nair, J. R., Gerbaldi, C., Daghero, D., and Gonnelli, R. *Appl. Surf. Sci.* **269**, 17–22 (2013).

[37] Li, C., Wang, B., Lin, S., Lin, J., Tong, P., Lu, W., and Sun, Y. *J. Magn. Man. Mater.* **323**, 2233–2237 (2011).

[38] Basov, D. N. and Chubukov, A. V. *Nature Phys.* **7**, 272–276 (2011).

[39] Sproul, A. B. and Green, M. A. *J. Appl. Phys.* **70**, 846–854 (1991).

[40] Dziewior, J. and Silber, D. *Appl.Phys. lett.* **35**, 170–172 (1979).

[41] Lilienfeld, J. E. *Patent* **US1745175** (1925).

[42] Heil, O. *Patent* **DEX439457** (1935).

[43] Kahng, D. *Patent* **US3102230** (1960).

[44] Salleo, A., Chabinyc, M. L., Yang, M. S., and Street, R. A. *Appl. Phys. Lett.* **81**, 4383–4385 (2002).

[45] Brown, A. R., Jarrett, C. P., de Leeuw, D. M., and Matters, M. *Synthetic metals* **88**, 37–55 (1997).

[46] Fahad, H. M., Smith, C. E., Rojas, J. P., and Hussain, M. M. *Nano Lett.* **11**, 4393Ű4399 (2011).

[47] Mannhart, J., Bednorz, J. G., Mueller, K. A., and Schlom, D. G. *Z. Phys. B* **83**, 307–311 (1991).

[48] Locklin, J., Shinbo, K., Onishi, K., Kaneko, F., Bao, Z., and Advincula, R. C. *Chem. Mater.* **15**, 14SS4–1412 (2003).

[49] Brattain, W. H. and Garrett, C. G. B. *Bell Syst. Tech. J.* **34**, 129–176 (1955).

[50] Chao, S. and Wrighton, M. S. *J. Am. Chem. Soc.* **109**, 6627–6631 (1987).

[51] Panzer, M. J., Newman, C. R., and Frisbie, C. D. *Appl. Phys. Lett.* **86**, 103503 (2005).

[52] Helmholtz, H. *Annalen der Physik und Chemie* **165**, 211Ű233 (1853).

[53] Gouy, G. *Compt. Rend.* **149**, 654 (1910).

[54] Chapman, D. L. *Philos. Mag.* **25**, 475–481 (1913).

[55] Stern, O. *Zeit. Elektrochem* **30**, 508–56 (1924).

[56] Kirby, B. J. *Micro- and Nanoscale Fluid Mechanics.* Cambridge University Press, (2013).

[57] Hahin, R. and Campbell, D. T. *J. Gen. Physiol.* **82**, 785–805 (1983).

[58] Russel, W., Saville, D. A., and Schowalter, W. R. *Colloidal Dispersions.* Cambridge University Press, (1989).

[59] Hall, E. H. *Amer. J. Math.* **2**, 287–292 (1879).

[60] Inzelt, G. *Electrochemical Methods.* Springer-Verlag, (2010).

[61] Kim, S. H., Hong, K., Xie, W., Lee, K. H., Zhang, S., Lodge, T. P., and Frisbie, C. D. *Adv. Mater.* **25**, 1822–1846 (2013).

[62] Riess, I. *Science and Technology of Fast Ion Conductors* , 23–50 (1989).

[63] Agrawal, R. C. and Pandey, G. P. *J. Phys. D: Appl. Phys.* **41**, 223001 (2008).

[64] Lei, Y. and Lodge, T. P. *Soft Matter* **8**, 2110 (2012).

[65] Prassides, K. *Nature Mater.* **0**, 96–98 (2010).

[66] Dean, C. R., Young, A. F., Meric, I., Lee, C., Wang, L., Sorgenfrei, S., Watanabe, K., Taniguchi, T., Kim, P., Shepard, K. L., and Hone, J. *Nature Nanotech.* **5**, 722–726 (2010).

[67] Chae, D.-H., Zhang, D., Huang, X., and von Klitzing, K. *Nano Lett.* **12**, 3905–3908 (2012).

[68] Park, J., Mitchel, W. C., Grazulis, L., Smith, H. E., Eyink, K. G., Boeckl, J. J., Tomich, D. H., Pacley, S. D., and Hoelscher, J. E. *Adv. Mater.* **22**, 4149–4145 (2010).

[69] Jerng, S. K., Yu, D. S., Kim, Y. S., Ryou, J., Hong, S., Kim, C., Yoon, S., Efetov, D. K., Kim, P., and Chun, S. H. *J. Phys. Chem. C* **115**, 4491–4494 (2011).

[70] Yu, Q. K., Lian, J., Li, S. S. H., Chen, Y. P., and Pei, S. S. *Appl. Phys. Lett.* **93**, 113103 (2008).

[71] Zhang, Y., Zhang, L., and Zhou, C. *Acc. Chem. Res.* **46**, 2329–2339 (2013).

[72] Berger, C., Song, Z., Li, T., Li, X., Ogbazghi, A. Y., Feng, R., Dai, Z., Marchenkov, A. N., Conrad, E. H., First, P. N., and de Heer, W. A. *J. Phys. Chem. B* **108**, 19912–19916 (2004).

[73] Emtsev, K. V., Bostwick, A., Horn, K., Jobst, J., Kellogg, G. L., Ley, L., McChesney, J. L., Ohta, T., Reshanov, S. A., Röhrl, J., Rotenberg, E., Schmid, A. K., Waldmann, D., Weber, H. B., and Seyller, T. *Nature Mater.* **8**, 203–207 (2009).

[74] Riedl, C., Coletti, C., Iwasaki, T., Zakharov, A. A., and Starke, U. *Phys. Rev. Lett.* **103**, 246804 (2009).

[75] Chakrabarti, A., Lu, J., Skrabutenas, J. C., Xu, T., Xiao, Z., Maguireb, J. A., and Hosmane, N. S. *J. Mater. Chem.* **21**, 9491–9493 (2011).

[76] Colombo, L., Li, X., Han, B., Magnuson, C., Cai, W., Zhu, Y., and Ruofl, R. S. *Phys Chem Chem Phys.* **13**, 20836–20843 (2011).

[77] Viculis, L. M., Mack, J. J., and Kaner, R. B. *Science* **299**, 1361 (2003).

[78] Pierson, H. O. *Handbook of Carbon, Graphite, Diamond and Fullerenes.* Noyes Publication, (1993).

[79] Blake, P., Hill, E. W., Neto, A. H. C., Novoselov, K. S., Jiang, D., Yang, R., Booth, T. J., and Geim, A. K. *Appl. Phys. Lett.* **91**, 063124 (2007).

[80] Raman, C. V. and Krishnan, K. S. *Nature* **121**, 501–502 (1928).

[81] Reich, S. and Thomsen, C. *Phil. Trans. R. Soc. Lond. A* **362**, 2271–2288 (2004).

[82] Ferrari, A. C., Meyer, J. C., Scardaci, V., Casiraghi, C., Lazzeri, M., Mauri, F., Piscanec, S., Jiang, D., Novoselov, K. S., and Geim, A. K. *Phys. Rev. Lett.* **97**, 187401 (2006).

[83] Al-Jishi, R. and Dresselhaus, G. *Phys. Rev. B* **26**, 4514–4522 (1982).

[84] Das, A., Pisana, S., Chakraborty, B., Piscanec, S., Saha, S. K., Waghmare, U. V., Novoselov, K. S., Krishnamurthy, H. R., Geim, A. K., Ferrari, A. C., and Sood, A. K. *Nature Nanotech.* **3**, 210–215 (2008).

[85] Thomsen, C. and Reich, S. *Phys. Rev. Lett.* **85**, 5214–5217 (2000).

[86] Mayorov, A. S., Gorbachev, R. V., Morozov, S. V., Britnell, L., Jalil, R., Ponomarenko, L. A., Blake, P., Novoselov, K. S., Watanabe, K., Taniguchi, T., and Geim, A. K. *Nano Lett.* **11**, 2396–2399 (2011).

[87] Zomer, P. J., Dash, S. P., Tombros, N., and van Wees, B. J. *Appl. Phys. Lett.* **99**, 232104 (2011).

[88] Burson, K. M., Cullen, W. G., Adam, S., Dean, C. R., Watanabe, K., Taniguchi, T., Kim, P., and Fuhrer, M. S. *Nano Lett.* **13**, 3576–3580 (2013).

[89] Hofstadter, D. *Phys. Rev. B* **14**, 2239–2249 (1976).

[90] Dean, C. R., Wang, L., Maher, P., Forsythe, C., Ghahari, F., Gao, Y., Katoch, J., Ishigami, M., Moon, P., Koshino, M., Taniguchi, T., Watanabe, K., Shepard, K. L., Hone, J., and Kim, P. *Naure* **497**, 598–602 (2013).

[91] Choi, M. S., Lee, G.-H., Yu, Y.-J., Lee, D.-Y., Lee, S. H., Kim, P., Hone, J., and Yoo, W. J. *Nature Commun.* **4**, 1624 (2012).

[92] Gerbaldi, C., Nair, J., Ahmad, S., Meligrana, T. G., Bongiovanni, R., Bodoardo, S., and Penazzi, N. *J. Power Sources* **195**, 1706–1713 (2010).

[93] Efetov, D. K. and Kim, P. *Phys. Rev. Lett.* **105**, 256805 (2010).

[94] Ye, J., Craciun, M. F., Koshino, M., Russo, S., Inoue, S., Yuan, H., Shimotani, H., Morpurgo, A. F., and Iwasa, Y. *PNAS* **108**, 13002Ű13006 (2010).

[95] Chen, F., Qing, Q., Xia, J., Li, J., and Tao, N. *J. Am. Chem. Soc.* **131**, 9908Ű9909 (2009).

[96] Chae, D.-H., Krauss, B., von Klitzing, K., and Smet, J. H. *Nano Lett.,* **10**, 466–471 (2010).

[97] Hurd, C. *The Hall Effect in Metals and Alloys.* Plenum Press, (1972).

[98] Moshkovich, M., Gofer, Y., and Aurbach, D. *JES* **148**, E155–E167 (2001).

[99] Lafkioti, M., Krauss, B., Lohmann, T., Zschieschang, U., Klauk, H., v. Klitzing, K., and Smet, J. H. *Nano Lett.* **10**, 1149–1153 (2010).

[100] Martin, J., Akerman, N., Ulbricht, G., Lohmann, T., Smet, J. H., von Klitzing, K., and Yocoby, A. *Nature Physics* **4**, 144–148 (2007).

[101] Zhang, Y., Brar, V., Girit, C., Zettl, A., and Crommie, M. F. *Nature Physics* **5**, 722–726 (2009).

[102] Cho, S. and Fuhrer, M. *Phys. Rev. B* **77**, 081402(R) (2008).

[103] Kuroda, M. A., Tersoff, J., and Martyna, G. J. *Phys. Rev. Lett.* **106**, 116804 (2011).

[104] Chockla, A. M., Panthani, M. G., Holmberg, V. C., Hessel, C. M., Reid, D. K., Bogart, T. D., Harris, J. T., Mullins, C. B., and Korgel, B. A. *J. Phys. Chem. C* **116**, 11917–11923 (2012).

[105] da Silva, R. and Wirth, G. I. *J. Stat. Mech.* **2010**, P04025 (2010).

[106] Caplan, P. J., Poindexter, E. H., Deal, B. E., and Razouk, R. R. *J. Appl. Phys.* **50**, 5847–5854 (1979).

[107] Nishi, Y. *Jpn. J. Appl. Phys.* **5**, 333 (1966).

[108] Poindexter, E. H., Gerardi, G. J., Rueckel, M.-E., Caplan, P. J., Johnson, N. M., and Bieglsen, D. K. *J. Appl. Phys.* **58**, 2844–2849 (1984).

[109] Park, Y.-B. and Rhee, S.-W. *Appl. Phys. Lett.* **66**, 3477–3479 (1995).

[110] Scharf, S., Schmidt, M., and Braunig, D. *Semicond. Sci. Technol.* **10**, 586–591 (1995).

[111] Manchanda, L., Vasi, J., and Bhattacharyya, A. B. *Appl. Phys. Lett.* **37**, 744–747 (1980).

[112] Park, H., Qi, J., Xu, Y., Varga, K., Weiss, S. M., Rogers, B. R., Lüpke, G., and Tolk, N. *Appl. Phys. Lett.* **95**, 062102 (2009).

[113] Dean, M. J., Brown, W. D., Sundaram, K. B., and Raider, S. I. *Silicon Nitride and Silicon Dioxide Thin Insulating Films.* The Electrochemical Society, (1997).

[114] El-Kareh, B. *Fundamentals of Semiconductor Processing Technologies.* Norwell: Kluwer Academic Publishers, (1995).

[115] Xu, K., Zheng, C., Zhang, Q., Yan, R., Ye, P. D., Wang, K., Seabaugh, A. C., Xing, H. G., Suehle, J. S., Richter, C. A., Gundlach, D. J., and Nguyen, N. *Nano Lett.* **13**, 131–136 (2012).

[116] Lu, Y. and Sah, C.-T. *J. Appl. Phys.* **76**, 4724–4727 (1994).

[117] DeKeersmaecker, R. F. and DiMaria, D. J. *J. Appl. Phys.* **51**, 1085–.1101 (1980).

[118] Landauer, R. *J. Appl. Phys.* **23**, 779–784 (1952).

[119] Rossi, E., Adam, S., and Sarma, S. D. *Phys. Rev. B* **79**, 245423 (2009).

[120] Ping, J., Yudhistira, I., Ramakrishanan, N., Cho, S., Adam, S., and Fuhrer, M. S. *Phys. Rev. Lett.* **113**, 047206 (2014).

[121] Ziman, J. H. *Principles of the Theory of Solids.* Cambridge University Press, (1972).

[122] Xu, R., Husmann, A., Rosenbaum, T. F., Saboungi, M.-L., Enderby, J. E., and Littlewood, P. B. *Nature* **390**, 57–60 (1997).

[123] Thio, T. and Solin, S. A. *Appl. Phys. Lett.* **72**, 3497–3499 (1998).

[124] Solin, S. A., Thio, T., Hines, D. R., and Heremans, J. J. *Science* **289**, 1530–1532 (200).

[125] Parish, M. M. and Littlewood, P. B. *Phys. Rev. B* **72**, 094417 (2005).

[126] Parish, M. M. and Littlewood, P. B. *Nature* **426**, 162–165 (2003).

[127] Abrikosov, A. A. *Phys. Rev. B* **58**, 2788–2795 (1998).

[128] Bergman, D. J. and Strelniker, Y. M. *Phys. Rev. B* **60**, 13016–13027 (1999).

[129] Magier, R. and Bergman, D. J. *Phys. Rev. B* **74**, 094423 (2006).

[130] Hwang, E. H., Adam, S., and Sarma, S. D. *Phys. Rev. B* **76**, 195421 (2007).

[131] Friedman, A. L., Tedesco, J. L., Campbell, P. M., Culbertson, J. C., Aifer, E., Perkins, F. K., Myers-Ward, R. L., Hite, J. K., Jr, C. R. E., Jernigan, G. G., and Gaskill, D. K. *Nano Lett.* **10**, 3962–3965 (2010).

[132] Adam, S., Hwang, E., Rossi, E., and Sarma, S. D. *Solid State Commun.* **149**, 1072–1079 (2009).

[133] Bruggeman, D. *Ann. Phys. Lpz.* **24**, 636 (1935).

[134] Stroud, D. *Phys. Rev. B* **12**, 3368–3373 (1975).

[135] Stroud, D. and Bergman, D. J. *Phys. Rev. B* **30**, 447–449(R) (1984).

[136] Bergman, D. J. and Stroud, D. G. *Phys. Rev. B* **62**, 6603–6613 (2000).

[137] Guttal, V. and Stroud, D. *Phys. Rev. B* **71**, 201304(R) (2005).

[138] Guttal, V. and Stroud, D. *Phys. Rev. B* **73**, 085202 (2006).

[139] Fogler, M. M. *Phys. Rev. Lett.* **103**, 236801 (2009).

[140] Jung, N., Crowther, A. C., Kim, N., Kim, P., and Brus, L. *Nano Lett.* **4**, 7005–7013 (2010).

[141] Abrahams, E., Anderson, P. W., Licciardello, D. C., , and Ramakrishnan, T. V. *Phys. Rev. Lett.* **42**, 673–676 (1979).

[142] Altshuler, B. L., Aronov, A. G., , and Lee, P. A. *Phys. Rev. Lett.* **44**, 1288–1291 (1980).

[143] Kechedzhi, K., Falko, V. I., McCann, E., and Alshuler, B. L. *Phys. Rev. Lett.* **98**, 176806 (2007).

[144] Gorbachev, R. V., Tikhonenko, F. V., Mayorov, A. S., Horsell, D. W., and Savchenko, A. K. *Phys. Rev. Lett.* **98**, 176805 (2007).

[145] Lee, P. A. and Ramakrishnan, T. V. *Phys. Rev. B* **26**, 4009–4012 (1982).

[146] Altshuler, B. L., Aronov, A. G., and Khmelnitsky, D. E. *J. Phys. C* **15**, 7367–7386 (1982).

[147] Lee, P. A. and Stone, A. D. *Phys. Rev. Lett.* **55**, 1622–1625 (1985).

Acknowledgements

- I would like to thank Prof. K. von Klitzing for his support and the stimulating discussions. His enthusiasm and passion towards science are a source of inspiration for me.

- My gratitude goes to Dr. J. Smet for the possibility to work in the Solid State Nanophysics group. His group provides the perfect scientific and technical environment for a PhD student.

- I am very grateful to all the "Smetions" for the unbelievable atmosphere in the group. Thanks to them I improved as a person and as a scientist. I found good friends. I will never forget them.

- I would like to thank the technical support and the clean room team. Without their help it would be impossible to carry out the experiments included in this thesis.

- A special thanks goes to my parents for their support and love. Too often I do not show my gratitude to them.

- I would like to thank my friends Andrea, Dario, Debora, Diego, Erica, Fabrizio, Federico, Francesca, Giovanna, Luca and Mirko. I can find them every time that I have a problem. They helped me to come out of the darkest period of my life.

- I would also like to thank the people that I lost during this journey.

- Finally, I would like to thank philosophy and poetry, because they saved the life of a delicate and wounded soul.